

International Atomic Energy Agency

INDC(BLR)-003

Distr. L

INDC**INTERNATIONAL NUCLEAR DATA COMMITTEE****EVALUATION OF NEUTRON DATA FOR
CURIUM-245**

V.M. Maslov, E.Sh. Sukhovitskij, Yu.V. Porodzinskij,
A.B. Klepatskij, G.B. Morogovskij

Radiation Physics & Chemistry Problems Institute,
220109 Minsk-Sosny, Belarus

February 1996

IAEA NUCLEAR DATA SECTION, WAGRAMERSTRASSE 5, A-1400 VIENNA

Reproduced by the IAEA in Austria
February 1996

EVALUATION OF NEUTRON DATA FOR CURIUM-245

V.M. Maslov, E.Sh. Sukhovitskij, Yu.V. Porodzinskij,
A.B. Klepatskij, G.B. Morogovskij

Radiation Physics & Chemistry Problems Institute,
220109 Minsk-Sosny, Belarus

Abstract

The evaluation of neutron data for ^{245}Cm is made in the energy region from 10^{-5}eV up to 20 MeV. The evaluation procedures are described. The resulting evaluated data, which were compiled in ENDF-6 format, are presented in graphical figures and compared with earlier evaluations contained in the JENDL-3 and ENDF/B-VI data libraries.

This work is performed under the Project Agreement CIS-03-95 with the International Science and Technology Center (Moscow). The Financing Party for the Project is Japan. The evaluation was requested by Y. Kikuchi (JAERI).

Date of Manuscript: 6 December 1995

Contents

1.	Introduction	7
2.	Resolved resonance region	7
2.1	Previous evaluations of resolved resonance parameters	7
2.2	Measured data fitting	7
2.2.1	Fission cross section	7
2.2.2	Other data	8
2.3	Evaluated resonance parameters up to 100 eV	8
2.3.1	Thermal energy region	8
2.3.2	Energy region $0.8 \div 100$ eV	8
2.3.3	Resonance parameter analysis	8
3.	Unresolved resonance region	10
3.1	Review	10
3.2	The s-wave average resonance parameter evaluation	11
3.2.1	Estimate of resonance level missing influence on $\langle D_{obs} \rangle$ and $\langle S_0 \rangle$	11
3.2.2	Evaluation of $\langle D_{obs} \rangle$, $\langle S_0 \rangle$, $\langle \Gamma_\gamma \rangle$ and $\langle \Gamma_f \rangle$ based on the resonance parameters	11
3.3	The p- and d-wave average resonance parameter evaluation	12
3.3.1	Neutron width	12
3.3.2	Neutron resonance spacing	13
3.3.3	Fission width	13
3.3.4	Radiative capture width, role of (n, γ f) reaction	13
3.4	Cross section evaluation in the region 0.1-54.9553 keV	13
3.4.1	Fitting of fission cross section structure	13
3.4.2	Drawbacks of ENDF/B-VI format and associated inconsistencies in neutron cross sections	13
3.4.3	Comparison of current and JENDL-3 evaluated data	14
4.	Fast neutron cross sections	15
4.1	Optical potential	15
4.2	Fission cross section	16
4.2.1	Status of the experimental data	16
4.2.2	Statistical model calculation of fission cross section	17
4.2.3	Fission transmission coefficient, level density and transition state spectrum	17
4.2.4	Fission cross section above emissive fission threshold	19
4.3	Inelastic scattering cross section	20
4.3.1	Compound inelastic scattering	21
4.3.2	Direct inelastic scattering	22
4.4	Radiative capture cross section	22
4.5	Cross sections of (n,2n) and (n,3n) reactions	22

5.	Energy distributions of secondary neutrons	23
5.1	Model calculations of (n,nx) reaction spectra	23
5.2	Prompt fission neutron spectra	24
5.2.1	Model calculations of prompt fission neutron spectra	24
5.2.2	Prompt fission neutron spectra evaluation	25
6.	Number of neutrons per fission	26
7.	Angular distributions of secondary neutrons	27
8.	Conclusions	27
9.	References	29
10.	Figure captions	31

1 Introduction

The advanced nuclear fuel cycle studies request the nuclear data of transplutonium isotopes¹. The neutron data for curium isotopes are especially important in this respect. Recently we have evaluated² the data for ²⁴³Cm. In this work the evaluation of ²⁴⁵Cm neutron data is performed. The next isotope, which neutron data would be evaluated is ²⁴⁶Cm. The curium isotopes data to be evaluated were requested by the General Manager of Japan Nuclear data Center Dr. Y. Kikuchi. The quantities evaluated are resolved and unresolved resonance parameters, total, elastic and inelastic scattering, fission, capture, (n,2n) and (n,3n) reaction cross sections, angular and energy distributions of secondary neutrons, including partial (n,xn) and (n,xnf) reaction spectra, fission spectra and number of neutrons per fission. The incident neutron energy range covered is from 10⁻⁵ eV up to 20 MeV. The evaluated quantities are compared with JENDL-3 evaluation³.

2 Resolved resonance region

2.1 Previous evaluations of resolved resonance parameters

The resonance parameter evaluation⁴ of ENDF/B-VI is based on fission cross section data measured from 0.01 eV up to 35 eV by Browne et al.⁵ and from 20 eV to 60 eV by Moore et al.⁶ Up to 39.5 eV Breit-Wigner single-level parameters of Browne et al.⁵ were adopted, while the R-matrix multilevel parameters of Moore et al.⁶ were adopted up to 60 eV. Both parameter sets were assumed to be of Breit-Wigner, single-level type. Negative resonance was placed at $E_r = -0.1$ eV. In JENDL-3 evaluation the resonance parameters of Browne et al.⁵ up to 20 eV were adopted, at higher neutron energies resonance parameters of Moore et al.⁶ were adopted up to 60 eV. Fission data by Moore et al.⁶ were fitted with the aid of smooth file. The negative resonance was assumed at $E_r = -0.1$ eV. The purpose of current resonance parameter evaluation is to extend the resolved resonance region up to 100 eV and fit the available fission data.

2.2 Measured data fitting

2.2.1 Fission cross section

The bomb-shot fission cross section data of Moore et al.⁶ are available in the energy region of 20 - 100 eV. Assuming realistic measurement conditions we

used fission data^{5,6} to derive resonance parameters Γ_n° , Γ_f , Γ_γ and E_r up to 100 eV.

2.2.2 Other data

The transmission was measured by Belanova et al.⁷ in the energy region of 8÷36 eV. However the resonance parameters of Belanova et al.⁷ are rather discrepant with those of Browne et al.⁵ and Moore et al.⁶ The other data⁸⁻¹³ on thermal cross sections and resonance integrals will be used for comparison purposes.

2.3 Evaluated resonance parameters up to 100 eV

We have fitted the data by Browne et al.⁵ and the data by Moore et al.⁶ to get a whole resonance parameter set up to 100 eV to avoid the smooth file inclusion into evaluated data file.

2.3.1 Thermal energy region

We fitted the data by Browne et al.⁵ at low energies adding three negative resonances at $E_r = -5.0$ eV, $E_r = -2.0$ eV, $E_r = -0.1$ eV. The resulted thermal cross section $\sigma_f^{2200} = 2142.38$ barn, which is compatible with estimate of $\sigma_f^{2200} = 2143 \pm 58$ barn by Browne et al.⁵

2.3.2 Energy region 0.8 ÷ 100 eV

The resonance parameters of Browne et al.⁵ and Moore et al.⁶, i.e. $2g\Gamma_n$, Γ_f and E_r are used as starting values. To fit the data by Browne et al.⁵ we have added two resonances: $E_r = 2.15$ eV and $E_r = 15.2$ eV (see figs. 2.1, 2.2). To fit the data by Browne et al.⁵ we have got the parameters of 44 resonances (see figs. 2.3, 2.4), instead of 26, as in original paper.⁶ In the energy region of 60-100 eV we have got 30 resonance parameters, fitting the data by Moore et al.⁶ However, the number of resonances here seems rather small. That is due to poor resolution above 60 eV. The other indication of this is the large values of Γ_n° and Γ_f . The radiative width Γ_γ is allowed to fluctuate between 20 and 60 meV during resonance parameter search.

2.3.3 Resonance parameter analysis

We have got 91 resonance parameters up to 100 eV, including three negative resonance parameters at $E_r = -5.0$ eV, $E_r = -2.0$ eV, $E_r = -0.1$ eV. The assigning of resonance spins was done as follows. Two assumptions were adopted: the number of resonances with spin J is proportional to $(2J + 1)$, reduced neutron width distribution should obey that of Porter-Thomas, neutron resonance spacing distribution should obey that of Wigner. Figures

2.7, 2.9 show that neutron resonance spacings obey to Wigner distribution. In case of reduced neutron widths the number of small Γ_n^o value is too low, which is due to missing of resonances.

The fission cross section was calculated as follows:

$$\sigma_f(E) = \frac{C}{\sqrt{E}} \sum_i \frac{g\Gamma_{n,i}^o \Gamma_{f,i}}{\Gamma_i^2} \Psi(x, \theta),$$

where $\Psi(x, \theta)$ is the Doppler function, $x = \frac{2(E-E_{0i})}{\Gamma_i}$, $\theta = \frac{\Gamma_i}{\Delta}$ and $\Delta^2 = ((\Delta_T)^2 + (\Delta_E)^2)$ takes into account the temperature dependence and experimental energy resolution of cross section measurements, respectively, while $\Delta^2 = \frac{4mkTE}{A+1} + (0.0278*\Delta t)^2 * E^3$. We modelled the dependence of Δ_E because the experimental resolution function of Browne et al.⁵ and Moore et al.⁶ experiments is unknown. Values of Δt were obtained from the experimental data^{5,6} on $\sigma_f(E)$ and were checked together with effective temperature $T = 300^0$ K by performing shape analysis of some isolated resonances in the energy region $1 \div 60$ eV. The values of energy resolutions that were used for the calculations are in the table 2.1.

Table 2.1

Cross section	ΔE , eV	Resolution Δt , $\mu\text{sec}/\text{m}$
σ_t	0.01-0.09	19.00
	0.10-1.28	2.30
	1.29-5.95	0.28
	6.00-19.60	0.29
	19.90-21.49	0.0120
σ_f	21.53- 23.32	0.0110
	23.35-25.49	0.0100
	25.52-28.50	0.0090
	28.53-32.57	0.0080
	32.61-37.73	0.0070
	37.77-44.21	0.0060
	44.26-69.30	0.0050
	69.35-81.24	0.0045
	81.30-100.0	0.0050

The resonance radiation width values Γ_γ were obtained using condition $20 \text{ meV} \leq \Gamma_\gamma \leq 60 \text{ meV}$. The resulted radiation width distribution obeys Porter-Thomas distribution with number of the degrees of freedom $\nu = 20$ (see fig. 2.10).

The average resonance parameters, thermal cross sections and resonance integrals of current, ENDF/B-VI and JENDL-3 evaluations are compared in Table 2.2. It is reasonable to compare single-level average resonance parameters for the interval $0.8 \div 20$ eV. In case of JENDL-3 evaluation $\langle \Gamma_n^0 \rangle = 0.2514$ eV, $\langle \Gamma_f \rangle = 318.83$ eV, in present case $\langle \Gamma_n^0 \rangle = 0.2009$ eV, $\langle \Gamma_f \rangle = 394.59$ eV. The net effect of using the JENDL-3 resonance parameters would be more strong and narrow resonances (see fig.2.2). Thermal cross sections and resonance integrals of current, ENDF/B-VI and JENDL-3 evaluations are fairly consistent.

Table 2.2

	ENDF/B-VI	JENDL-3	This evaluation
$\langle \Gamma_n^0 \rangle$, meV	0.3884	0.3719	0.2812 ----- 0.2383 ¹⁾
$\langle \Gamma_\gamma \rangle$, meV	40.2564	40.0	37.7913 ----- 37.4098 ¹⁾
$\langle \Gamma_f \rangle$, meV	513.821	503.513	537.301 ----- 477.977 ¹⁾
σ_t , barn	2569.11	2358.55	2512.50
σ_γ , barn	341.938	346.351	359.145
σ_f , barn	2218.28	2000.61	2142.38
σ_n , barn	8.89445	11.5898	10.9728
g_γ	0.95151	0.93979	0.94175
g_f	0.95722	0.94771	0.95070
I_γ , barn	108.428	109.450	105.404
I_f , barn	828.733	789.232	793.927

¹⁾ up to 60 eV.

The thermal total σ_t , capture σ_γ , and scattering σ_n cross sections, g_γ -, and g_f -factors, as well as resonance integrals I_γ and I_f values are calculated with a code INTER¹⁴.

3 Unresolved resonance region

3.1 Review

Unresolved resonance region of ²⁴⁵Cm is supposed to be from 0.1 keV up to 54.9553 keV. The lower energy is the end-point of resolved resonance region,

the upper energy is the threshold energy of the inelastic scattering. We supposed s -, p - and d -wave neutron-nucleus interactions to be effective. We suppose also the $(n, \gamma f)$ reaction to be important here due to high fissility of ^{245}Cm compound nucleus.

3.2 The s -wave average resonance parameter evaluation

3.2.1 Estimate of resonance level missing influence on $\langle D_{obs} \rangle$ and $\langle S_0 \rangle$

The preliminary estimates of average partial widths were obtained by averaging the evaluated resolved resonance ($E_r > 0$) parameters. They are as follows:

$$\begin{aligned}\langle \Gamma_n^o \rangle &= 2.726 \times 10^{-4} \text{ (eV)}^{1/2} \\ \langle \Gamma_f \rangle &= 0.541 \text{ eV} \\ \langle D_{obs} \rangle &= 1.138 \text{ eV} \\ \langle \Gamma_\gamma \rangle &= 0.0378 \text{ eV}\end{aligned}$$

Note that due to missing of weak resonances these values overestimate actual reduced neutron width $\langle g\Gamma_n^o \rangle$ and neutron resonance spacing $\langle D_{obs} \rangle$. To get a physically justified values for $\langle g\Gamma_n^o \rangle$ and $\langle D_{obs} \rangle$ we employ a method, which is described elsewhere¹⁵. Both reduced neutron width and neutron resonance spacing distributions are obtained in a unified approach. We take into account the correlation of weak resonance missing and resonance missing due to poor experimental resolution. The resolution function parameters as well as $\langle g\Gamma_n^o \rangle$ and $\langle D_{obs} \rangle$ are obtained by maximum likelihood method when comparing experimental distributions of reduced neutron width and resonance spacing with Porter-Thomas and Wigner distributions, modified for the resonance missing. The latter distributions will be called expected distributions. We assume that several energy intervals with different experimental resolution may occur. Then the expected distribution is a weighted sum of partial contributions.

3.2.2 Evaluation of $\langle D_{obs} \rangle$, $\langle S_0 \rangle$, $\langle \Gamma_\gamma \rangle$ and $\langle \Gamma_f \rangle$ based on the resonance parameters

To evaluate average neutron resonance spacing $\langle D_{obs} \rangle$ and neutron strength function S_0 we apply our method¹⁵ to the resolved resonance data base. We suppose that data up to 100 eV should be taken into account. Figure 3.1 shows the cumulative sum of resolved resonance levels and demonstrates energy intervals which were distinguished. Level distances greater than eight

average distances were omitted from the analysis, due to the negligible probability of this event in pure Wigner distribution approach. This approximation also remains valid if we assume one resonance missing between each two neighboring resonances with distances greater than $8 < D >$. Evaluated values are obtained using four energy intervals, they are:

$$\begin{aligned} < S_0 > = 1.256 \times 10^{-4} \text{ (eV)}^{-1/2} \\ < D_{obs} > = 0.698 \text{ eV} \end{aligned}$$

Average fission and radiation widths are less sensitive to resonance missing, so we adopted values obtained by averaging of resolved resonance parameters up to 100 eV.

Figure 3.2 shows the comparison of expected and experimental reduced neutron width distributions. Figure 3.3 shows the comparison of distributions for neutron resonance spacing. Both figures are obtained for energy interval 0-100 eV as a weighted sum of distributions in four chosen energy intervals. The expected distributions show the effect of resonance missing. The figures 3.2-3.3 show that the expected distributions are consistent with the experimental data for energy interval 0-100 eV. That is why the $< D_{obs} >$ and S_0 estimates could be considered reliable. Double humped behavior of expected neutron reduced width distribution on Fig 3.2 is due to different thresholds for reduced neutron width discrimination in measurements of Browne et al.⁵ (0-20 eV) and Moore et al.⁶ (20-100 eV).

3.3 The p- and d-wave average resonance parameter evaluation

3.3.1 Neutron width

Average neutron width is calculated as follows

$$< \Gamma_n^{lJ} > = S_l < D_J > E^{1/2} P_l,$$

where P_l is the transmission factor for the l th partial wave, which was calculated within black nucleus model. The p -wave neutron strength function $S_1 = 2.10 \times 10^{-4} \text{ (eV)}^{-1/2}$ was calculated with the optical model, using the deformed optical potential, described below. According to the results of optical calculations S_0 was assumed to decrease linearly to the value of $S_0 = 1.172 \times 10^{-4} \text{ (eV)}^{-1/2}$ for neutron energy of 54.9553 keV. The d -wave neutron strength function was assumed to be equal to $S_0 = 1.256 \times 10^{-4} \text{ (eV)}^{-1/2}$. Since the d -wave contribution is rather small, the impact of this approximation on calculated values is negligible.

3.3.2 Neutron resonance spacing

Neutron resonance spacing $\langle D_J \rangle$ was calculated with the phenomenological model¹⁶, which takes into account the shell, pairing and collective effects. The main parameter of the model \tilde{a} was normalized to the observed neutron resonance spacing $\langle D_{obs} \rangle = 0.698$ eV.

3.3.3 Fission width

Fission widths are calculated within a double-humped fission barrier model. Energy and angular momentum dependence of fission width is defined by the transition state spectra at inner and outer barrier humps. We constructed transition spectra by supposing the triaxiality of inner saddle and mass asymmetry at outer saddle. They will be described below. The calculated fission widths $\langle \Gamma_f^{3+} \rangle$ and $\langle \Gamma_f^{4+} \rangle$ are normalized to the adopted average fission width $\langle \Gamma_f \rangle = 0.345$ eV, which allows to describe fission measured data in unresolved resonance region. This value is somewhat lower than average resolved resonance fission width.

3.3.4 Radiative capture width, role of $(n, \gamma f)$ reaction

Energy and angular momentum dependence of radiative capture width are calculated within a two-cascade γ -emission model with allowance for the $(n, \gamma f)$ reaction competition to the $(n, \gamma \gamma)$ reaction. The $(n, \gamma \gamma)$ reaction is supposed to be a radiative capture reaction. The radiative capture width was normalized to the value of $\langle \Gamma_\gamma \rangle = 37.8$ meV. (For details see Chapter IV).

3.4 Cross section evaluation in the region 0.1-54.9553 keV

3.4.1 Fitting of fission cross section structure

There are fission data of Moore et al.⁶ covering the unresolved resonance region and data of Gerasimov et al.¹⁷ in standard energy intervals up to 21.5 keV and data of White et al.¹⁸ above 11 keV. The averaged data of Moore et al.⁶ nor any other data do not imply any structure (see fig.3.5), so we decided to describe these data with average parameters. The calculated fission cross section is compared with measured data on fig.3.5.

3.4.2 Drawbacks of ENDF/B-VI format and associated inconsistencies in neutron cross sections

Within ENDF/B-VI format we can not distinguish between (l, J, j) reaction channels with different channel spin values $j = l \pm 1/2$. Specifically, channels $(l = 1, J = 3, j = 1/2)$ and $(l = 1, J = 3, j = 3/2)$ are treated as a lumped

channel ($l = 1, J = 3$) with neutron degrees of freedom $\nu=2$, then the average neutron width $\langle \Gamma_n^{lj} \rangle$ for ($l = 1, J = 3$) channel equals

$$\langle \Gamma_n^{13} \rangle = 2S_1 P_1 \sqrt{E} D_3$$

This results in an increase of elastic scattering cross section as compared with the case when one treats channels ($l = 1, J = 3, j = 1/2$) and ($l = 1, J = 3, j = 3/2$) separately. Within ENDF/B-VI format constraints the elastic enhancement would be too strong because of artificial duplication of elastic scattering neutron width. Moreover, the increase of neutron number of degrees of freedom decreases the competition of fission reaction channel. Henceforth the fission and capture reactions, calculated with standard ENDF/B utility codes are decreased as compared with the results of physically correct approach. The magnitude of this discrepancy at ~ 54 keV incident neutron energy amounts to $\sim 3\%$ in calculated fission cross section.

3.4.3 Comparison of current and JENDL-3 evaluated data

Evaluated fission cross sections of this work is 20% higher than JENDL-3 at lower edge of unresolved resonance region. That is due to data of Gerasimov et al.¹⁷, which are higher than data of Moore et al.⁶ and White et al.¹⁸. At upper edge both evaluations fit the data of Moore et al.⁶ and White et al.¹⁸ and the difference decreases to 3% at 40 keV. Figure 3.4 gives the comparison of σ_f for both evaluations. The discrepancies are noticed when comparing the (n, γ) reaction cross sections (see fig. 3.5) Current evaluated cross section is more than 1.5 times as large as JENDL-3 evaluated capture cross section. This discrepancy is due to much lower values of $\langle D \rangle$, $\langle \Gamma_f \rangle$ and partly to (l, J) - channel dependence of fission width in our approach. This dependence is due to adopted transition states spectra structures (see below). Specifically the ratio of $\langle \Gamma_f^{4+} \rangle / \langle \Gamma_f^{3+} \rangle \simeq 1.3$ is almost independent on incident neutron energy, that will lead to the increased capture reaction cross section for the ($l = 0, J = 4$) channel as compared with JENDL-3 approach. In approach, adopted in JENDL-3 the fission width value is independent on spin and parity. Furthermore, the adopted in JENDL-3 average fission width value of ~ 1.8 eV is anomalously high. With this value of fission width measured fission data can not be reproduced in our approach. Comparison of evaluated data for fission and capture cross-sections is given in table 3.1.

Table 3.1

Average cross sections in unresolved resonance region for ^{245}Cm

E , keV	$\sigma_{f,\gamma}$, b	σ_f , b(JENDL-3)	σ_γ , b	σ_γ , b(JENDL-3)
0.10	40.1	34.24	10.43	6.46
0.20	28.18	24.21	7.26	4.34
0.30	22.91	19.77	5.86	3.43
0.50	17.64	15.34	4.47	2.53
0.70	14.87	12.99	3.72	2.07
1.0	12.38	10.91	3.09	1.65
2.0	8.72	7.81	2.13	1.11
3.0	7.14	6.45	1.73	0.898
5.0	5.60	5.12	1.34	0.713
7.0	4.95	4.38	1.06	0.627
10.0	4.25	3.85	0.918	0.568
20.0	3.30	3.12	0.726	0.464
30.0	2.94	2.79	0.651	0.451
40.0	2.73	2.62	0.608	0.429

4 Fast neutron cross sections

The measured neutron data in fast energy region, i.e. above 54 keV are available only for fission cross section. The detailed fission cross section data are available only in the energy range up to ~ 9 MeV. At higher energies there are two discrepant measurements^{18,19} at 14.1 MeV. The bomb-shot data of Moore et al.⁶ are also rather discrepant with more recent data^{18,20,21}. So, the available fission data fit would be used as constraint for (n, n') , (n, γ) , $(n, 2n)$ and $(n, 3n)$ reaction cross sections evaluation. We reproduce also the average resonance fission width within double-humped fission barrier model. To fix fission channel parameters the systematic trends are used.

4.1 Optical potential

The deformed optical potential for $n+^{245}\text{Cm}$ interaction is employed. The starting values for the potential parameters were those for $n+^{238}\text{U}$ interaction²². The isotopic dependences of real and imaginary parts of the potential were calculated using the optical potential parameter systematics²³. Six levels of the ground state band ($7/2^+$, $9/2^+$, $11/2^+$, $13/2^+$, $15/2^+$, $17/2^+$) are coupled. Since the fifth and sixth levels are missing in compilation²⁴, they were added as $E_J = A(J(J+1) - K(K+1))$. The deformation parameters β_2 and β_4

are obtained by fitting S_0 value of $1.256 \times 10^{-4} \text{ (eV)}^{-1/2}$. We modified the original potential geometry parameters²² to fit total cross section and differential scattering data for N-odd targets above 10 MeV. This procedure of parameter fitting is well tested in case of ^{239}Pu , ^{235}U and ^{233}U targets. The potential parameters are as follows:

$$W_D = \begin{cases} V_R = 46.38 - 0.3E, \text{ MeV}, r_R = 1.26 \text{ fm}, a_R = 0.615 \text{ fm} \\ 3.71 + 0.4E, \text{ MeV}, E < 10 \text{ MeV}, r_D = 1.24 \text{ fm}, a_D = 0.5 \text{ fm} \\ 7.71 \text{ MeV}, E > 10 \text{ MeV} \end{cases}$$

$$V_{SO} = 6.4 \text{ MeV}, r_{SO} = 1.12 \text{ fm}, a_{SO} = 0.47 \text{ fm}, \beta_2 = 0.233, \beta_4 = 0.076$$

The s- and p-wave strength functions and potential scattering cross sections, calculated with this potential parameters in a coupled channel approach at incident neutron energy of 100 eV are:

$$S_0 = 1.256 \times 10^{-4} \text{ (eV)}^{-1/2} \quad S_1 = 2.10 \times 10^{-4} \text{ (eV)}^{-1/2} \quad R' = 9.52044 \text{ fm}$$

The reaction cross sections, calculated with deformed optical potential and spherical optical potential, which is used in JENDL-3 evaluation, are compared on fig.4.1. The significant differences below 1 MeV and above 10 MeV would be manifested in inelastic scattering cross section and $(n, 3n)$ cross section. The total cross sections appear to be rather close (see fig.4.2), while elastic scattering cross section are rather different above 1 MeV (see fig. 4.3).

4.2 Fission cross section

4.2.1 Status of the experimental data

The bomb-shot data of Moore et al.⁶ cover the incident neutron energy region from 20 eV up to 2.2 MeV. However, above 100 keV they are rather discrepant with data, obtained with accelerator-driven neutron sources. The data of White et al.¹⁸ were measured with linac, but they are unavailable in numerical form. They appear to be systematically lower than Moore et al.⁶ data above 0.1 MeV. For the incident neutron energies up to ~ 9 MeV these data were taken from the graph. Fomushkin et al.²⁰ data, published in 1990 appear to be rather different from both data sets at incident neutron energies below 1.5 MeV. The latter data predict different cross section shape below 1.5 MeV. Above 1.5 MeV incident neutron energy the data of White et al.¹⁸ and Fomushkin et al.²⁰ are compatible. Both data sets are incompatible with data by Moore et al.⁶ in the first plateau region. although the data of Moore et al.⁶ are well described with average resonance parameters up to 54 keV (see fig. 3.4). The preliminary data of Fursov et al.²¹ appear unrealistically high in the energy region from 0.1 MeV up to 0.4 MeV. The bump, evident in data by Fursov et al.²¹ near the upper edge of the first plateau region also can not be interpreted.

4.2.2 Statistical model calculation of fission cross section

We consider the data base to be fairly consistent in the first plateau region, i.e. above ~ 1.5 MeV. At lower energies we will follow the trend of data by Fomushkin et al.²⁰. The fission cross section is calculated within the statistical model. The fission widths for s -wave neutrons Γ_f^{3+} and Γ_f^{4+} are fitted at 0.1 keV by varying the positions of transition spectra band-heads to reproduce the average fission width $\langle \Gamma_f \rangle = 0.345$ eV. To calculate fission cross section below 0.3 MeV we fit the fission cross section value at 54 keV, evaluated with the average resonance parameters. The fission cross section above 0.3 MeV incident neutron energy is consistent with data of Fomushkin et al.²⁰ The slope of the calculated fission cross section with energy in the first plateau region is consistent with the measured data base.

The comparison of calculated fission cross section with JENDL-3 evaluation and measured data is shown in figs. 4.4 and 4.5. The statistical theory calculation of fission cross section was accomplished within the double-humped barrier model. The approach employed in code STAT is described in more details elsewhere.²⁵ The procedure of calculating fission transmission coefficients is briefly described below.

4.2.3 Fission transmission coefficient, level density and transition state spectrum

The collective levels of ^{246}Cm fissioning nuclide, lying within pairing gap define the $^{245}\text{Cm}(n,f)$ fission cross section below incident neutron energy of ~ 0.5 MeV. These levels comprise the discrete transition spectra at both saddles. The discrete transition spectra contribution to the fission transmission coefficient is dependent upon the order of symmetry for ^{246}Cm fissioning nucleus at inner and outer saddles. Due to the axial asymmetry at the inner saddle²⁶ the respective 2^+ -band-heads are lowered as compared with the respective positions of 2^+ -band-heads at ground state deformation. The positions of negative parity bands $K^\pi = 0^-, 1^-, 2^-$ at outer saddle are lowered due to mass asymmetry²⁶. With transition state spectra thus defined (see Table 4.1) the fission barrier parameters are obtained (see table 4.2). The calculated fission widths at incident neutron energy of 0.1 keV are $\Gamma_f^{3+} = 0.291$ eV and $\Gamma_f^{4+} = 0.391$ eV reproduce the average fission width $\langle \Gamma_f \rangle = 0.345$ eV.

At excitation energies above the pairing gap, which is assumed to be 1.0 MeV, level density of axially symmetric fissioning nucleus is calculated in constant temperature approximation, i.e. $\rho(U) = T_f^{-1} \exp((U - U_o)/T_f)$. The respective parameters, nuclear temperature T_f and excitation energy shift U_o are defined at the matching energy $U_c = 3.6$ MeV. At excitation energies above U_c the continuum part of the transition state spectrum is repre-

sented with the phenomenological model¹⁶, which takes into account pairing, shell and collective effects at saddle deformations. After that the effects of non-axiality and mass asymmetry are included. The detailed procedure of calculating fission transmission coefficient is described elsewhere²⁵. The respective parameters: shell correction at saddles δW , correlation function Δ , quadrupole deformation ε , and momentum of inertia at zero temperature F_0/\hbar^2 are given in Table 4.3.

The generalized pairing model provides the means of taking into account the discrete character of few quasi-particle excitations just above the pairing gap. It was shown to be important in case of even-even fissioning nucleus ^{236}U in the $^{235}\text{U}(n,f)$ reaction²⁵. We modelled the nuclear level density $\rho(U)$ above the pairing gap up to the four-quasi-particle excitation threshold as $\rho(U) = \rho(\hat{U})/(1 + \exp(U_2 - U + \delta_1)/\delta_2)$. The two-quasi-particle states level density of even-even fissioning nucleus ^{246}Cm defines the fission cross section shape at incident neutron energies $\sim 0.5\div 2\text{MeV}$ (see fig. 4.4), the parameters $\hat{U} = 1.7\text{ MeV}$, $\delta_1 = \delta_2 = 0.2\text{ MeV}$ values were extracted. Above $\sim 2\text{ MeV}$ incident neutron energy fission cross section data were fitted (see fig. 4.5) by slight increase of pairing correlation function. The parameters used for calculation of neutron emission competition are described below.

Table 4.1

Transition spectra band-heads of ^{246}Cm

inner saddle		outer saddle	
K^π	$E_{K^\pi}, \text{ MeV}$	K^π	$E_{K^\pi}, \text{ MeV}$
0^+	0.0	0^+	0.0
2^+	0.1	2^+	0.3
0^-	0.4	0^-	0.0
1^-	0.4	1^-	0.1
2^+	0.5	2^+	0.5
2^-	0.4	2^-	0.1
0^+	0.8	0^+	0.8
0^+	0.8	0^+	0.8

Table 4.2

Fission barrier parameters

Nucleus	Barrier	Barrier height, MeV	Curvature, MeV
²⁴⁶ Cm	inner	6.00	0.9
²⁴⁶ Cm	outer	4.80	0.6
²⁴⁵ Cm	inner	6.45	0.8
²⁴⁵ Cm	outer	5.55	0.6
²⁴⁴ Cm	inner	6.43	0.9
²⁴⁴ Cm	outer	5.1	0.6
²⁴³ Cm	inner	6.3	0.8
²⁴³ Cm	outer	5.6	0.6

Table 4.3

Level density parameters of ²⁴⁶Cm fissioning nucleus and residual nucleus
²⁴⁵Cm

Parameter	inner saddle	outer saddle	neutron channel
δW , MeV	2.5	0.6	-2.676
Δ , MeV	$\Delta_0 + 0.07$	$\Delta_0 + 0.07$	Δ_0
ε	0.6	0.8	0.24
F_0/\hbar^2 , MeV ⁻¹	100	200	73

Below incident neutron energy of 0.5 MeV the neutron cross sections are calculated within Hauser-Feshbach approach with a width fluctuation correction taken into account. For width fluctuation correction calculation only Porter-Thomas fluctuations are taken into account. Effective number of degrees of freedom for fission channel is defined at the higher (inner) saddle as $\nu_f^{J\pi} = T_f^{J\pi}/T_{f_{\max}}^{J\pi}$, where $T_{f_{\max}}^{J\pi}$ is the maximum value of the fission transmission coefficient $T_f^{J\pi}$. Above incident neutron energy of 0.5 MeV the Tepel et al.²⁷ approach is employed.

4.2.4 Fission cross section above emissive fission threshold

The first chance fission cross section of ²⁴⁶Cm nucleus above the emissive fission threshold is fixed with the level density and fission barrier parameters systematics²⁵ (see Tables 4.2, 4.3) and secondary neutron spectra parameterization (see fig. 4.6). A consistent description of a complete set of measured data on (n,f), (n,2n) and (n,3n) for ²³⁸U and ²³⁵U targets was accomplished with the secondary neutron spectra parameterization²⁸, which

is used here. The fission barrier parameters of ^{245}Cm are fixed in $^{244}\text{Cm}(n,f)$ reaction data analysis. The fig.4.7 shows the $^{244}\text{Cm}(n,f)$ data description. One may note that the over-threshold structure apparent in $^{244}\text{Cm}(n,f)$ fission cross section around 1 MeV incident neutron energy is reproduced. The level density of ^{245}Cm fissioning nucleus was calculated within the framework of generalized pairing model¹⁶. The intrinsic state density is represented by the sum of n-quasiparticle state densities.²⁵ The other fissioning nuclei ^{244}Cm and ^{243}Cm fission barrier parameters are obtained from $^{243}\text{Cm}(n,f)$ and $^{242}\text{Cm}(n,f)$ data analyses² and parameter systematics trends (see table 4.2).

The calculated fission cross section is drastically different from JENDL-3 evaluated curve above (n,nf) reaction threshold (see fig. 4.6). This discrepancy is unavoidable, since the measured data of White et al.¹⁸ and Fomushkin et al.¹⁹ appear to be just as high as reaction cross section at 14.1 MeV, so they are incompatible with the calculated fission cross section. The comparison with JENDL-3 evaluated fission cross section is shown on figure 4.8.

4.3 Inelastic scattering cross section

The inelastic scattering cross section is calculated with the statistical codes STAT and STAPRE²⁹. The discrete level excitation (compound and direct), continuum excitation and pre-equilibrium emission contribute to the inelastic scattering cross section. The low-lying level scheme of Nuclear Data Sheets²⁴ appear incomplete at excitation energy as low as 0.5 MeV. The two levels, which were added are the ground state $K^\pi = 7/2^+$ band levels $J = 15/2, 17/2$, ($J = 9/2, 11/2$ and $13/2$ levels are present). The number of discrete excited levels in ^{245}Cm is 17 up to 0.51 MeV (see Table 4.4), above this excitation energy appreciable missing of levels occurs (see fig.4.9). In JENDL-3 evaluation there are 23 discrete excited levels up to 0.769 MeV, i.e. the missing of levels above ~ 0.5 MeV is ignored. The continuum level density below excitation energy $U_c = 2.4$ MeV is calculated with the constant temperature model

$$\rho(U) = T^{-1} \exp((U - U_0)/T),$$

here the constant temperature model parameters, energy shift $U_0 = -0.65311$ MeV, nuclear temperature $T = 0.36246$ MeV. At higher excitation energies the phenomenological model¹⁶ is used. The main model parameter \tilde{a} for ^{245}Cm residual nucleus is obtained by fitting the evaluated neutron resonance spacing of ^{244}Cm target nuclide $< D_{obs} > = 7.916$ eV. To evaluate $< D_{obs} >$ we have used evaluated neutron resonance parameters³².

Within our approach¹⁵ we have distinguished three energy regions with similar resolution functions. Two energy intervals were omitted from the analysis because the distances between appropriate resonances are greater than $6 < D >$ (see fig.4.10).

4.3.1 Compound inelastic scattering

The residual nucleus ^{245}Cm level density modelling, adopted in present work changes the inelastic scattering cross section below 5 MeV as compared with JENDL-3 evaluation (see fig. 4.11). Above 1 MeV incident neutron energy the discrepancy is due to direct excitation of the ground state band levels. Above 1 MeV incident neutron energy inelastic scattering to the continuum gives a major contribution to the total inelastic scattering cross section. Above 5 MeV incident neutron energy pre-equilibrium emission and direct

Table 4.4

Level scheme of ^{245}Cm

$E_{J\pi}$, MeV	J	π	K	band	
0.000	7/2	+	7/2	A	
0.0547	9/2	+	7/2	A	
0.1214	11/2	+	7/2	A	
0.1971	13/2	+	7/2	A	
0.2528	5/2	+	5/2	B	
0.2923	15/2	+	7/2	A	*
0.2958	7/2	+	5/2	B	
0.3505	9/2	+	5/2	B	
0.3559	1/2	+	1/2	C	
0.3615	3/2	+	1/2	C	
0.3879	9/2	-	9/2	D	
0.3957	17/2	+	7/2	A	*
0.4170	11/2	+	5/2	B	
0.4188	5/2	+	1/2	C	
0.4310	7/2	+	1/2	E	
0.4428	11/2	-	9/2	D	
0.4980	13/2	+	5/2	B	
0.5057	13/2	-	9/2	D	

*) added

inelastic scattering are the two reaction mechanisms which define inelastic scattering cross section (see fig. 4.11). The pre-equilibrium model parameters were tested by the statistical model description of $^{238}\text{U}+n$ interaction

secondary neutron spectra and consistent description of fission and (n,xn) reaction data for major actinides²⁸. Steep decrease of $(n,n\gamma)$ reaction cross section of JENDL-3 above 5 MeV (see fig. 4.15) is due to missing of pre-equilibrium emission of neutrons.

4.3.2 Direct inelastic scattering

The direct inelastic scattering changes the shape of ground band levels excitation cross sections above 1 MeV incident neutron energy (see figs. 4.12 - 4.16). This mechanism defines partly the hard-energy tail in total inelastic scattering cross section (see fig. 4.11). The calculations were accomplished with the code COUPLE²³.

4.4 Radiative capture cross section

The radiative capture cross section is calculated within a statistical approach up to 5 MeV. Radiative capture strength function $S_{\gamma 0} = 541.55$. At higher incident neutron energies we assume radiative capture cross section to be 0.1 mbarn. The radiative capture width was calculated with $(n,\gamma f)$ and $(n,\gamma n')$ reactions competition against "true" capture reaction $(n,\gamma\gamma)$. The role of $(n,\gamma f)$ and $(n,\gamma n')$ reactions is illustrated on fig.4.14 by sharp decrease of capture cross section above 0.5 MeV incident neutron energy, as compared with JENDL-3 evaluation.

4.5 Cross sections of $(n,2n)$ and $(n,3n)$ reactions

The current and JENDL-3 evaluated $(n,2n)$ and $(n,3n)$ cross sections are drastically different. The magnitude of $(n,2n)$ cross section below the $(n,2nf)$ reaction threshold is defined by (n,nf) and $(n,2n)$ reaction competition. The reaction cross sections of this work and JENDL-3 below the $(n,2nf)$ reaction threshold virtually coincide (see fig. 4.1). To calculate the $(n,2n)$ reaction cross section in a threshold region we use an approach, developed for description of the $^{239}\text{Pu}(n,2n)$ reaction cross section³³. The level density of residual nuclide ^{244}Cm was modelled as follows. The levels within a pairing gap were represented with a constant temperature approach, since the experimental level schema is rather incomplete. Above the pairing gap the two-quasi-particle states level density is used. The detailed procedure is described elsewhere³³. The present and JENDL-3 evaluations are compared in fig.4.18. The shape of $(n,2n)$ reaction cross sections of JENDL-3 evaluation appears unrealistic. In case of $(n,3n)$ reaction the difference in reaction cross section above 11 MeV (see fig. 4.1) contributes essentially to the discrepancy, shown on fig. 4.19.

5 Energy distributions of secondary neutrons

There is no measured data on secondary neutron spectra except average fission neutron spectrum energies. To calculate neutron energy distributions of $(n, xn\gamma)$ and (n, xnf) , $x=1, 2, 3$ reactions we use a simple Weisskopf-Ewing evaporation model³⁴ taking into account fission, and gamma competition to neutron emission. The pre-equilibrium emission of first neutron is included.

5.1 Model calculations of (n, nx) reaction spectra

The first neutron spectra for the (n, nx) reaction is the sum of evaporated and pre-equilibrium emitted neutron contributions. The pre-equilibrium emission contribution is calculated with a parameter systematics tested in case of $n+^{238}\text{U}$ and $n+^{235}\text{U}$ interactions^{25,28}. We have calculated the 1st, 2nd and 3d neutron spectra for the $(n, n\gamma)$, $(n, 2n)$ and $(n, 3n)$, where applicable. According to the ENDF/B-VI format we included the secondary neutron spectra in the following way. The calculated spectra were summed up and tabular spectra for the $(n, n\gamma)$, $(n, 2n)$ and $(n, 3n)$ reactions were obtained. To clarify the competition of neutron, γ -emission and fission in case of (n, nx) and $(n, 2nx)$ reactions we have chosen the following presentation of spectra. Figure 5.1 shows the spectrum of 1st neutron of the reaction (n, nx) and its partial contributions for $(n, n\gamma)$, $(n, 2n)$, (n, nf) $(n, 2nf)$ and $(n, 3n)$ reactions. Figure 5.2 shows the spectrum of 2nd neutron of the reaction $(n, 2nx)$ and its partial contributions for $(n, 2n)$, $(n, 3n)$ and $(n, 2nf)$ reactions. The spectra of 1st and 2nd neutrons are normalized to unity. The partial neutron spectra shown on figs. 5.1, 5.2 are normalized to the contributions of appropriate cross sections to the (n, nx) and $(n, 2nx)$ reaction cross sections, respectively.

Table 5.1 Average energies of secondary neutron spectra

E_n , MeV	1st neutron average energy, MeV									
	(n, n')		$(n, 2n)$		$(n, n'f)$		$(n, 3n)$		$(n, 2n'f)$	
	pres.	J - 3	pres.	J - 3	pres.	J-3	pres.	J - 3	pres.	J-3
2.0	0.52	0.83								
7.0	2.38	1.02	0.71	1.02	0.48					
14.0	9.86	1.47	4.14	1.47	2.82		0.56	1.47	1.11	
20.0	15.9	1.76	10.4	1.76	4.54		2.73	1.76	3.40	

E_n , MeV	2nd neutron average energy, MeV						3d neutron	
	(n, 2n)		(n, 3n)		(n, 2n'f)			
	pres.	J - 3	pres.	J - 3	pres.	J-3	pres.	J - 3
7.0	0.20	0.83						
14.0	0.83	0.99	0.48	1.03	0.77		0.16	0.84
20.0	0.79	1.37	1.19	1.37	1.19		0.67	0.81

The inclusion of pre-equilibrium emission changes significantly the average energies of emitted neutron spectra. That is shown in Table 5.1, where the average secondary neutron energies for current and JENDL-3 evaluations are compared. The most significant is the change of neutron spectra of (n,n γ) reaction. Figs 5.3-5.7 demonstrate the discrepancies of secondary neutron spectra in current and JENDL-3 evaluations.

The 1st neutron spectra of (n,nf) reaction also becomes harder and that influences prompt fission neutron spectra. On the other hand, the spectra of 2nd and 3d neutrons become softer.

5.2 Prompt fission neutron spectra

Prompt fission neutron spectra were calculated within the framework of Madland-Nix model³⁵.

5.2.1 Model calculations of prompt fission neutron spectra

The model parameters, which should be defined are the following.

5.2.1.1 Fragment masses. The fragment masses are defined as $A_L = 105$ and $A_H = 141$, in accordance with the data of Unik et al.³⁶. Fragment charges are defined as even values, closest to the ratios of

$$\langle A_{L,H} \rangle / (Z_{L,H} \mp 0.5) = A_F / Z_F.$$

The average fragments adopted are ^{105}Mo and ^{141}Xe .

5.2.1.2 Energy parameters. Average total fission energies $\langle E_R \rangle$ and average fission-fragment separation energies are calculated as in Madland-Nix model using mass tables of Wapstra et al.³⁷ Unik et al.³⁶ total fragment kinetic energy $\langle TKE \rangle = 184.2 \pm 0.5$ MeV for ^{246}Cm fissioning nuclei is used, for other fissioning nucleus $\langle TKE \rangle$ is calculated with Viola et al.³⁸ systematics:

$$\langle TKE \rangle = (0.1189 \pm 0.0011)Z^2/A^{1/3} + (7.3 \pm 1.5), \text{ MeV}$$

The resulted values of $\langle TKE \rangle$ are then varied to fit ν_p at thermal energy.

5.2.1.3 Other parameters. The level density parameter of the fermi-gas model is calculated as $a = A_{L,H}/10.2$, MeV^{-1} . Becchetti-Greenlees³⁹ spherical optical potential parameters are employed to calculate compound cross section.

5.2.2 Prompt fission neutron spectra evaluation

Below emissive fission threshold prompt fission neutron spectra are calculated with the parameters given in Table 5.2.

Table 5.2

Parameters of the Madland-Nix model

Fissioning nucleus	A_L fragm.	A_H fragm.	$\langle E_R \rangle$, MeV	$\langle TKE \rangle$, MeV	B_n , MeV
²⁴⁶ Cm	¹⁰⁵ Mo	¹⁴¹ Xe	208.340	183.700	6.455
²⁴⁵ Cm	¹⁰⁴ Mo	¹⁴¹ Xe	208.564	185.000	5.522
²⁴⁴ Cm	¹⁰⁴ Mo	¹⁴⁰ Xe	209.722	185.800	6.799

Figure 5.8 shows the comparison of calculated thermal prompt fission neutron spectrum with maxwellian spectrum ($T = 1.395 \text{ MeV}$) of JENDL-3. Average energy of fission spectrum is 2.20 MeV, it is compatible with measured datum of $2.25 \pm 0.08 \text{ MeV}$ of Krohskin and Zamyatnin⁴⁰. Figure 5.9 demonstrates the increasing differences of our calculation and JENDL-3 evaluation due to incident neutron energy independent maxwellian fission spectrum presentation in JENDL-3.

Above emissive fission threshold the fission neutron spectra $N(E)$ is the superposition of emissive fission spectra, i.e.

$$\begin{aligned}
 N(E) = & \left(\frac{\sigma_{nf}}{\sigma_{nF}} \nu_1 N_1(E) + \frac{\sigma_{nn'f}}{\sigma_{nF}} [\Phi_{nn'f}(E) + \nu_2 N_2(E)] \right. \\
 & \left. + \frac{\sigma_{n2nf}}{\sigma_{nF}} [\Phi_{n2nf}^1(E) + \Phi_{n2nf}^2(E) + \nu_3 N_3(E)] \right) / \\
 & \left[\frac{\sigma_{nf}}{\sigma_{nF}} \nu_1 + \frac{\sigma_{nn'f}}{\sigma_{nF}} (1 + \nu_2) + \frac{\sigma_{n2nf}}{\sigma_{nF}} (2 + \nu_3) \right],
 \end{aligned}$$

where σ_{nF} , σ_{nf} , $\sigma_{nn'f}$, σ_{n2nf} are the total and i-th chance fission cross sections ($i = 1, 2, 3$); $\Phi_{nn'f}$, Φ_{n2nf}^1 , and Φ_{n2nf}^2 are emitted neutron spectra: for (n,nf) reaction, 1st and 2nd neutrons of (n,2nf) reaction, respectively; ν_i and N_i are multiplicity and prompt neutron spectra for the i-th fissioning nucleus. The pre-equilibrium emission of the first neutron is included, the $\Phi_{n,xnf}^i$ spectra for the emissive fission are calculated with the model, described in 5.1

Table 5.3 Comparison of Madland-Nix and present approach

Quantity	$E_n = 7 \text{ MeV}$		$E_n = 14 \text{ MeV}$	
	M-N model ²⁸	This work	M-N model ²⁸	This work
$\langle E_1 \rangle$	2.353	2.353	2.492	2.492
ν_1	4.477	4.477	5.224	5.224
$\langle E_{n'f} \rangle$	1.083	0.484	1.518	2.822
$\langle E_2 \rangle$	2.174	2.190	2.324	2.295
ν_2	3.291	3.372	4.160	3.990
$\langle E_{2nf} \rangle^1$	-	-	1.518	1.114
$\langle E_{2nf} \rangle^2$	-	-	1.083	0.765
$\langle E_3 \rangle$	-	-	2.191	2.208
ν_3	-	-	3.306	3.402
$\langle E \rangle$	2.258	2.230	2.358	2.435
ν	4.435	4.453	5.298	5.241

The influence of pre-equilibrium prefission neutrons on prompt fission neutron multiplicity ν_i and prompt neutron spectra N_i predictions as well as $N(E)$ and $\nu(E)$, is illustrated in Table 5.3 and Fig. 5.10 for two incident neutron energies. Here $\langle E_i \rangle$ denotes average prompt fission neutron energy of i-th fissioning nucleus, $\langle E \rangle$ is the average fission neutron energy, $\langle E_{n'f} \rangle$, $\langle E_{2nf} \rangle^1$ and $\langle E_{2nf} \rangle^2$ are the average energies of neutrons, emitted in (n,nf) and 1st and 2nd neutrons emitted in (n,2nf) reactions, respectively. The fig. 5.11 shows the partial contributions of ith-chance fission to the total fission neutron spectrum at incident neutron energy of 14 MeV.

6 Number of neutrons per fission

The number of prompt fission neutrons at thermal energies was measured in 1970 by Kroshkin and Zamyatnin⁴⁰ and Jaffey et al.⁴¹ Simple renormalization of these data to the recent reference values of ν_p for ²³³U, ²³⁵U, ²³⁹Pu and ²⁵²Cf seems incorrect. The measurements by Howe et al.⁴² of $\nu_p(E)$ gives the anomalous value of $d\nu_p/dE = 0.08 \pm 0.015$, which is considerably

lower than that, found for other measured neighboring nuclei. The recent data of Khokhlov et al.⁴³ agree with data by Howe et al.⁴² below 4 MeV. At higher incident neutron energies they are systematically higher, while appropriate value of $d\nu_p/dE = 0.146 \pm 0.009$ is consistent with other neighboring nuclei data. The present evaluation of ν_p is based on calculation within Madland-Nix model, fitted to the data of Khokhlov et al.⁴³ in the energy range 0.5÷4 MeV. The calculated $d\nu_p/dE = 0.133$ is considerably higher than that of Howe et al.⁴². However calculated ν_p is roughly consistent with data by Khokhlov et al.⁴³ above 4 MeV, although it can not be increased any further. The comparison of $\nu_p(E)$ with measured data, JENDL-3 and ENDF/B-VI evaluations is shown in fig. 6.1. The Madland-Nix model calculations predict non-linear increase of $\nu_p(E)$ above emissive threshold. The influence of pre-equilibrium pre-fission neutrons manifests in additional appreciable decrease of $d\nu_p/dE$ above 12 MeV.

For incident neutron energy from thermal up to 0.3 MeV we adopted constant value of $\nu_p = 3.59$. This behavior follows from the measured data for several uranium and plutonium nuclei, and agrees with data by Howe et al.⁴² in this region.

The delayed number of neutrons per fission ν_d is from Brady et al.⁴⁴ and systematics of Tuttle⁴⁵. Specifically, $\nu_d = 0.0064$ for incident neutron energies up to 6 MeV and $\nu_d = 0.0044$ for $E_n \geq 8$ MeV. The decay constants for six groups of delayed neutrons are taken from Brady et al.⁴⁴

7 Angular distributions of secondary neutrons

The angular distributions of elastically scattered neutrons and those for neutrons, scattered on three levels of ground state band are calculated with the coupled channel method. The isotropic compound scattering contribution is taken into account by renormalizing l-th Legendre polynomial coefficients A_l^{cc} , calculated with coupled channels:

$$A_l = A_l^{cc} \sigma_{dir} / (\sigma_{dir} + \sigma_{comp}),$$

where σ_{dir} and σ_{comp} are the direct and compound contributions to the scattering cross section, respectively. All the other contributing reactions angular distributions of secondary neutrons are assumed isotropic.

8 Conclusions

The evaluated neutron data file for ²⁴⁵Cm is compiled in ENDF/B-VI format and sent to the International Science and Technology Center (Moscow) and

Japan Nuclear Data Center at Japan Atomic Energy Research Institute.

The scarcity of experimental data coupled with possibility of some new data becoming available (for example, $^{245}\text{Cm}(n,f)$ data of Fursov et al. (PPEI, Obninsk, Russia) may urge some revision of data file. Present version of ^{245}Cm data file may be revised before March of 1998, the expiration date of Project CIS-03-95.

9 REFERENCES

1. Nakagawa T., Kikuchi Y., Proc. of the Int. Conf. on Nuclear Data and Technology, Gatlinburg, Tenn., USA, 9-13 May, 1994, Dickens J.K. (Editor), 709, ANS Inc., 1994.
2. Maslov V.M., Porodzinskij Yu.V., Sukhovitskij E.Sh., Klepatskij A.B., Morogovskij G.B. INDC, 1995, in print
3. Japanese Evaluated Data Library, Version 3, JAERI 1319, 1990.
4. C.L. Dunford, Nuclear Data for Science and Technology, Proc. Int. Conf. Julich, 1991, 788. Springer-Verlag, 1992, Berlin
5. Browne J.C., Benjamin R.W., Karraker D.G. Nucl. Sci. Engng. 65, 166 (1978)
6. Moore M.S., Keyworth G.A. Phys. Rev. C, 3, 1656 (1971)
7. Belanova T.S., Kolesov A.G., Poruchikov V.A. et al., Neutron Physics, v.2, 260 (1977)
8. Halperin J., Drusched R.E., Eby R.E. ORNL-4437, 20 (1969)
9. Thomson M.C., Hyder M.L., Reuland R.J. J. Inorg. Nucl. Chem. 33, 1533 (1971)
10. Benjamin R.W., Macmurdo K.W., Spences J.D. Nucl. Sci. Eng. 47, 203 (1972)
11. Zhuravlev K.D., Kroshkin N.I., Chetverikov Atomnaya Energiya, 39, 907 (1976)
12. Gavrilov V.D. Goncharov V.A., Ivanenko V.V. Atomnaya Energiya 41, 808 (1977)
13. Mughabghab S.F.: "Neutron Cross Sections, v1, part B", Academic Press (1984).
14. Dunford C.L.: "ENDF Utility Codes Release 6.9", IAEA-NDS-29 (1993)
15. Porodzinskij Yu.V., Sukhovitskij E.Sh., Nuclear Constants, 4, p.27, 1987 (in Russian)
16. Ignatjuk A.V., Istekov K.K., Smirenkin G.N. Sov. J. Nucl. Phys. 29, 450 (1979).
17. Gerasimov V.F., Danitchev V.V., Dementiev V.N., et al., Proc. of 1st Int. Conf. on Neutron Physics, 14-18 Sept., Kiev, USSR, V.3, p.85, 1988.
18. White R.M., Browne J.C. , in: Nuclear Data for Science and Technology (North-Holland, 1983), p.281.
19. Fomushkin E.F., G.F. Novoselov, Y.I. Vinogradov et al., Atomnaya Energiya, 69, 258 (1990).
20. Fomushkin E.F., Novoselov G.F., Gavrilov G.F. et al., in: Nuclear Data for Science and Technology (Springer-Verlag, 1992), p.439.
21. Fursov B.I., Samylin B.F., Smirenkin G.N., et al. Nuclear Data for Science and Technology, Proc. Int. Conf., Gatlinburg, 1994, 269, ANS.
22. Haouat, Lachkar J., Lagrange Ch., et al., Nucl.Sci. Engng. 81, 491

(1982)

23. Klepatskij A.B., Sukhovitskij E.Sh., private communication.
24. Ellis-Akovali Y.A., Nucl. Data Sheets, 44, 407 (1985)
25. Ignatjuk A.V., Maslov V.M., Proc. Int. Symp. Nuclear Data Evaluation Methodology, Brookhaven, USA, October 12-16, 1992, p.440, World Scientific, 1993.
26. Howard W.M., Moller P. Atomic Data and Nuclear Data Tables, 25, 219 (1980)
27. Tepel J.W., Hoffman H.M., Weidenmuller H.A. Phys. Lett. 49, 1 (1974).
28. Ignatjuk A.V., Maslov V.M., Pashchenko A.B. Sov. J. Nucl. Phys. 47, 224 (1988).
29. Uhl M. and Strohmaier B., Report IRK - 76/10 (Vienna, 1976).
30. Fomushkin E.F., Novoselov G.F., Vinogradov Yu.I., Gavrilov G.F., Zherebtsov Sov. J. Nucl. Phys. 36, 338 (1980).
31. Vorotnikov P.E. et al. Sov. J. At. Energy 57, 504 (1985).
32. Klepatskij A.B., Kolesov A.M., Maslov V.M., Porodzinskij Yu.V., Sukhovitskij E.Sh., INDC(CCP)-316, 1989
33. Maslov V.M. Zeit. Phys. A, Hadrons & Nuclei, 347, 211 (1994).
34. Maslov V.M., Porodzinskij Yu.V., Sukhovitskij E.Sh., Proc. Int. Conf. on Neutron Physics, 14-18 Sept., Kiev, USSR, V.1, p.413, 1988.
35. Madland D.G., Nix J.R., Nucl. Sci. Engng. 81, 213 (1982).
36. Unik J.P. et al. Physics and Chemistry of Fission, Proc. of a Symp., Rochester, NW, USA, 13-17 August, 1973, v.II, p. 19, IAEA, Vienna, 1974.
37. Wapstra A.H. et al. At. Data & Nucl. Data Tables, 39, 281 (1988).
38. Viola V.E., Kwiatkowski K., Walker M., Phys. Rev., 31, 1550 (1985).
39. Becchetti F.D., Greenlees G.W., Phys. Rev. 182, 1190 (1969).
40. Kroshkin N.I. and Zamyatnin Yu.S., Atomnaya Energiya, 29, 95 (1970).
41. Jaffey A.H., Lerner J.L., Nucl. Phys. A, 145, 1 (1970).
42. Howe R. E. et al., Nuclear Physics, A407, 193 (1983).
43. Khokhlov Yu. A. et al., Nuclear Data for Science and Technology, Proc. of the Int. Conf., Gatlinburg, Tennessee, USA, May 9-13, 1994, v. I, p. 272.
44. Brady M.C. and England T.R., Nucl. Sci. Engng. 103, 129 (1989).
45. Tuttle R.J. Proc. Consultants Meeting on Delayed Neutron Properties, 1979, Vienna, INDC(NDS)-107/G, p.29.

10 Figure captions

- Fig. 2.1 Fission cross section of ^{245}Cm .
Fig. 2.2 Fission cross section of ^{245}Cm in the energy region 1.5-26 eV.
Fig. 2.3 Fission cross section of ^{245}Cm in the energy region 26-40 eV.
Fig. 2.4 Fission cross section of ^{245}Cm in the energy region 40-60 eV.
Fig. 2.5 Fission cross section of ^{245}Cm in the energy region 60-100 eV.
Fig. 2.6 Distribution of reduced neutron widths for $J=3$ resonances of ^{245}Cm .
Fig. 2.7 Neutron resonance spacing distribution for ^{245}Cm , $J=3$.
Fig. 2.8 Distribution of reduced neutron widths for $J=4$ resonances of ^{245}Cm .
Fig. 2.9 Neutron resonance spacing distribution for ^{245}Cm , $J=4$.
Fig. 2.10 Distribution of radiative widths for ^{245}Cm .
Fig. 3.1 Cumulative sum of neutron resonance levels of ^{245}Cm ; * marks energy intervals, omitted from the analysis
Fig. 3.2 Distribution of reduced neutron widths for ^{245}Cm .
Fig. 3.3 Neutron resonance spacing distribution for ^{245}Cm .
Fig. 3.4 Fission cross section of ^{245}Cm in unresolved resonance region.
Fig. 3.5 Radiative capture cross section of ^{245}Cm in unresolved resonance region.
Fig. 4.1 Compound reaction cross section of ^{245}Cm .
Fig. 4.2 Total cross section of ^{245}Cm .
Fig. 4.3 Elastic scattering cross section of ^{245}Cm .
Fig. 4.4 Fission cross section of ^{245}Cm
Fig. 4.5 Fission cross section of ^{245}Cm
Fig. 4.6 Fission cross section of ^{245}Cm
Fig. 4.7 Fission cross section of ^{244}Cm .
Fig. 4.8 Fission cross section of ^{245}Cm
Fig. 4.9 Cumulative number of levels of ^{245}Cm
Fig. 4.10 Cumulative number of neutron resonance levels for ^{244}Cm .
Fig. 4.11 Inelastic scattering cross section of ^{245}Cm .
Fig. 4.12 Cross section of ^{245}Cm : 0.0548 MeV, $9/2^+$ level excitation.
Fig. 4.13 Cross section of ^{245}Cm : 0.1215 MeV, $11/2^+$ level excitation.
Fig. 4.14 Cross section of ^{245}Cm : 0.1974 MeV, $13/2^+$ level excitation.
Fig. 4.15 Cross section of ^{245}Cm : 0.2923 MeV, $15/2^+$ level excitation.
Fig. 4.16 Cross section of ^{245}Cm : 0.3957 MeV, $17/2^+$ level excitation.
Fig. 4.17 Radiative capture cross section of ^{245}Cm .
Fig. 4.18 $^{245}\text{Cm}(n,2n)$ reaction cross section
Fig. 4.19 $^{245}\text{Cm}(n,3n)$ reaction cross section

Fig. 5.1 Components of first neutron spectrum of ^{245}Cm for incident neutron energy 14 MeV.

Fig. 5.2 Components of second neutron spectrum of ^{245}Cm for incident neutron energy 14 MeV.

Fig. 5.3 Comparison of $(n,n'\gamma)$ reaction neutron spectra of ^{245}Cm for incident neutron energy 8 MeV.

Fig. 5.4 Comparison of $(n,2n)$ reaction neutron spectra of ^{245}Cm for incident neutron energy 8 MeV.

Fig. 5.5 Comparison of $(n,n'\gamma)$ reaction neutron spectra of ^{245}Cm for incident neutron energy 14 MeV.

Fig. 5.6 Comparison of $(n,2n)$ reaction neutron spectra of ^{245}Cm for incident neutron energy 14 MeV.

Fig. 5.7 Comparison of $(n,3n)$ reaction neutron spectra of ^{245}Cm for incident neutron energy 14 MeV.

Fig. 5.8 Thermal prompt fission neutron spectrum.

Fig. 5.9 Calculated fission neutron spectra of ^{245}Cm ratio to JENDL-3 evaluation ($T_{\text{maxw}} = 1.395$).

Fig. 5.10 Fission neutron spectra of ^{245}Cm ratio to standard Madland-Nix model calculation for incident neutron energies 7 and 14 MeV.

Fig. 5.11 Fission neutron spectra of ^{245}Cm for incident neutron energy 14 MeV.

Fig. 6.1 Prompt fission neutron multiplicity for ^{245}Cm .

^{245}Cm FISSION CROSS SECTION

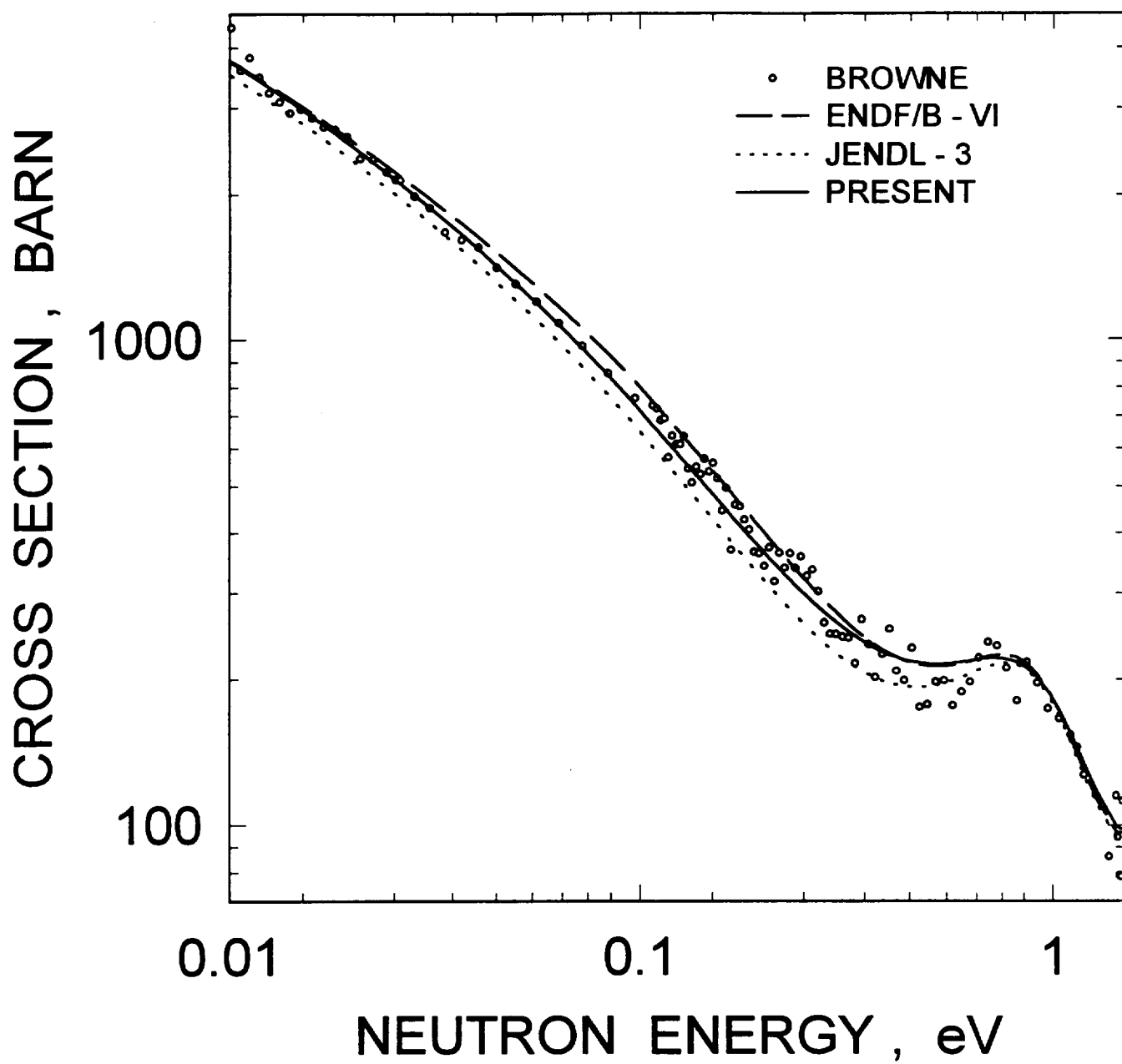


FIG. 2.1

^{245}Cm FISSION CROSS SECTION

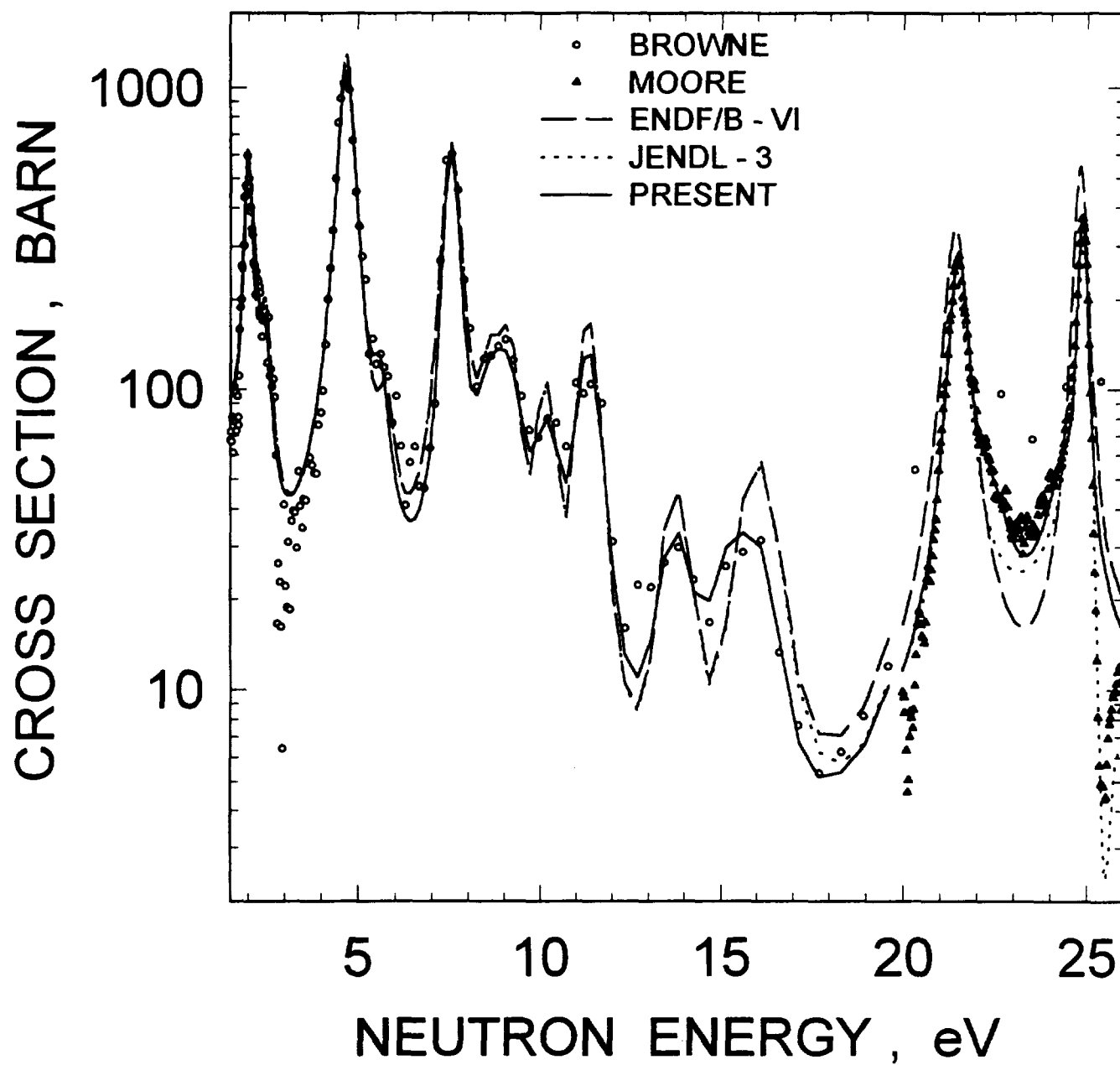


FIG. 2.2

^{245}Cm FISSION CROSS SECTION

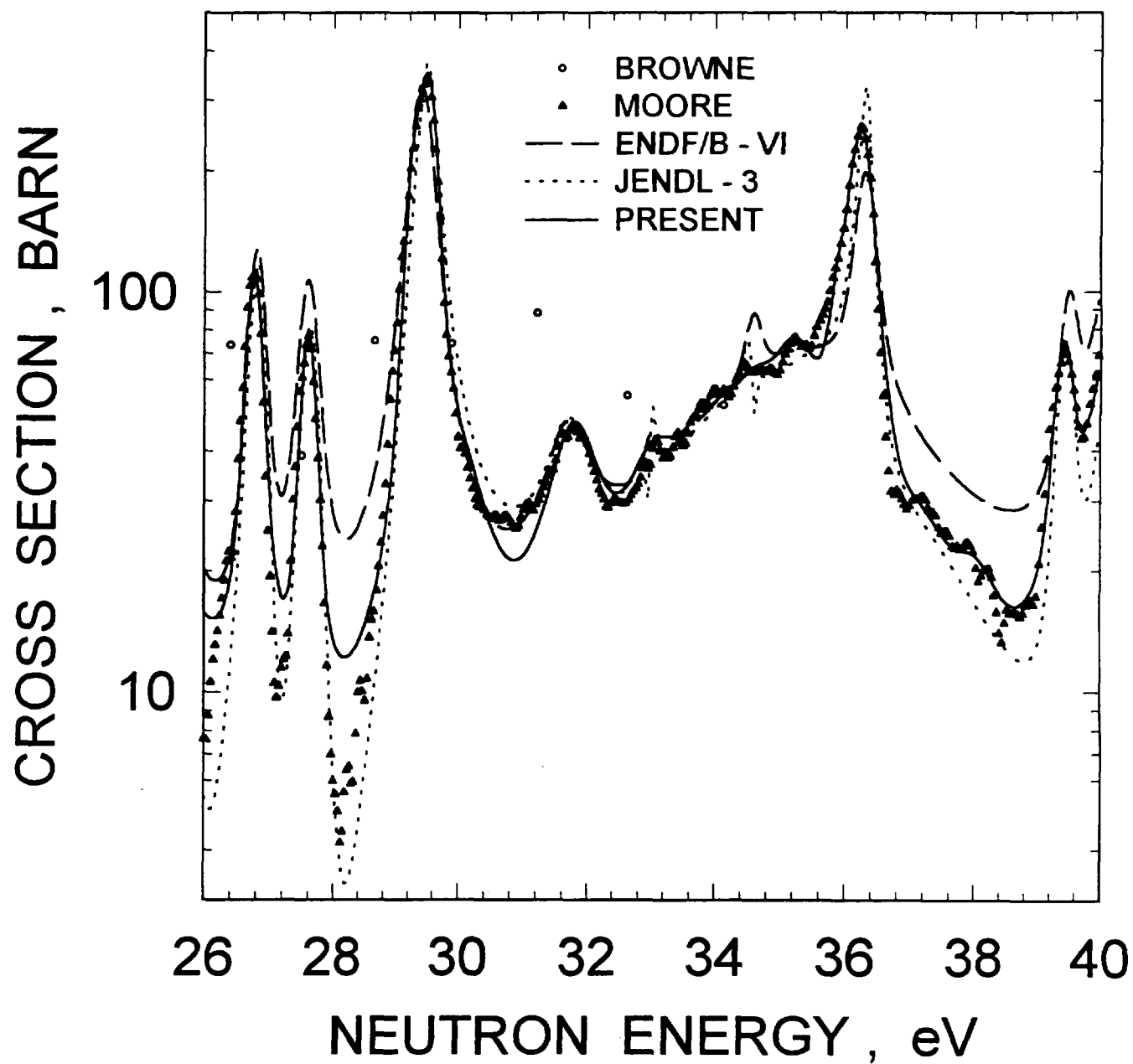


FIG. 2.3

^{245}Cm FISSION CROSS SECTION

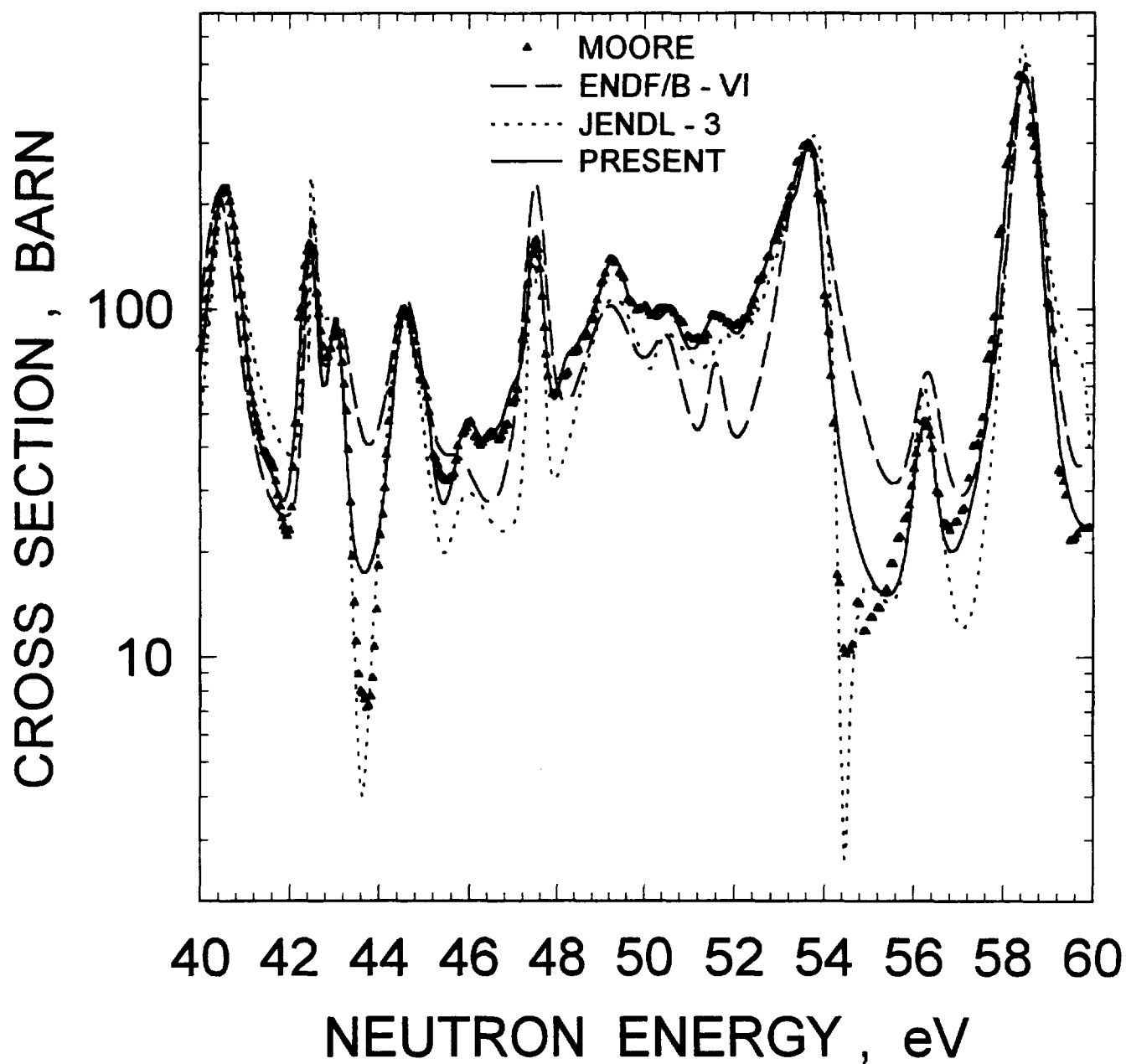


FIG. 2.4

^{245}Cm FISSION CROSS SECTION

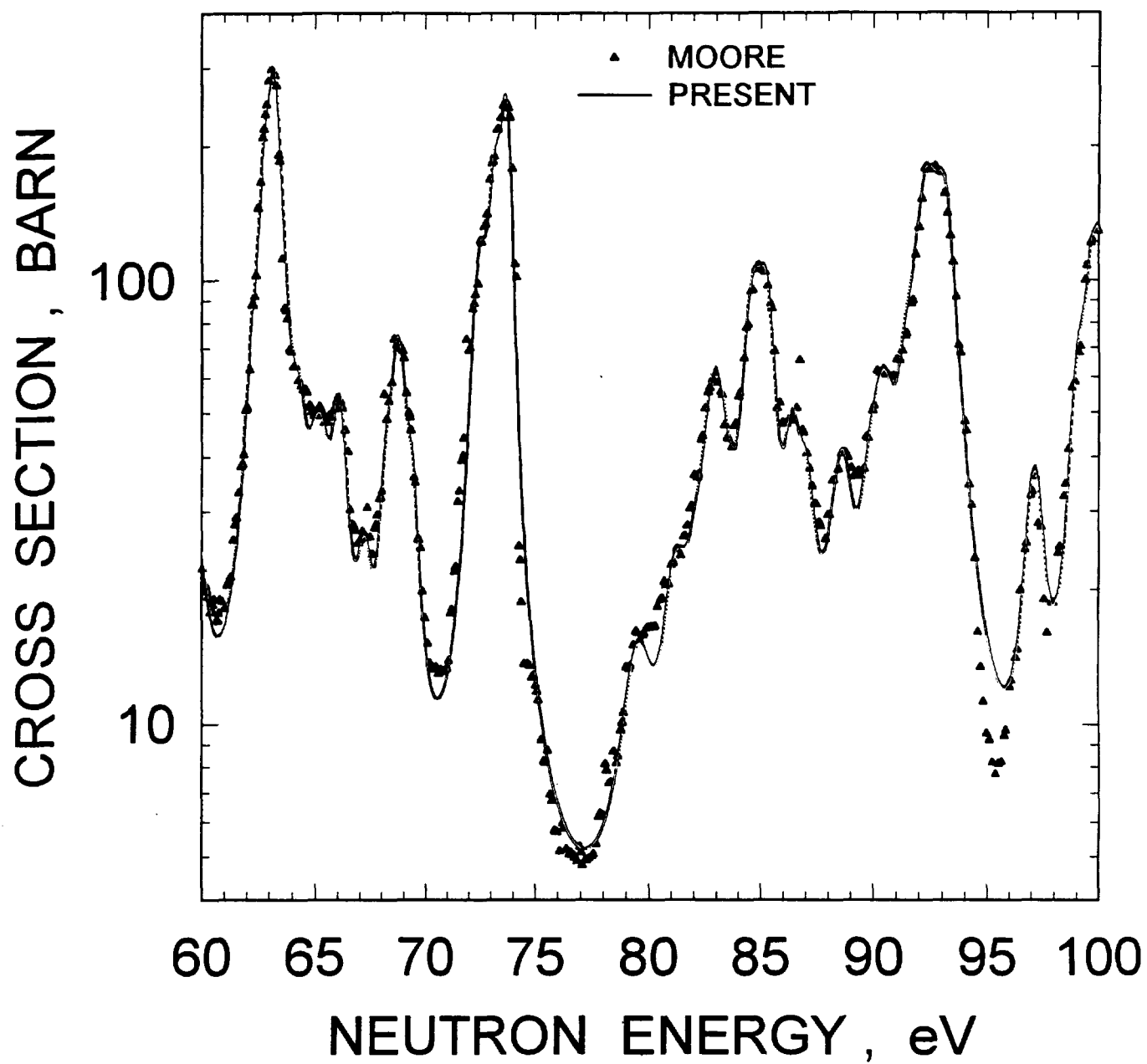


FIG. 2.5

^{245}Cm DISTRIBUTION OF REDUCED
NEUTRON WIDTHS

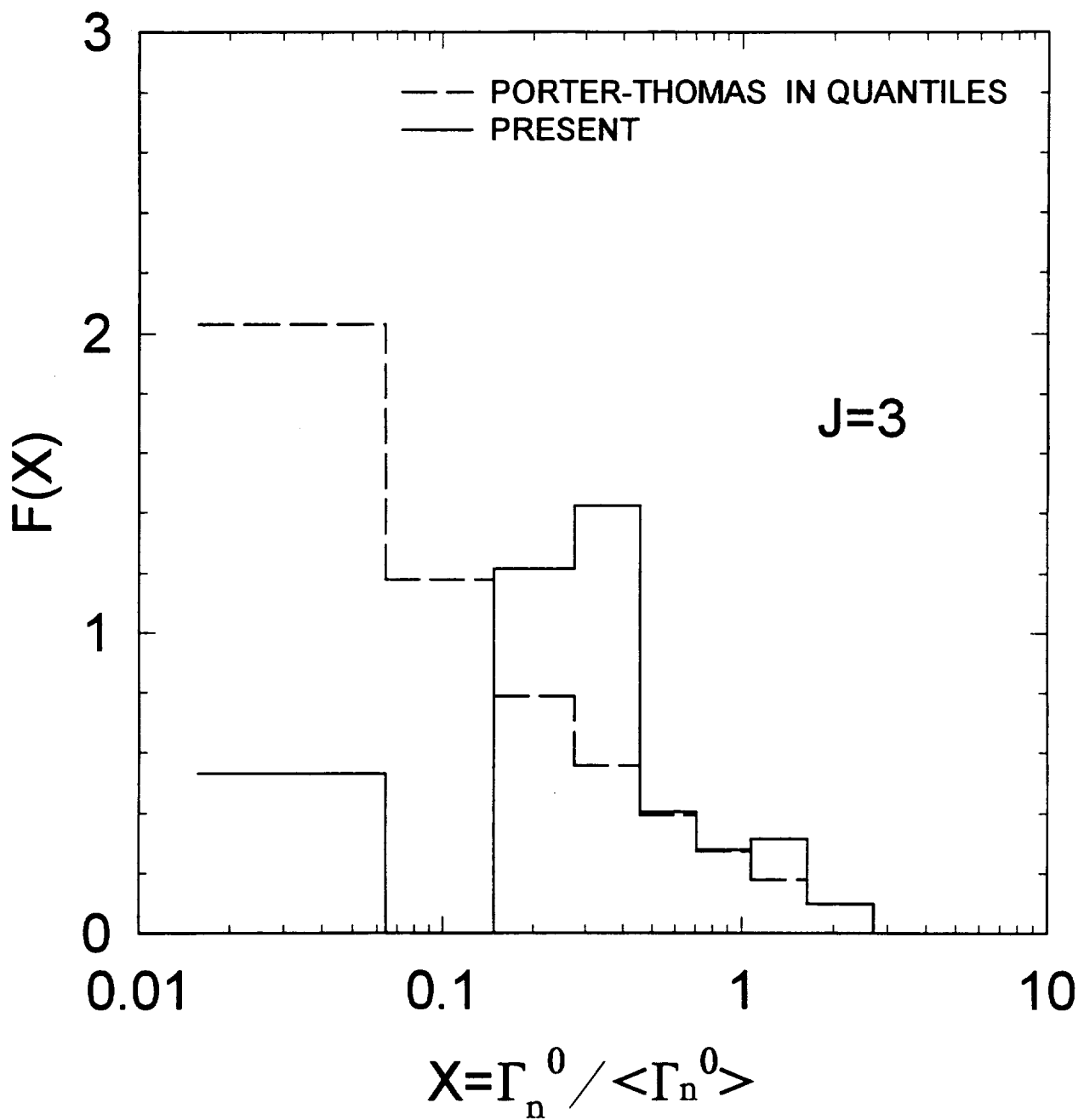


FIG. 2.6

^{245}Cm LEVEL SPACING DISTRIBUTION

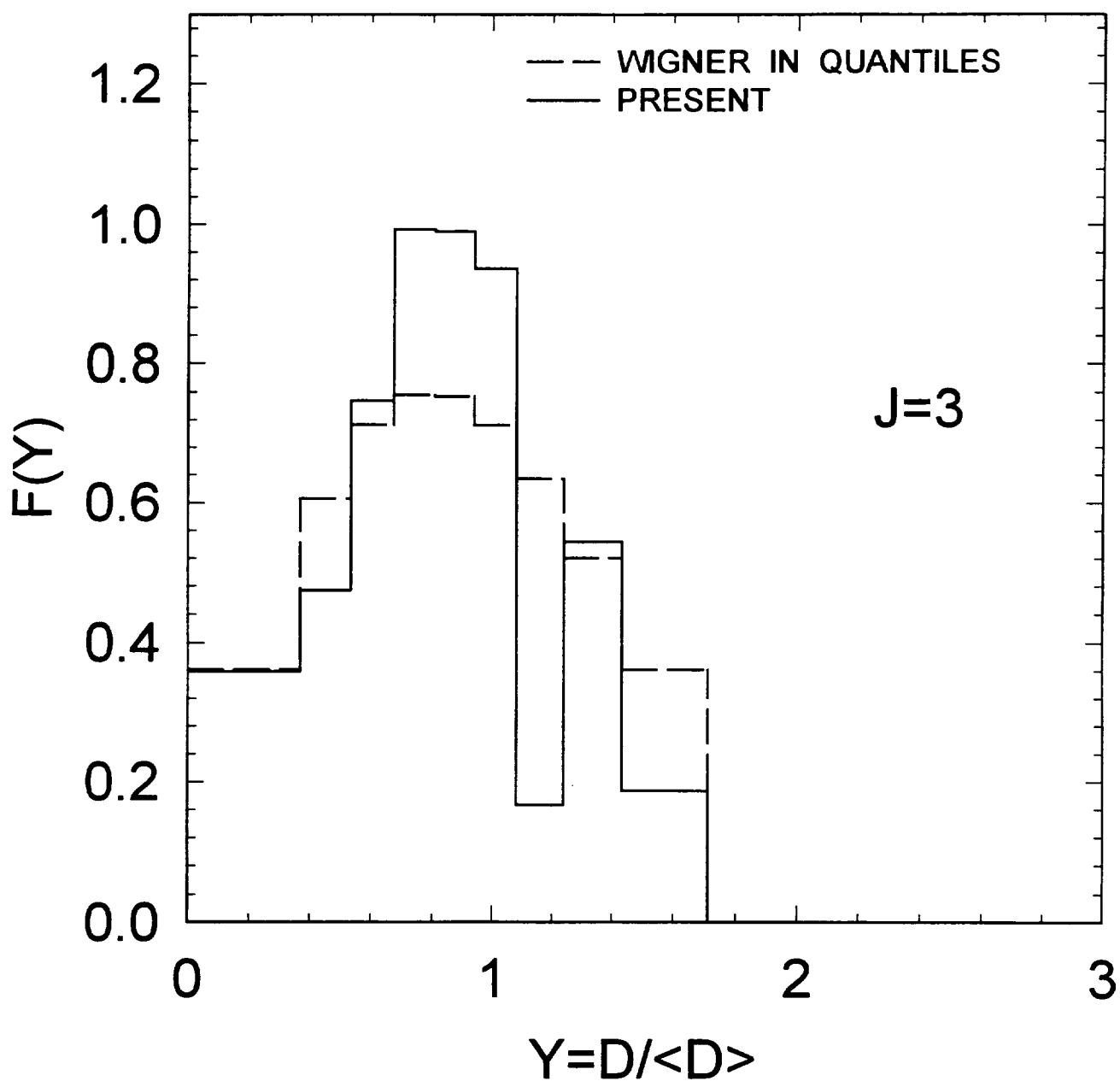


FIG. 2.7

^{245}Cm DISTRIBUTION OF REDUCED NEUTRON WIDTHS

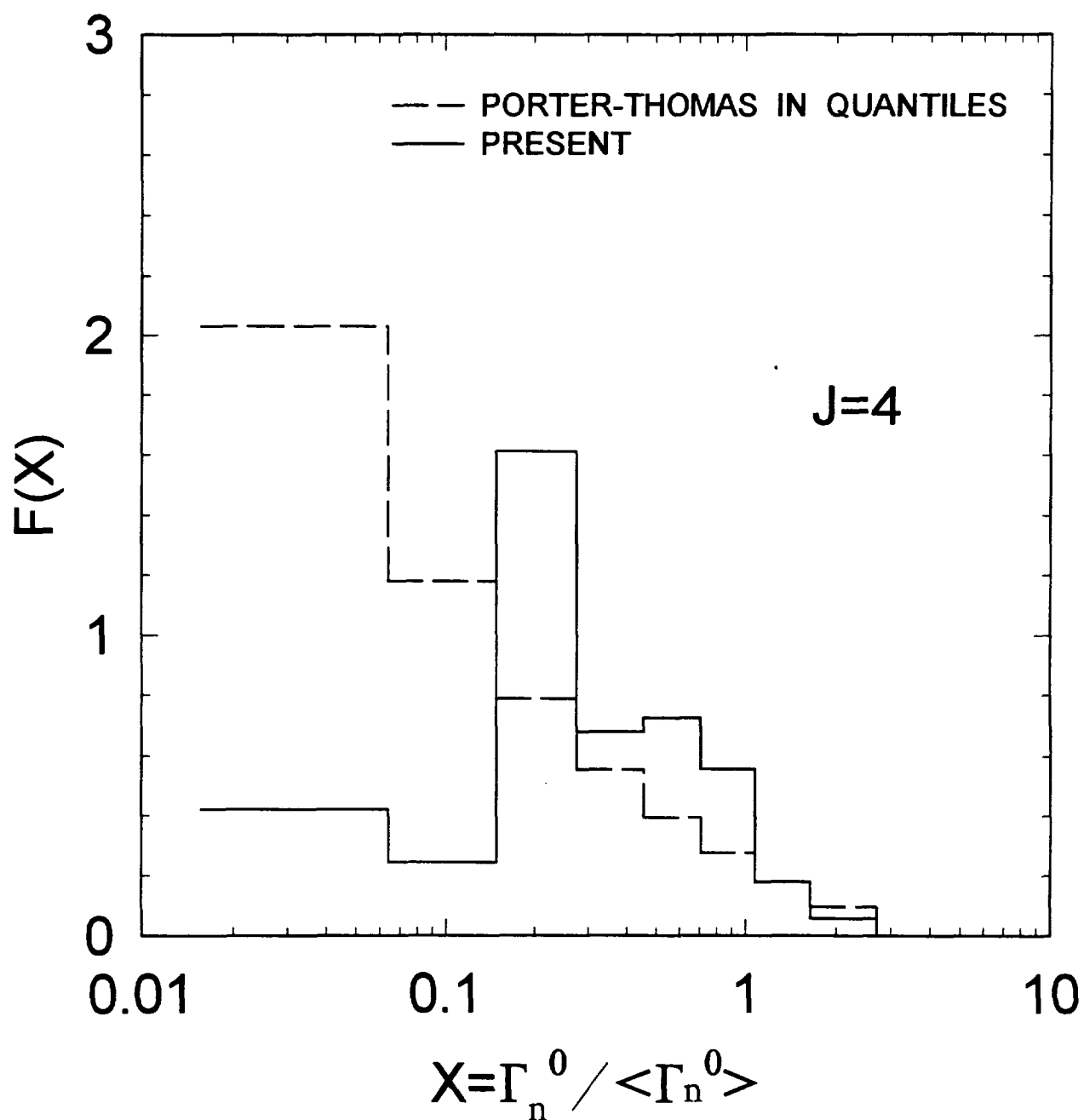


FIG. 2.8

^{245}Cm LEVEL SPACING DISTRIBUTION

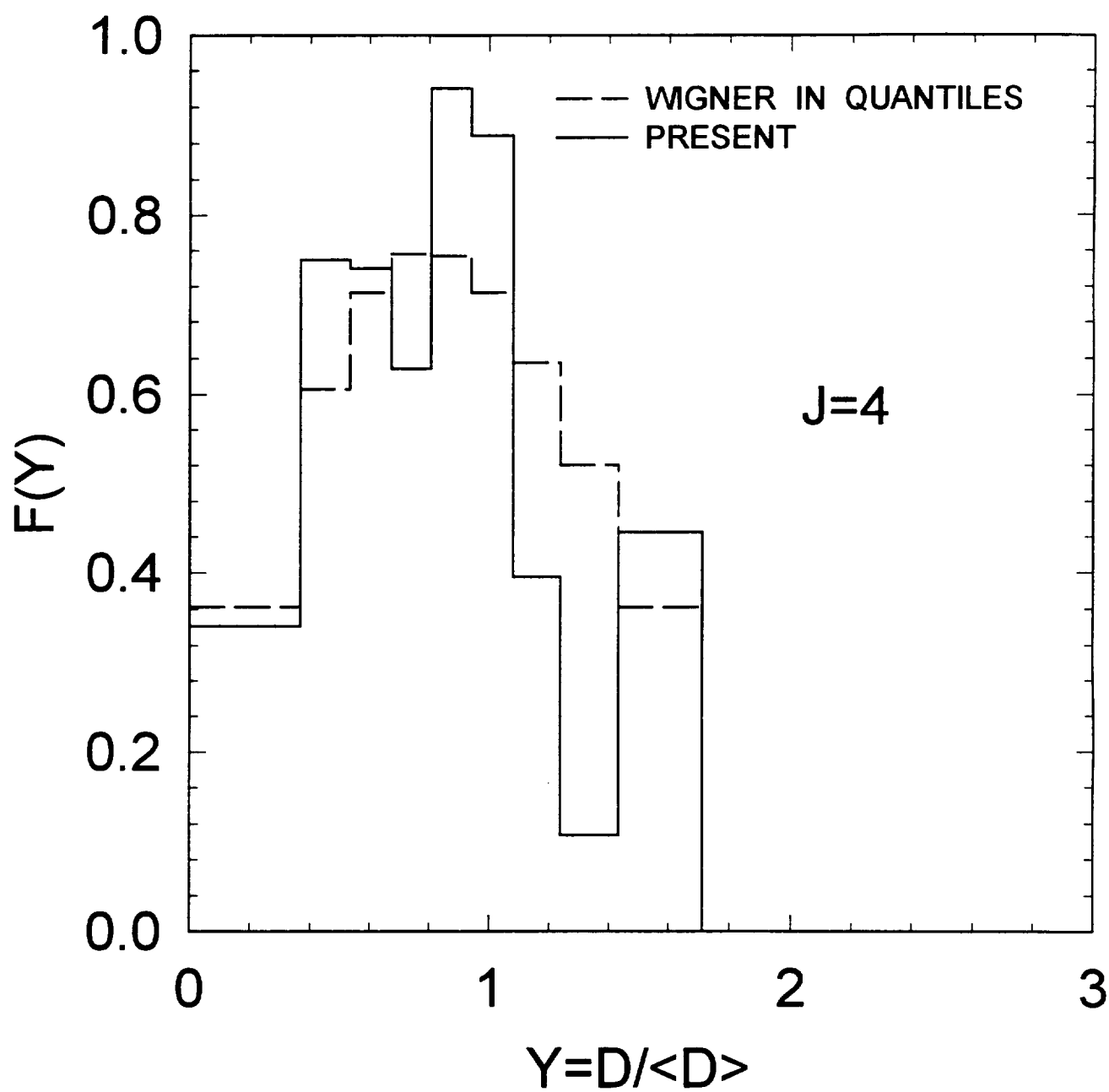


FIG. 2.9

²⁴⁵Cm DISTRIBUTION OF CAPTURE WIDTHS

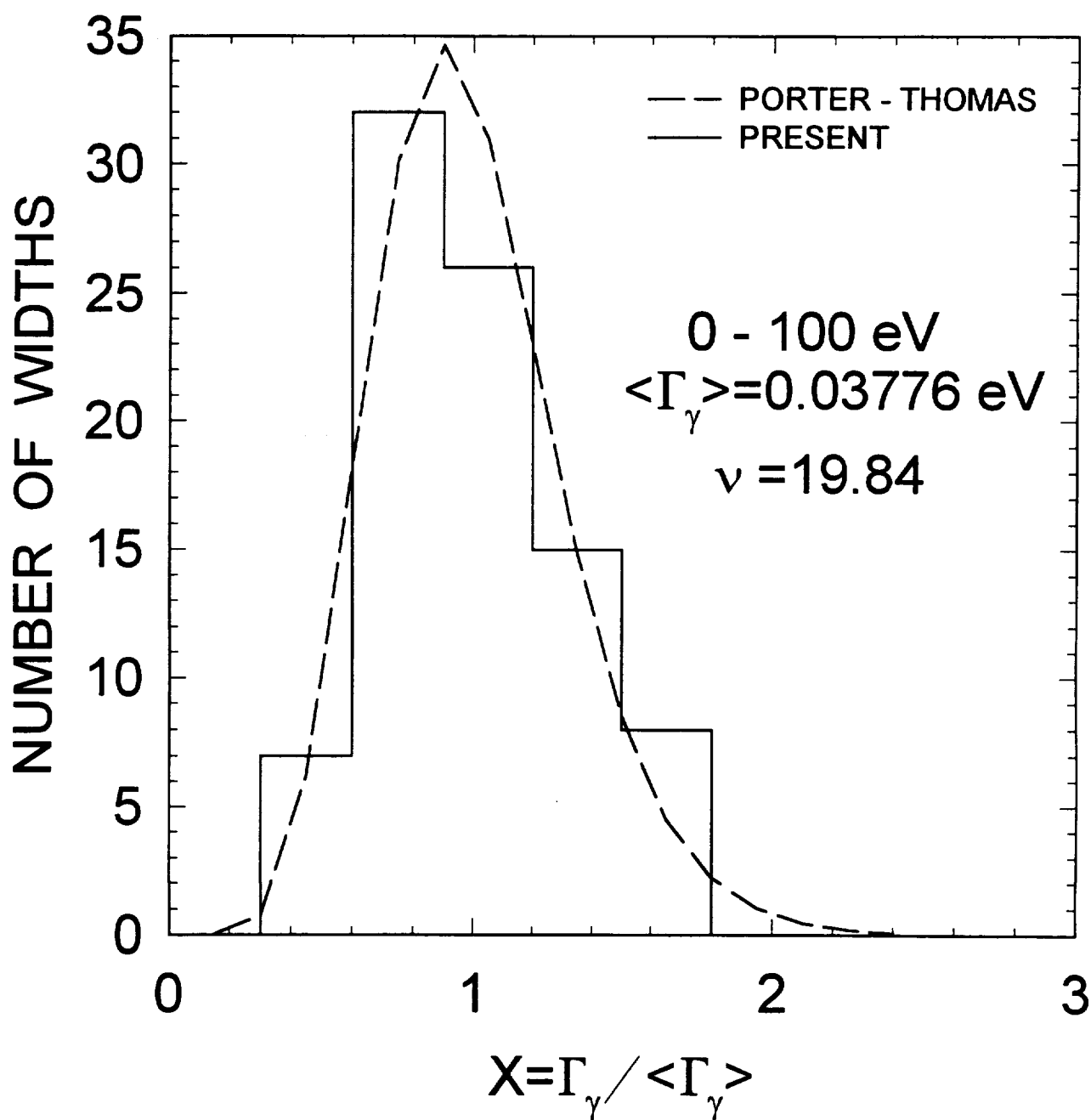


FIG. 2.10

^{245}Cm CUMULATIVE SUM OF LEVELS

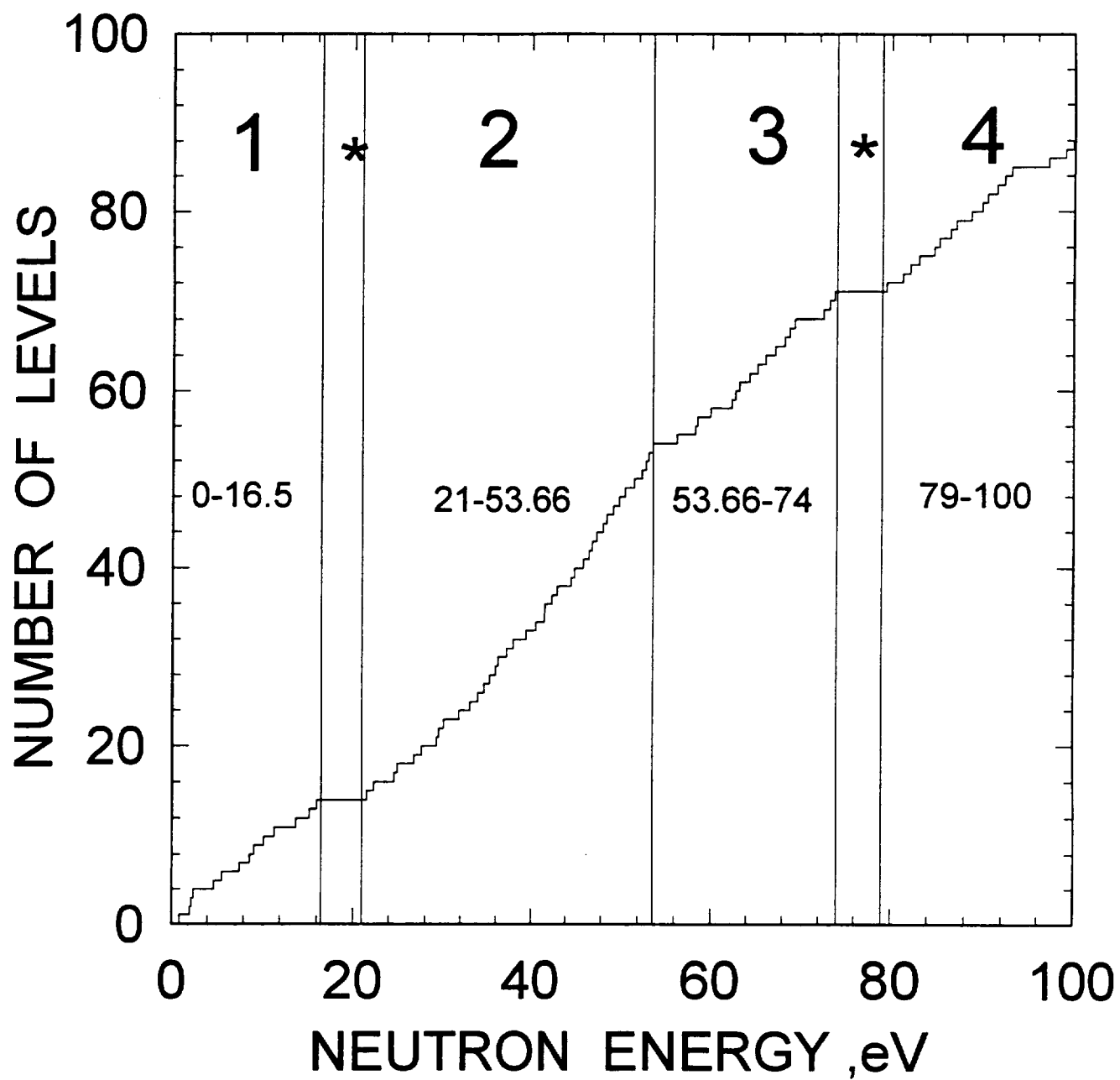


FIG.3.1

²⁴⁵Cm REDUCED NEUTRON WIDTH DISTRIBUTION

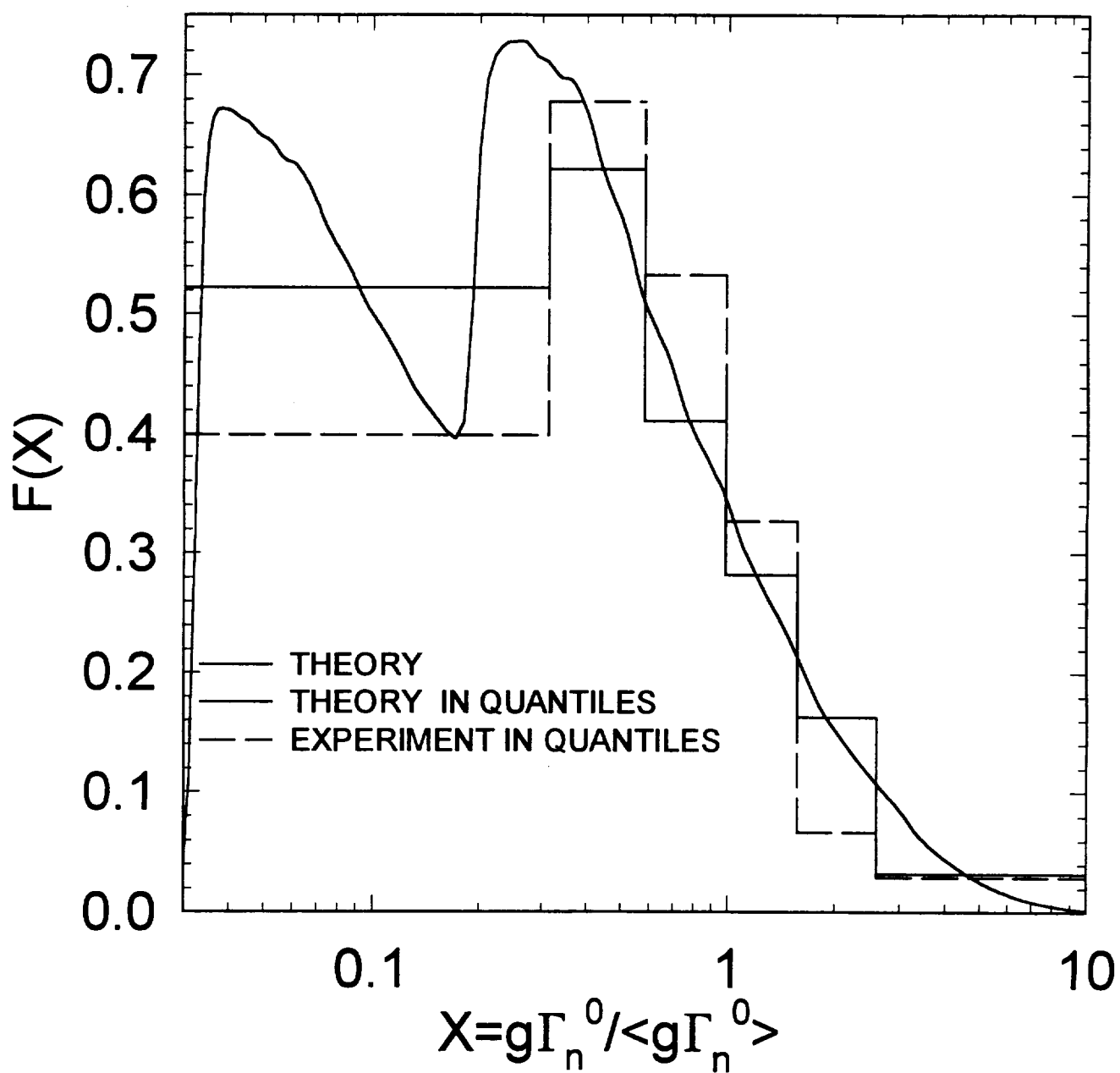


FIG.3.2

²⁴⁵Cm LEVEL SPACING DISTRIBUTION

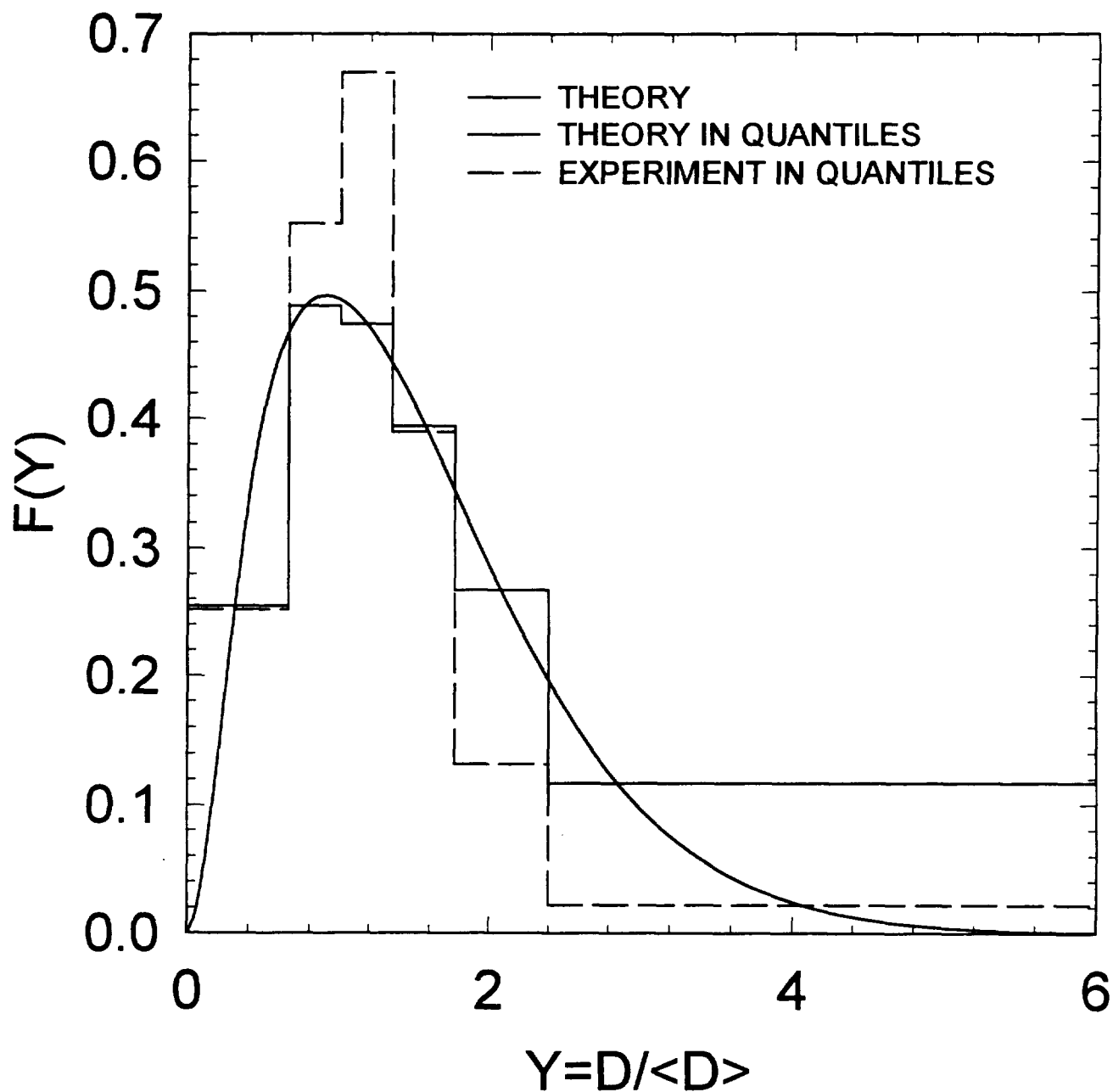


FIG.3.3

^{245}Cm FISSION CROSS SECTION

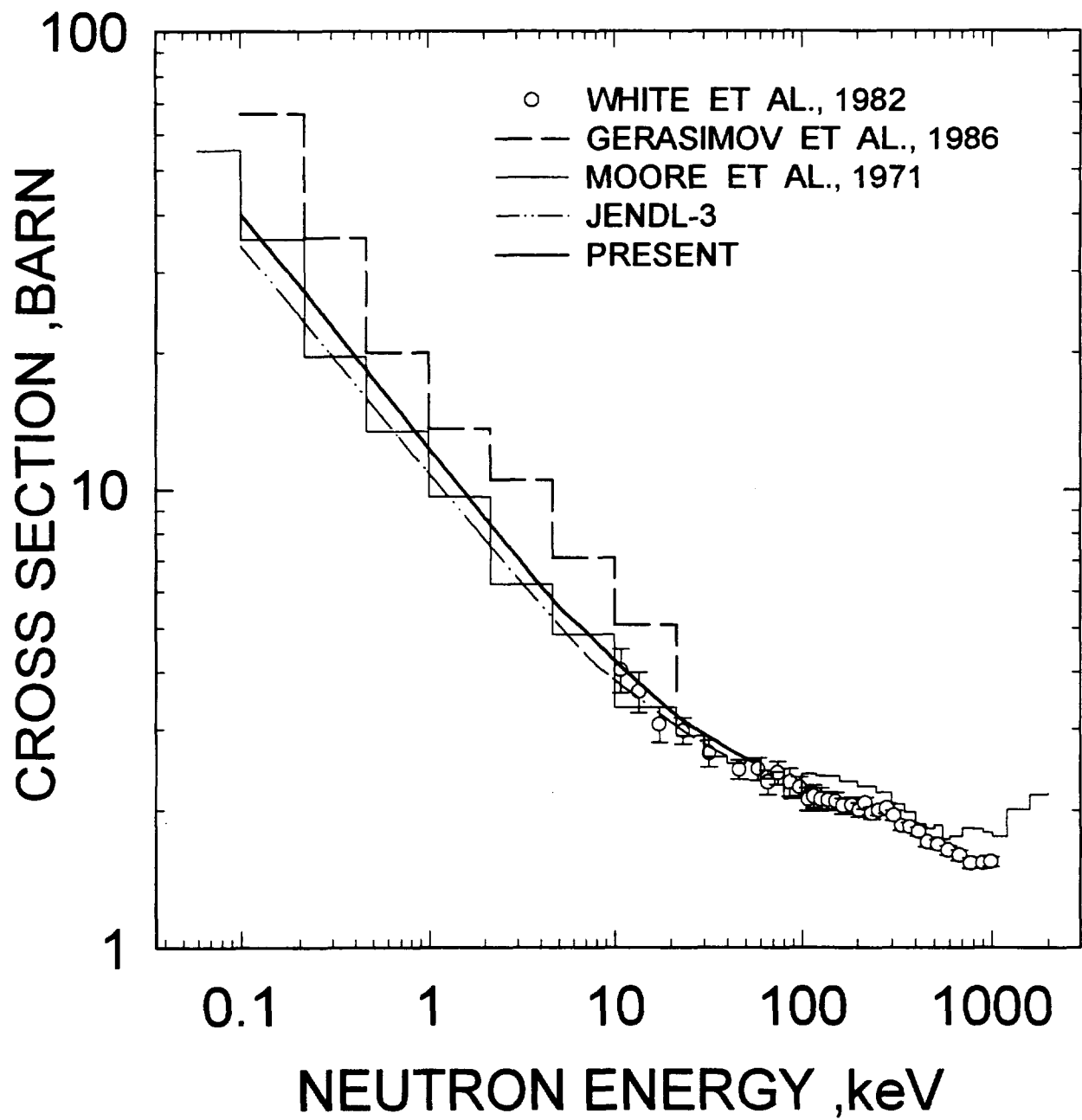


FIG.3.4

^{245}Cm CAPTURE CROSS SECTION

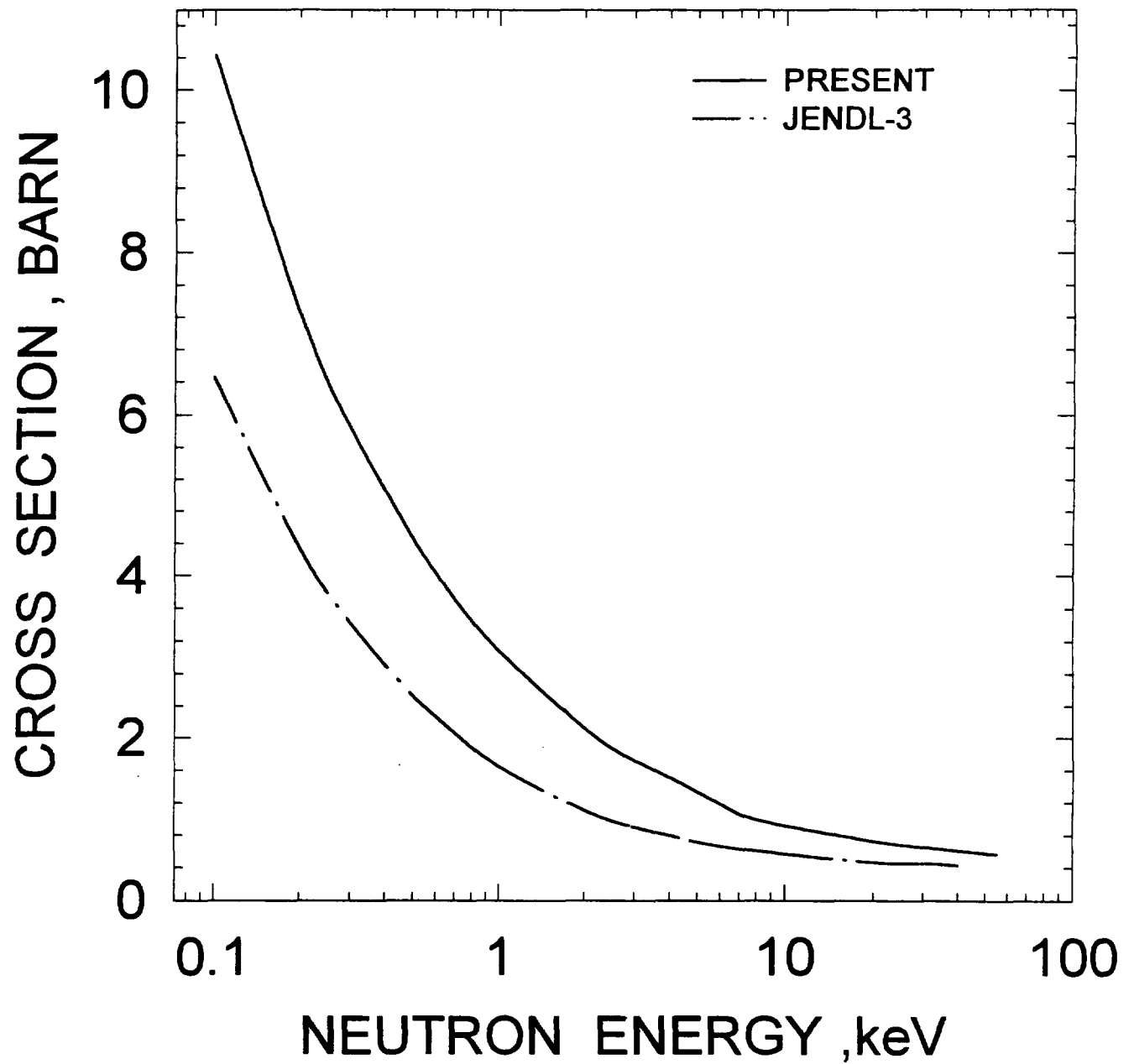


FIG.3.5

^{245}Cm REACTION CROSS SECTION

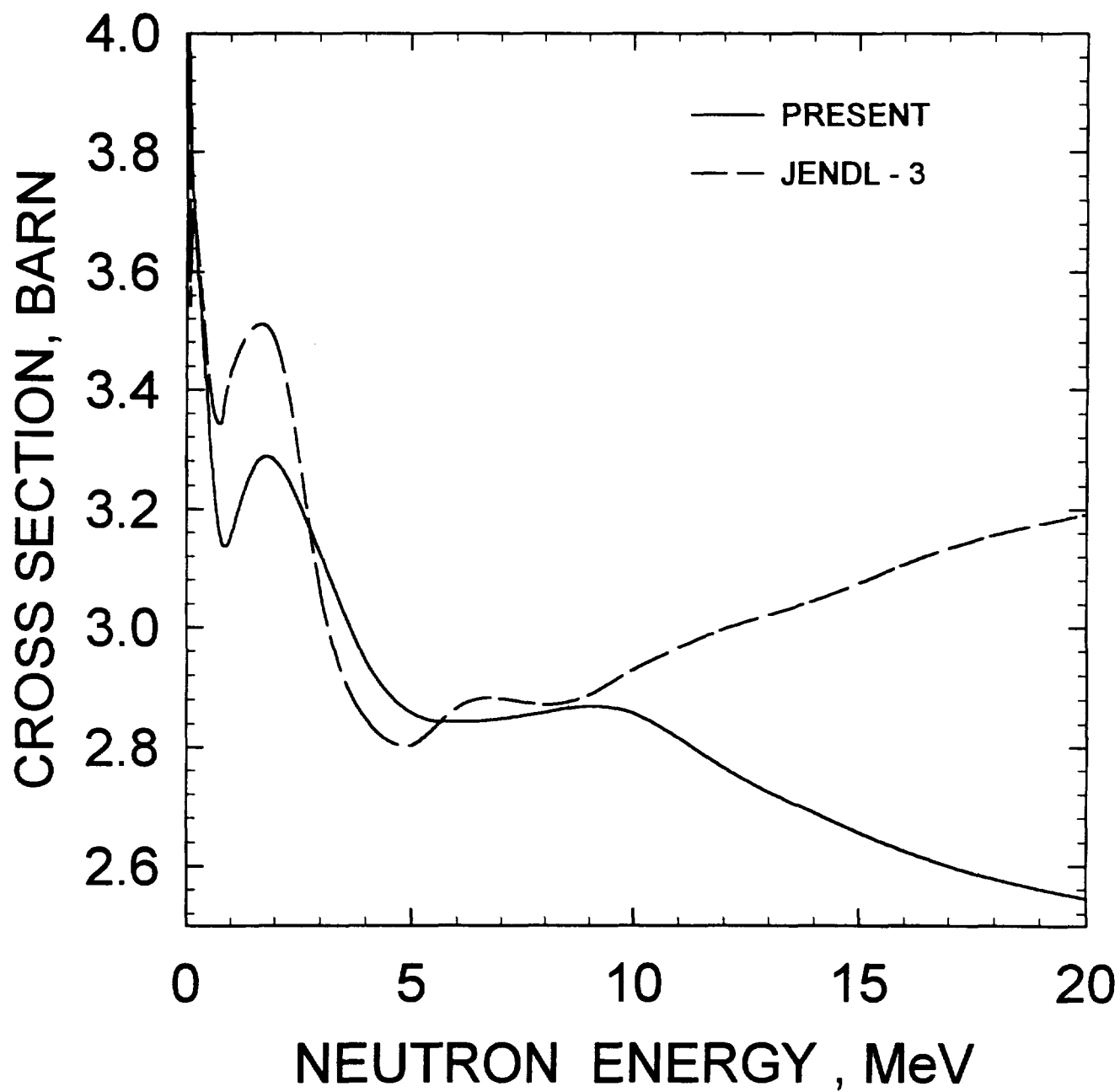


FIG.4.1

^{245}Cm TOTAL CROSS SECTION

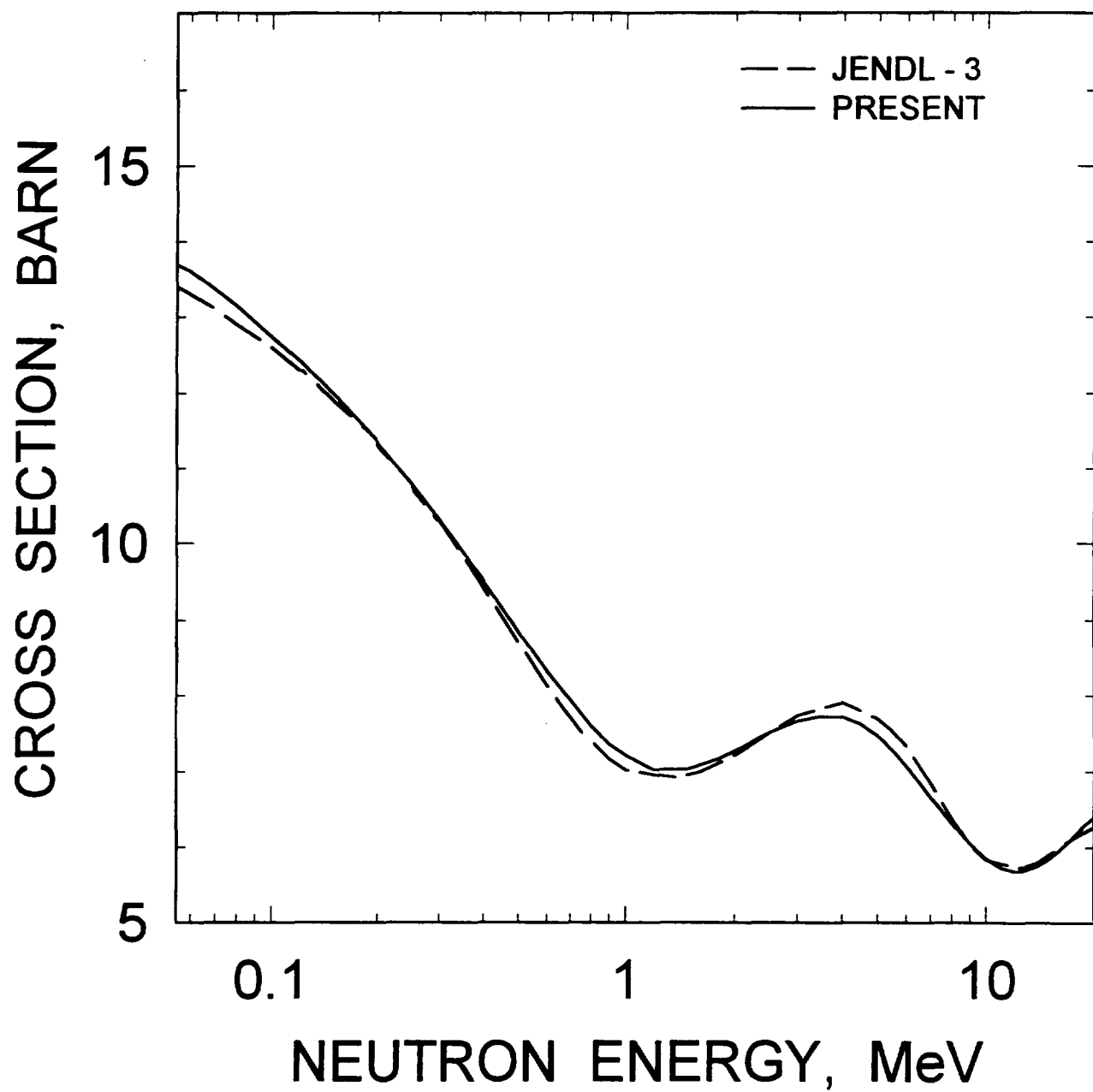


FIG. 4.2

^{245}Cm ELASTIC SCATTERING
CROSS SECTION

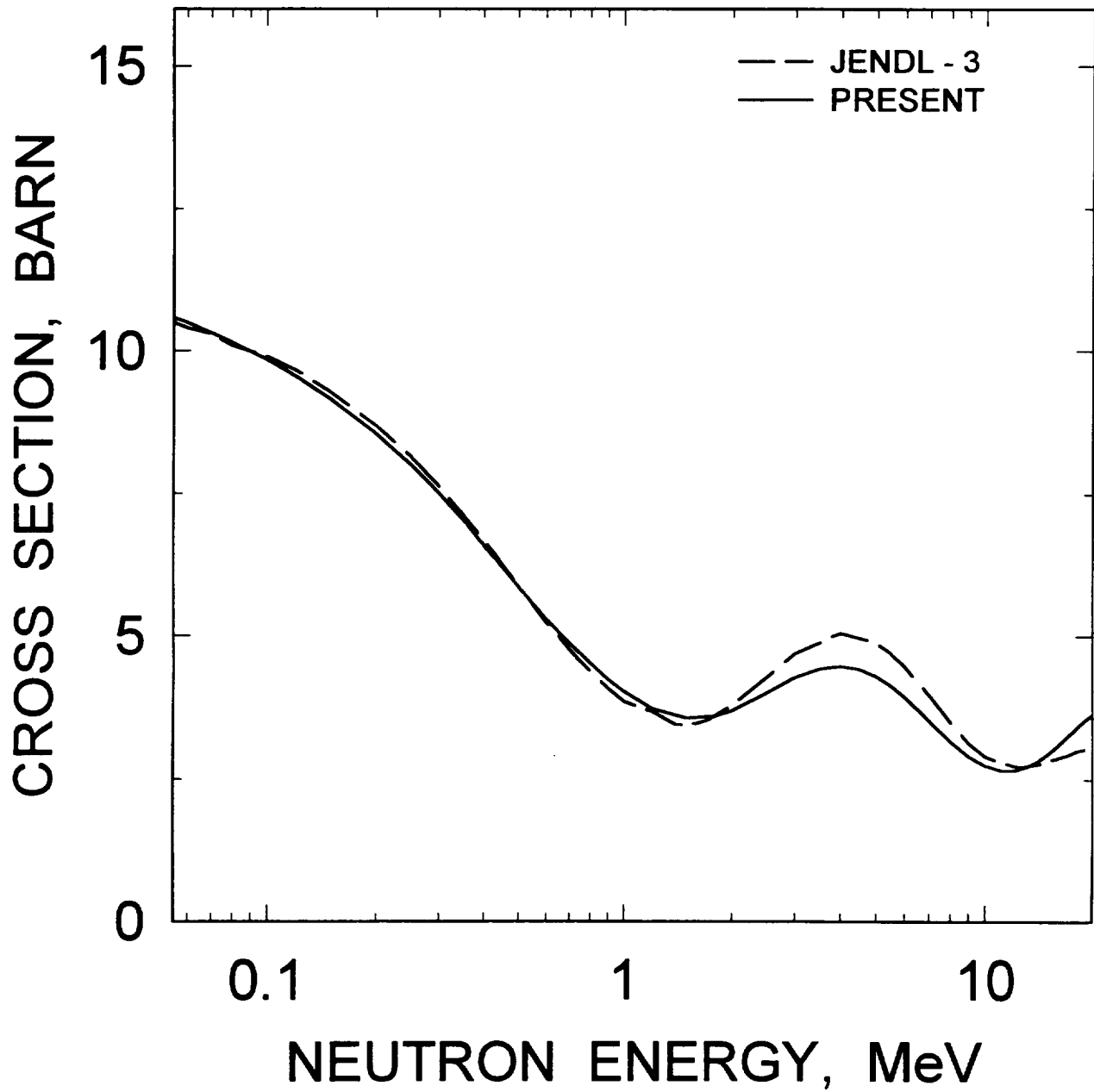


FIG. 4.3

^{245}Cm FISSION CROSS SECTION

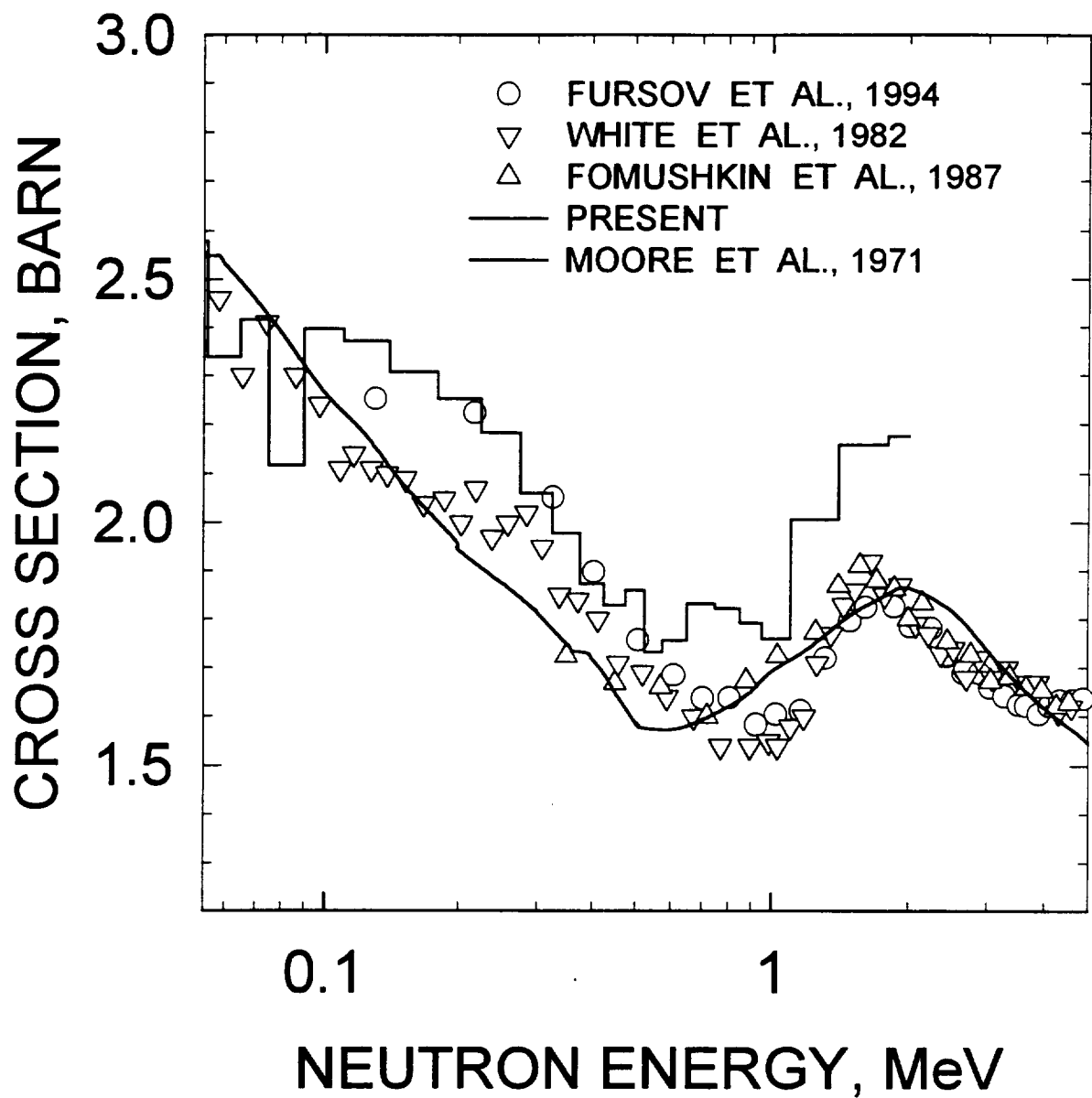


FIG 4.4

^{245}Cm FISSION CROSS SECTION

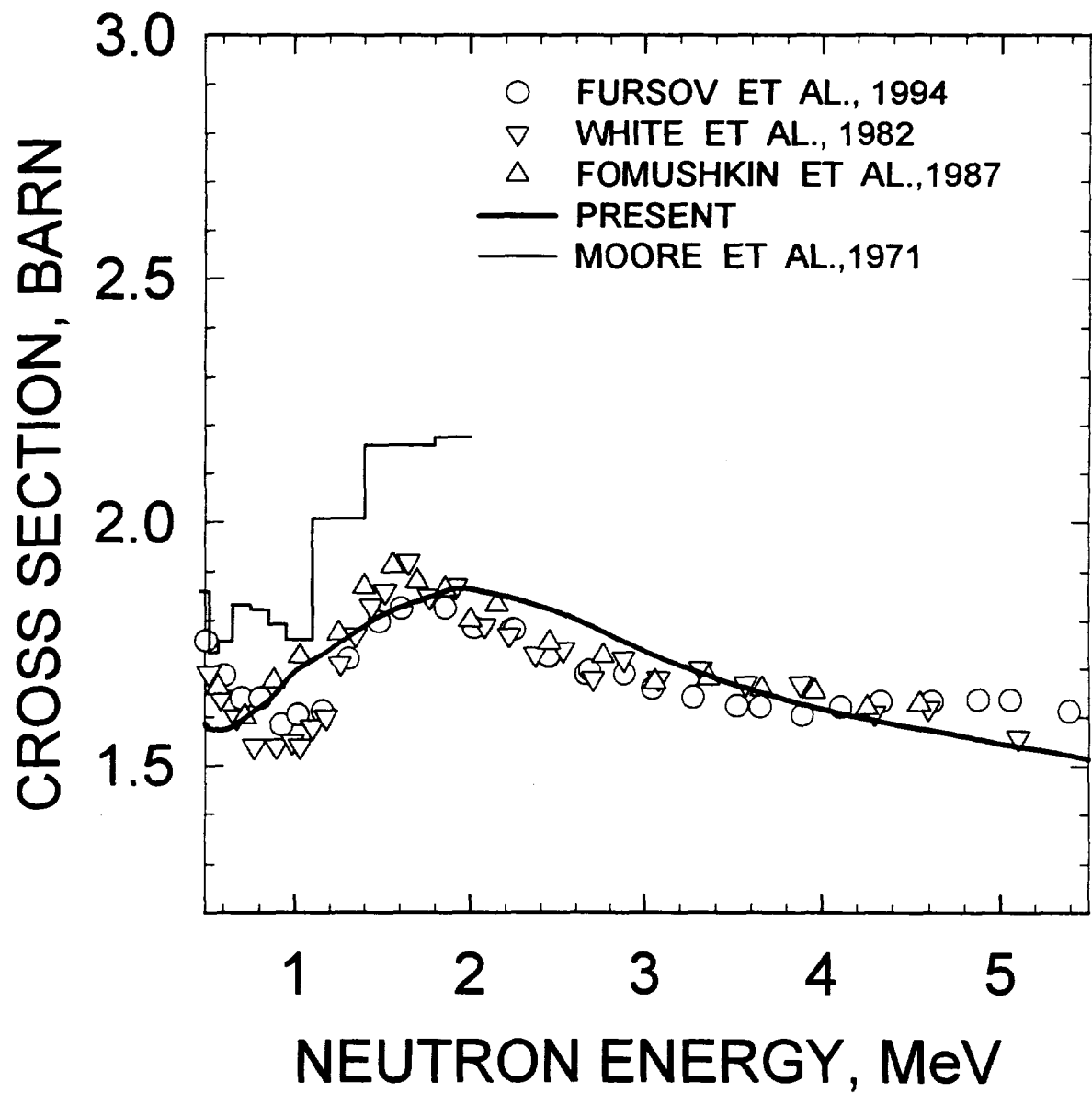


FIG 4.5

^{245}Cm FISSION CROSS SECTION

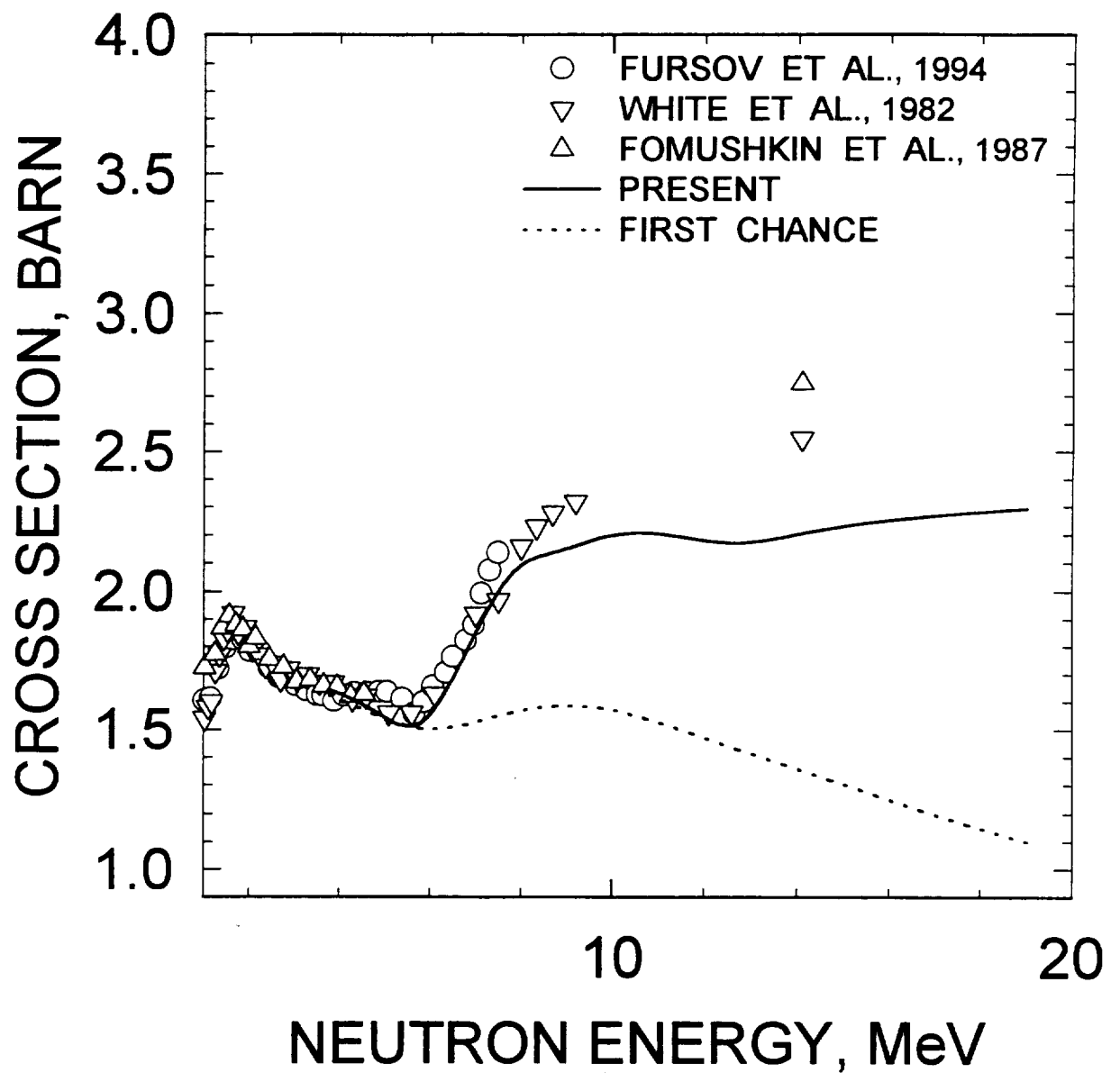


FIG 4.6

^{244}Cm FISSION CROSS SECTION

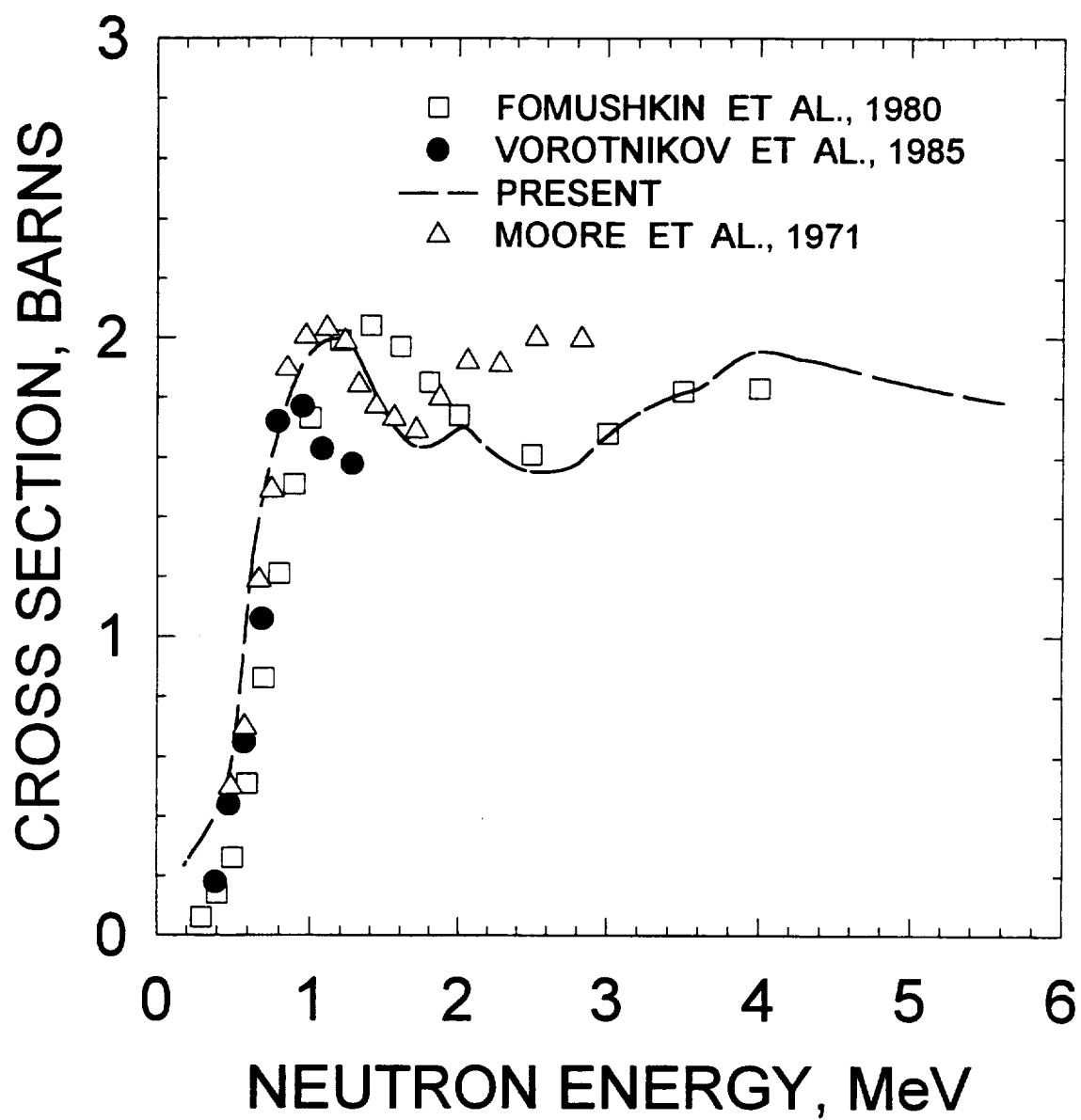


FIG 4.7

^{245}Cm FISSION CROSS SECTION

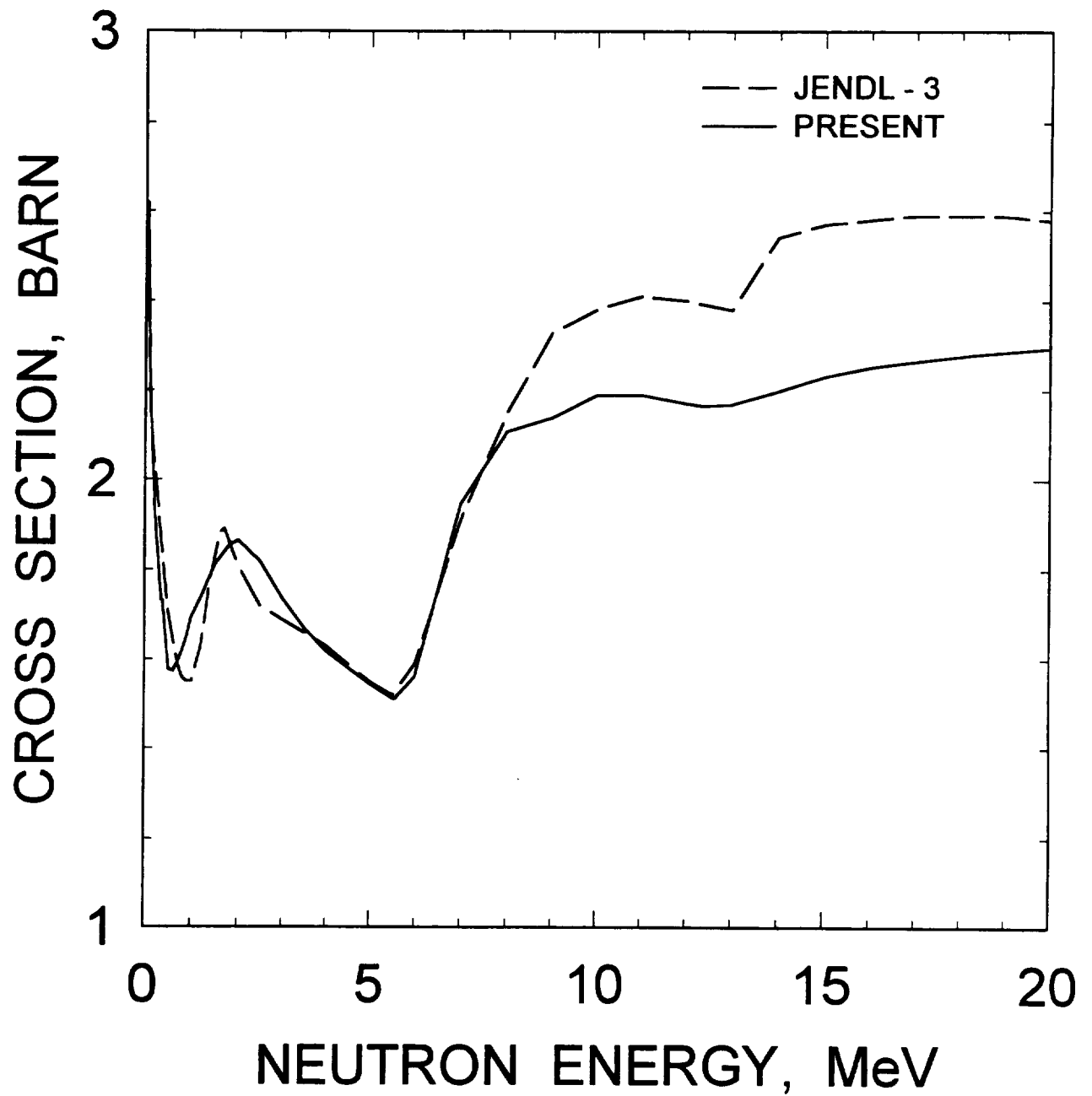


FIG. 4.8

^{245}Cm

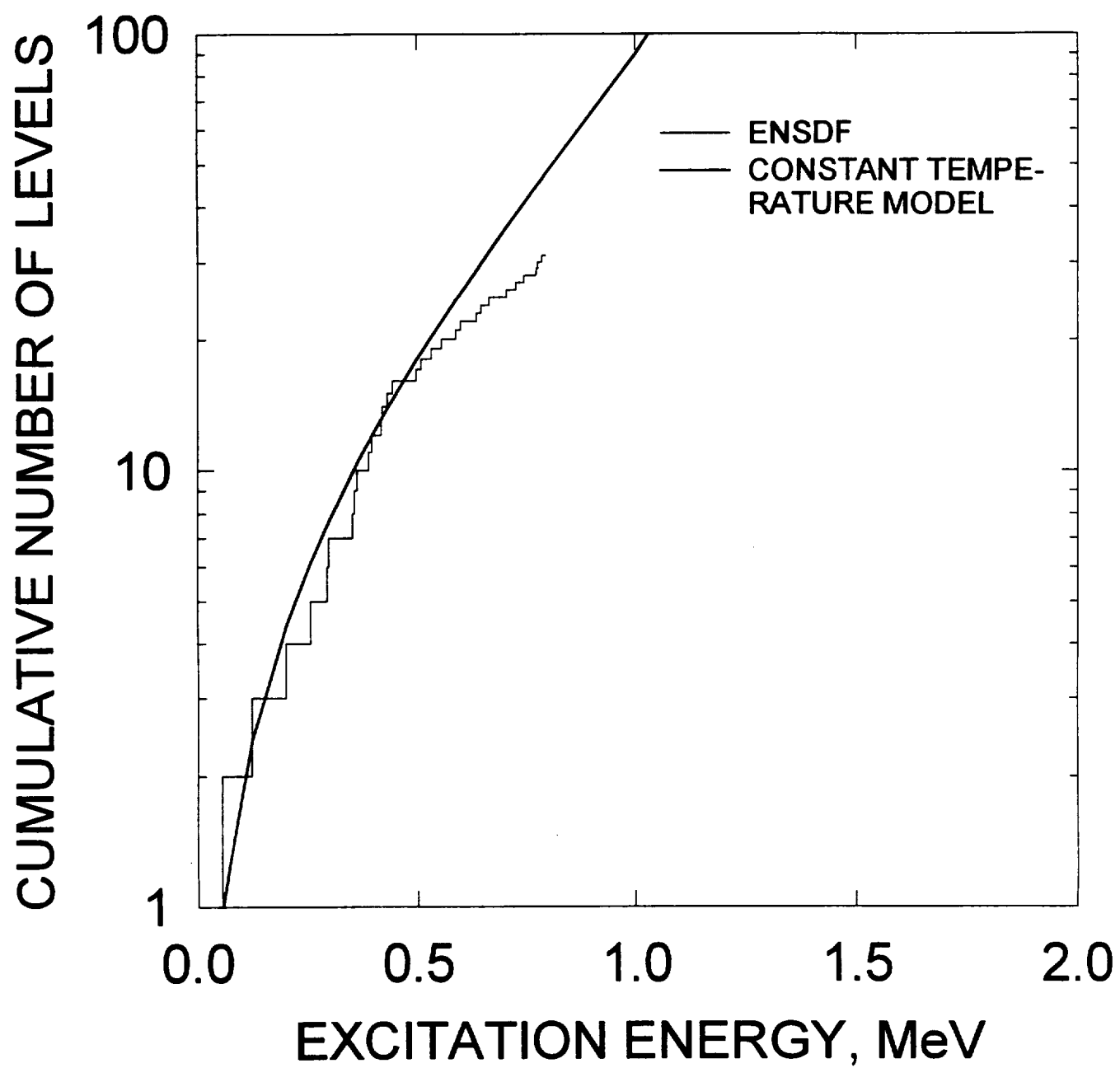


FIG. 4.9

$n + {}^{244}\text{Cm}$

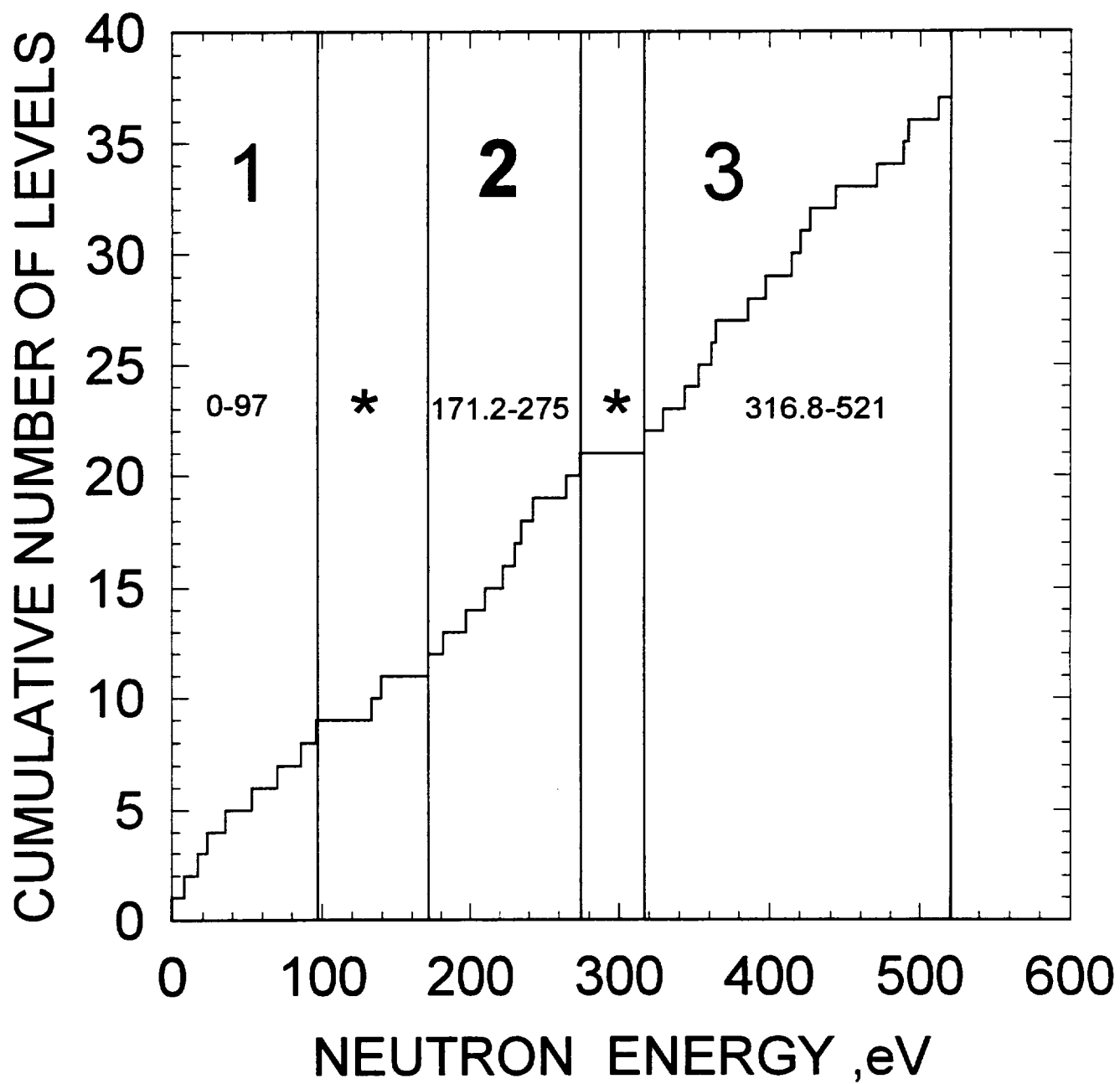


FIG.4.10

^{245}Cm INELASTIC CROSS SECTION

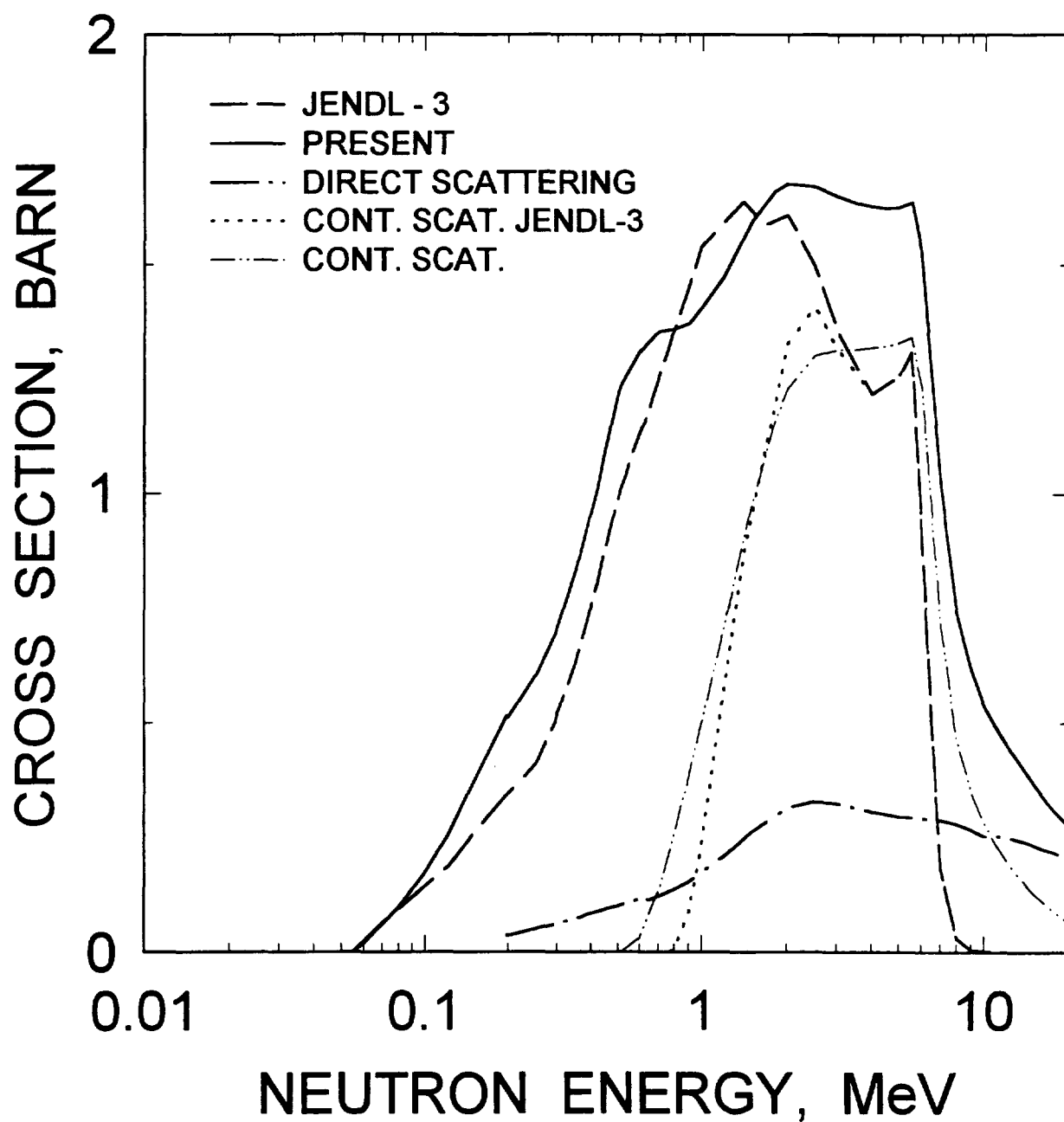


FIG. 4.11

^{245}Cm : 0.0548 MeV, $9/2^+$ LEVEL EXCITATION

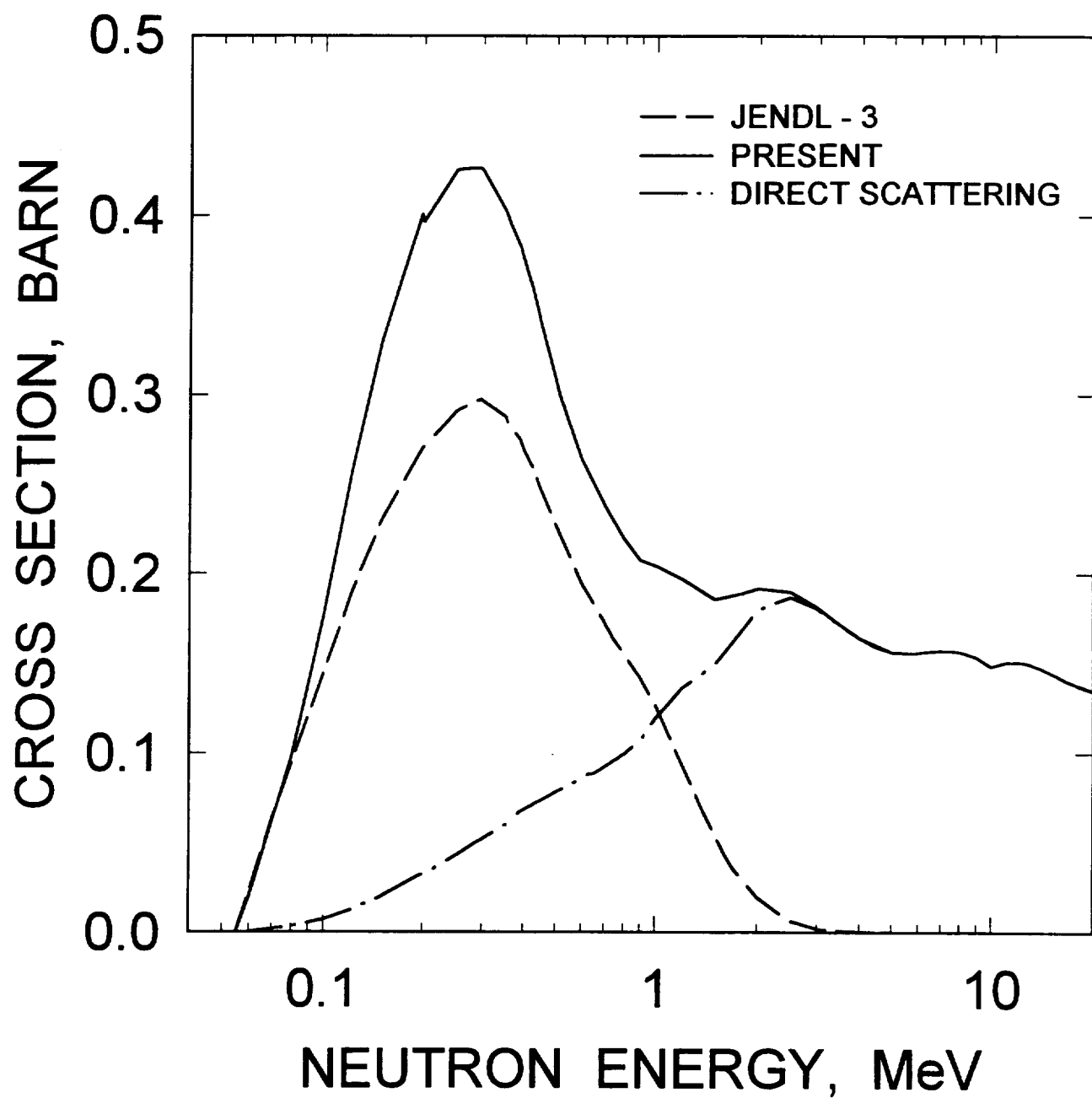


FIG. 4.12

^{245}Cm : 0.1215 MeV, $11/2^+$ LEVEL EXCITATION

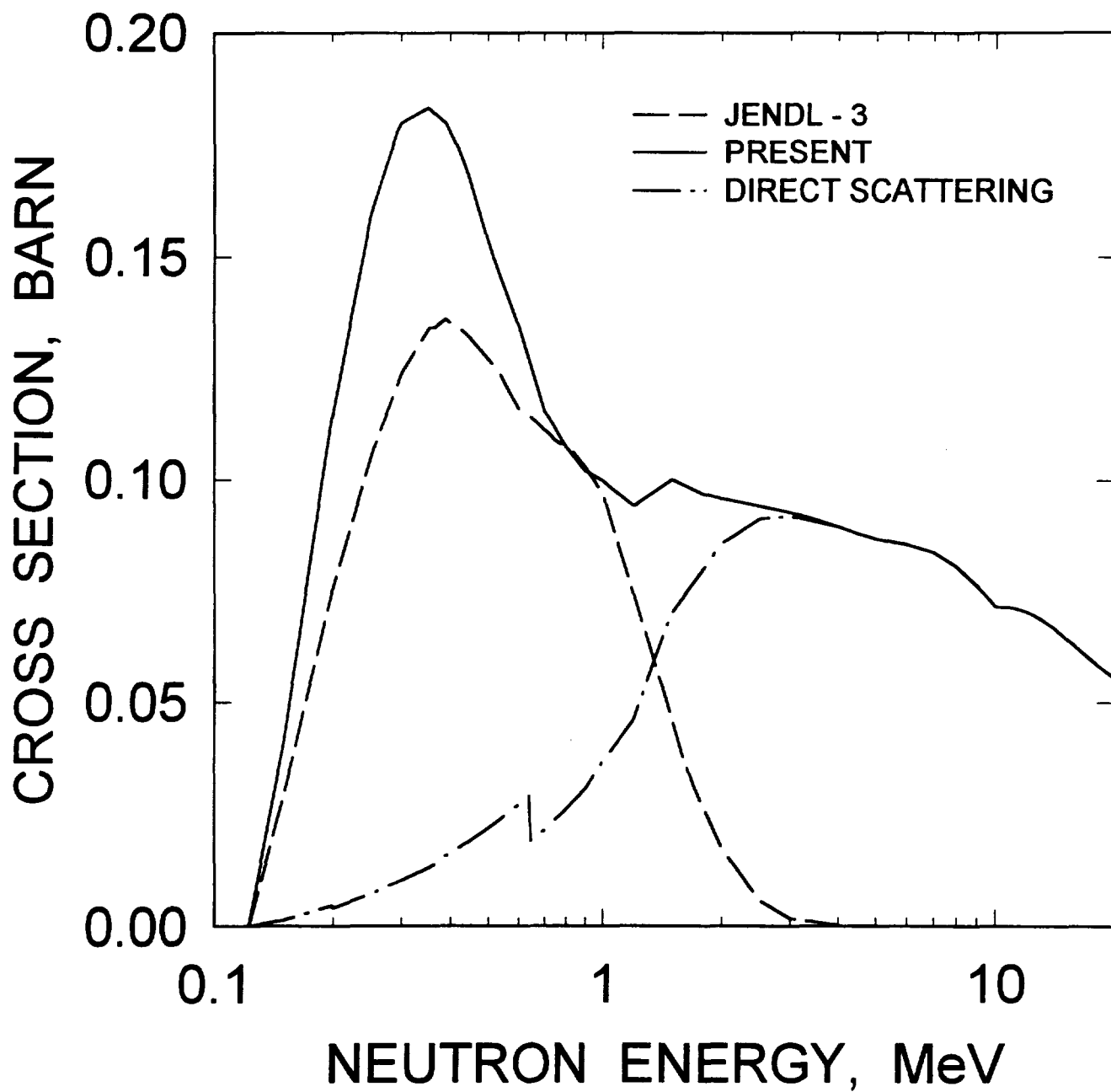


FIG. 4.13

^{245}Cm : 0.1974 MeV, $13/2^+$ LEVEL EXCITATION

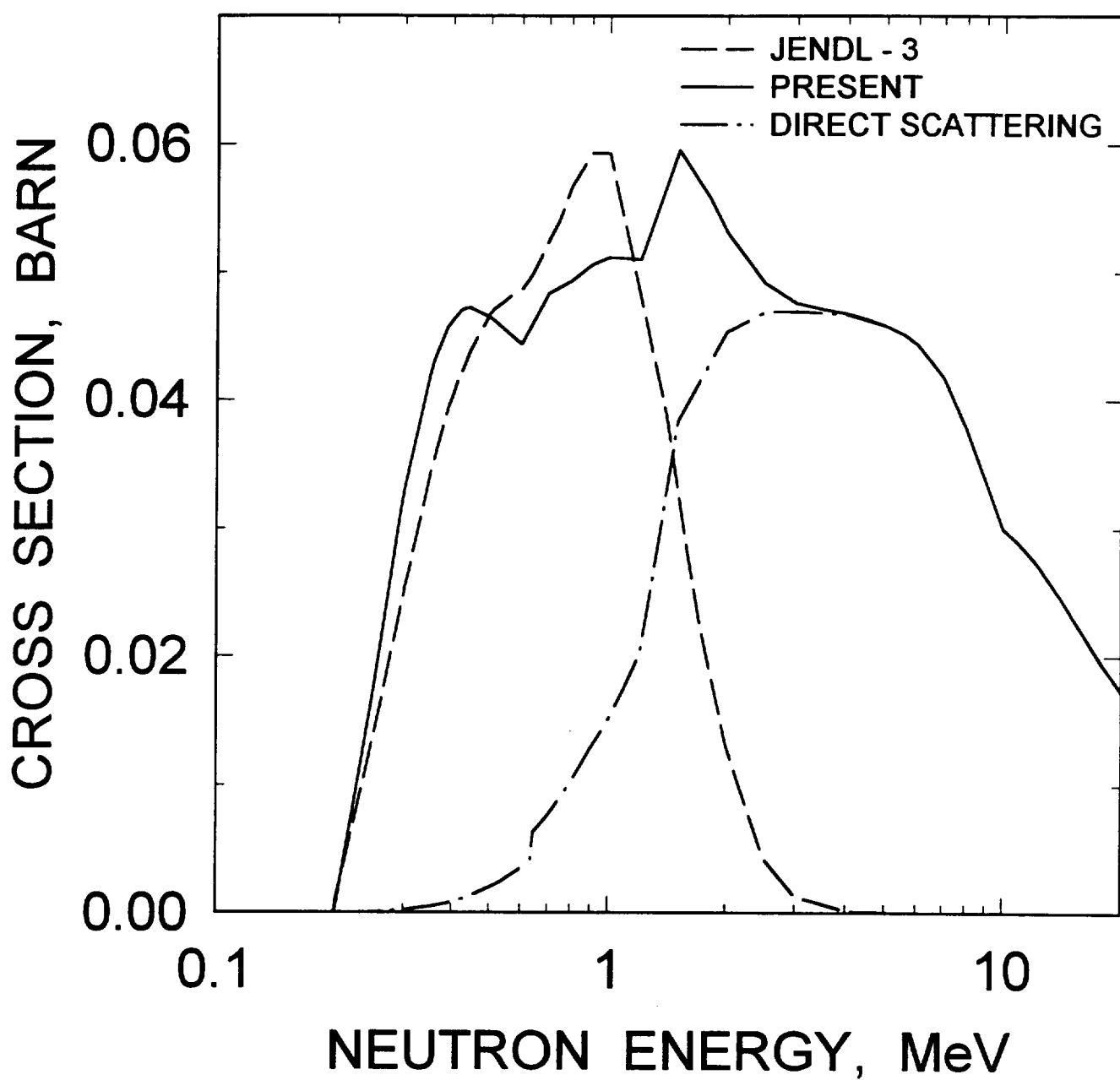


FIG. 4.14

^{245}Cm : 0.2993, $15/2^+$ LEVEL EXCITATION

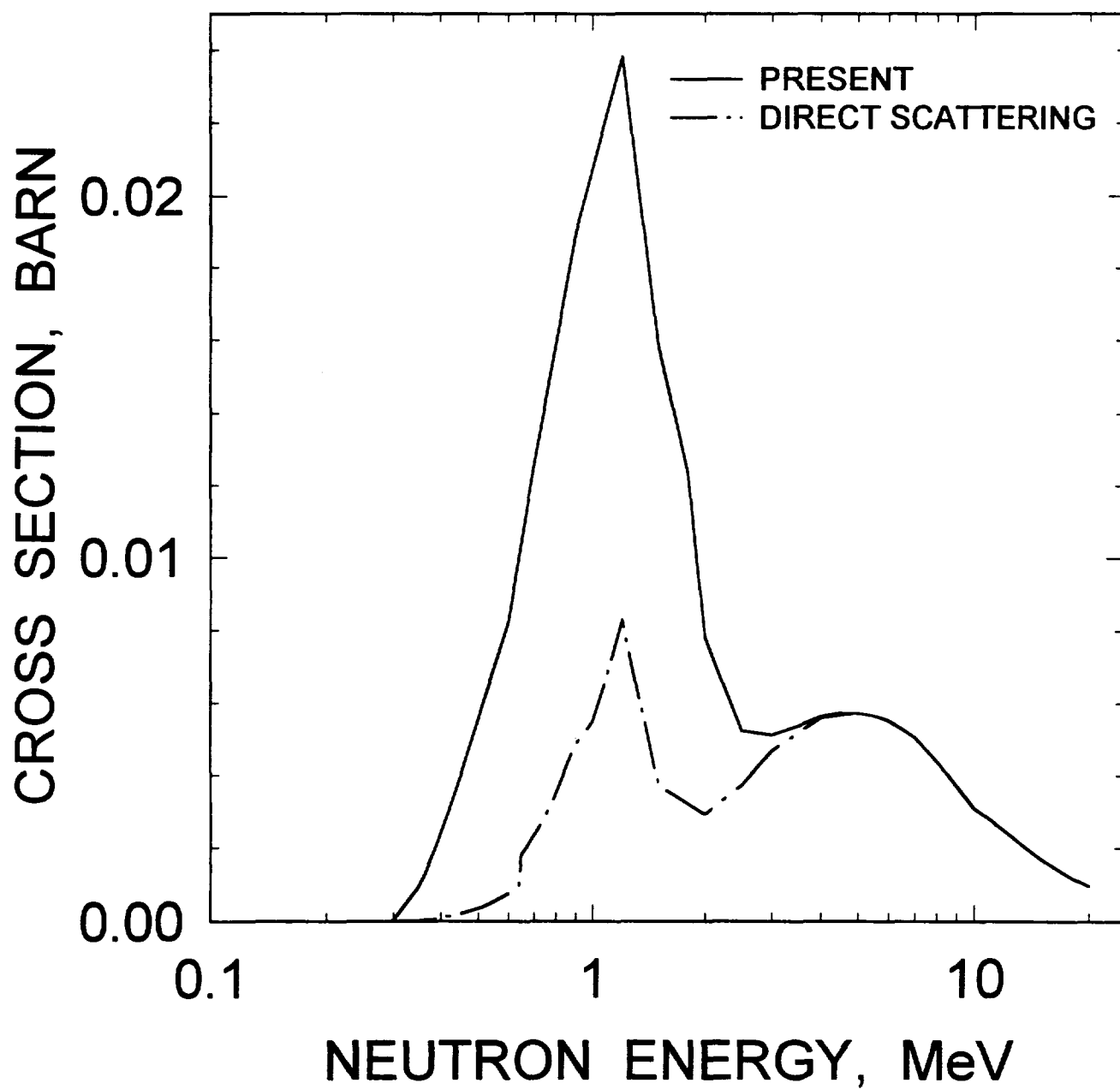


FIG.4.15

^{245}Cm : 0.3957, $17/2^+$ LEVEL EXCITATION

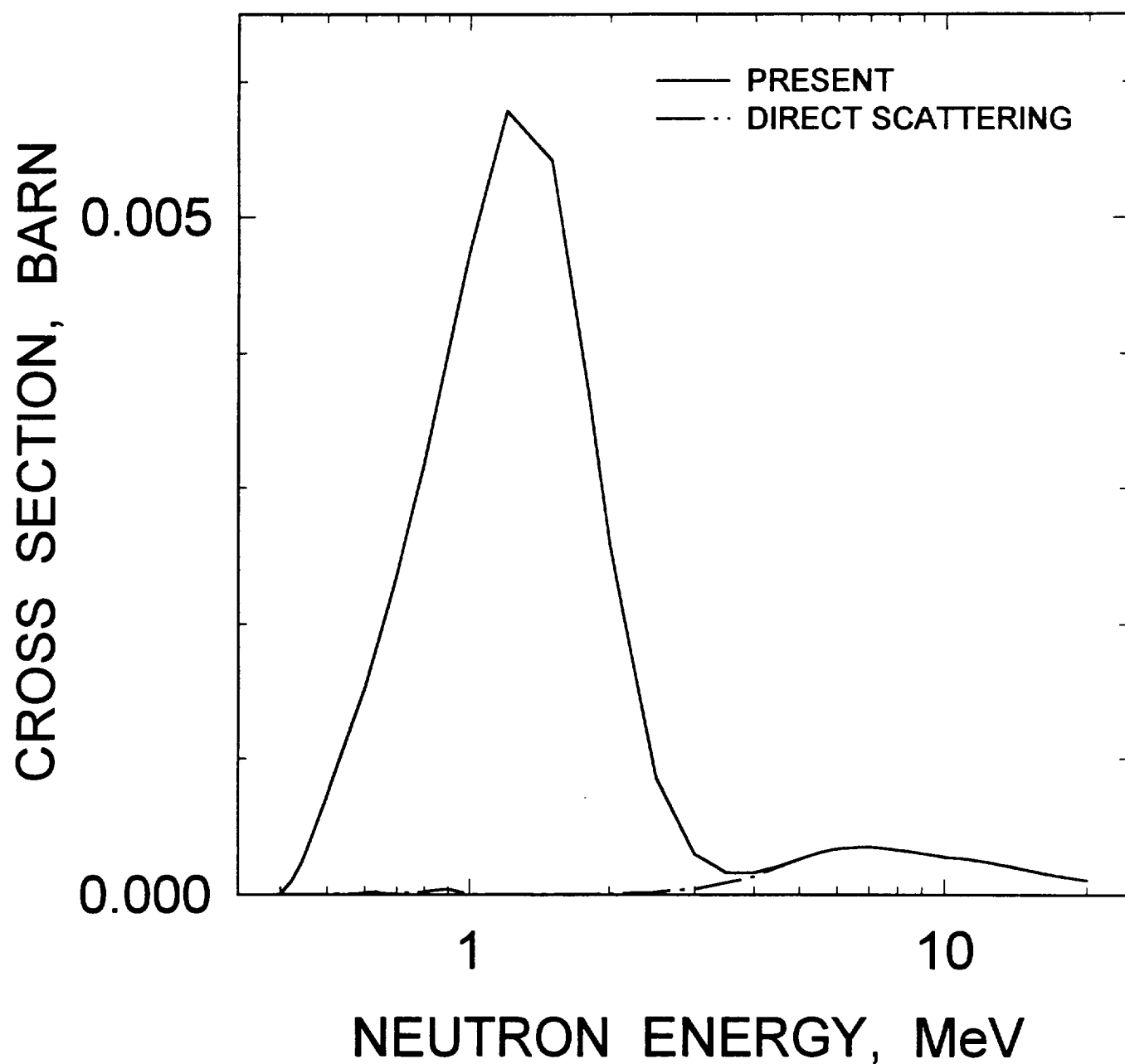


FIG. 4.16

^{245}Cm RADIATIVE CAPTURE CROSS SECTION

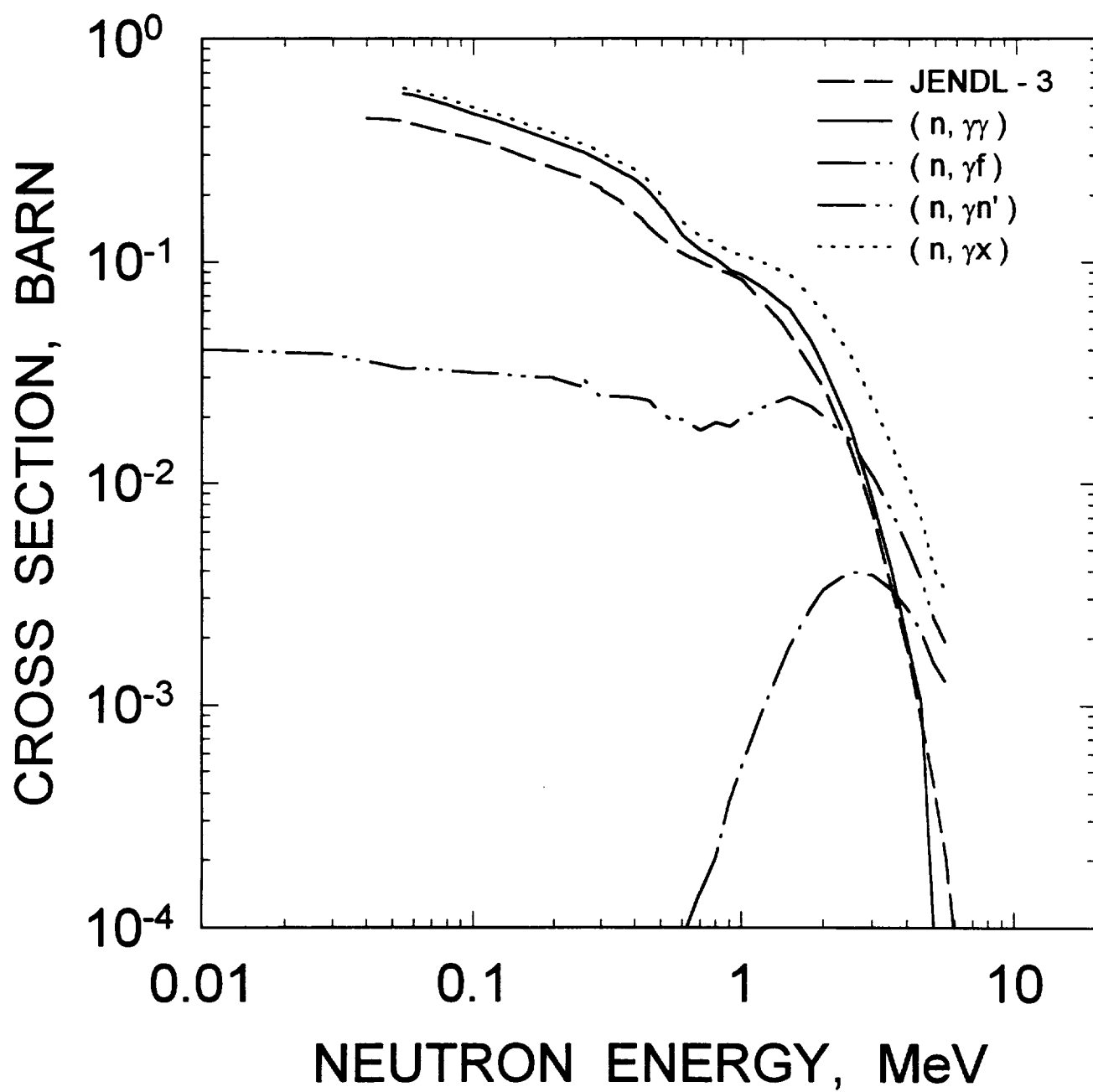


FIG. 4.17

^{245}Cm (n,2n) CROSS SECTION

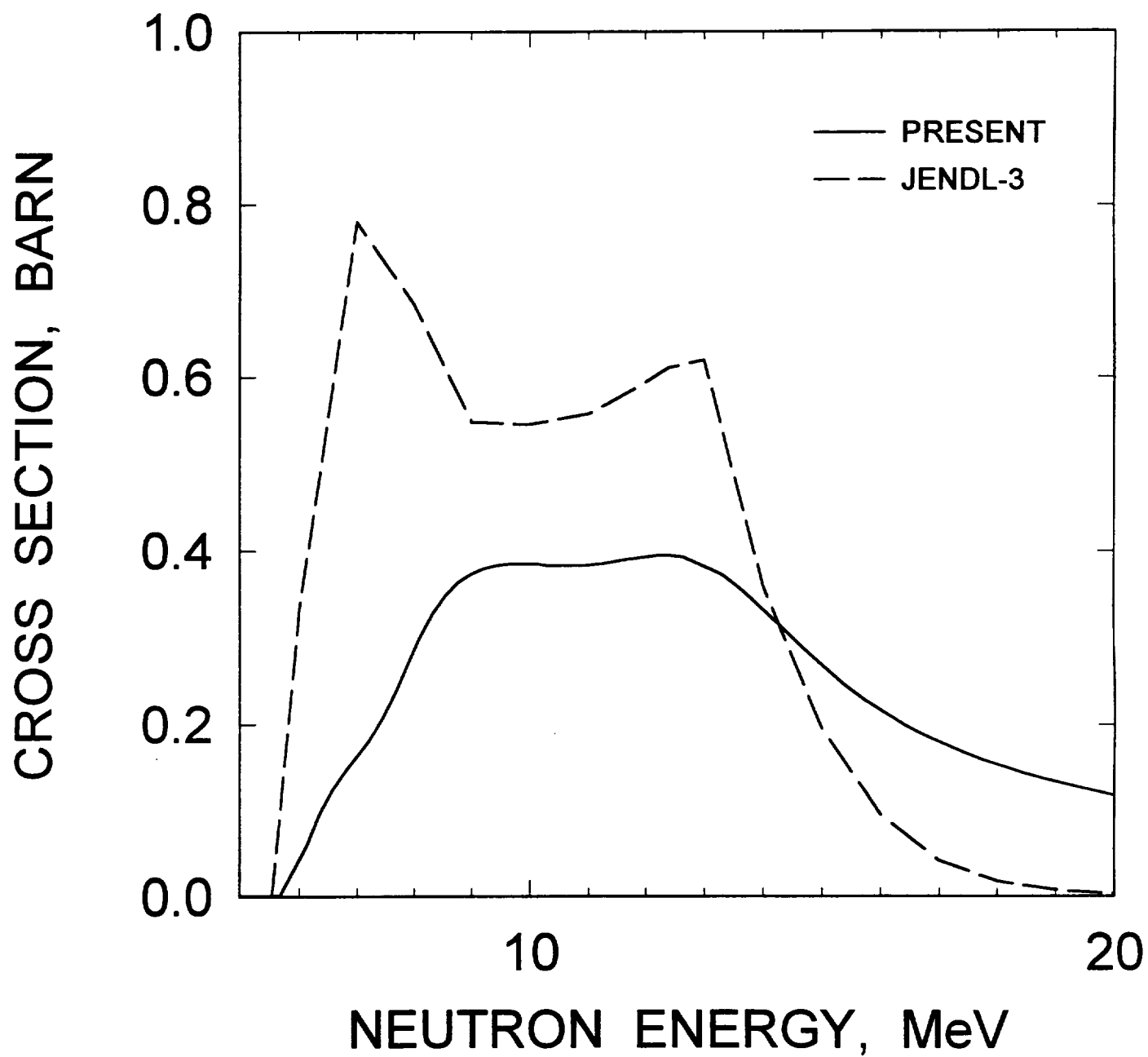


FIG. 4.18

^{245}Cm (n,3n) CROSS SECTION

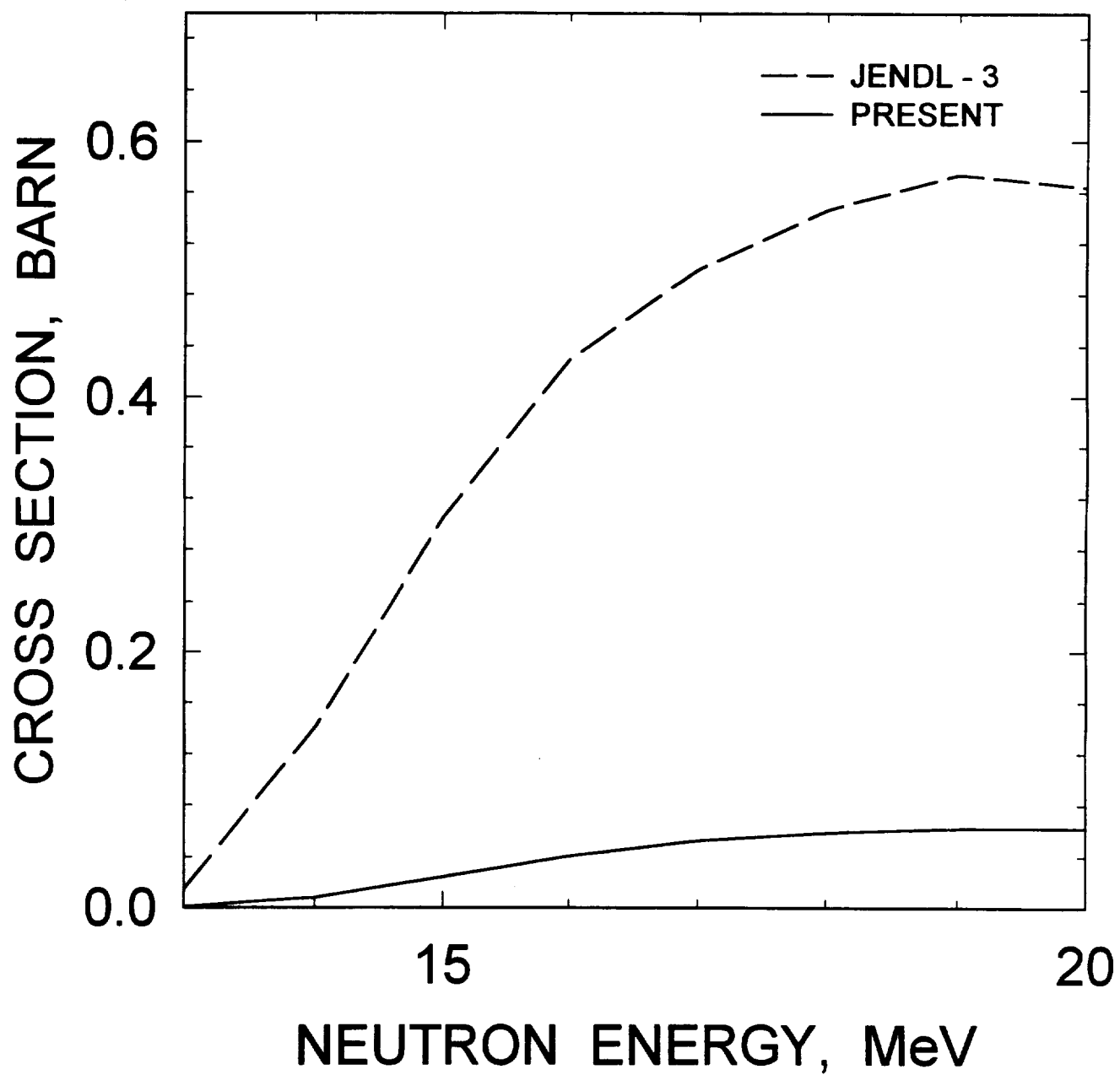


FIG. 4.19

^{245}Cm $E_n=14\text{ MeV}$
COMPONENTS OF FIRST NEUTRON
SPECTRUM

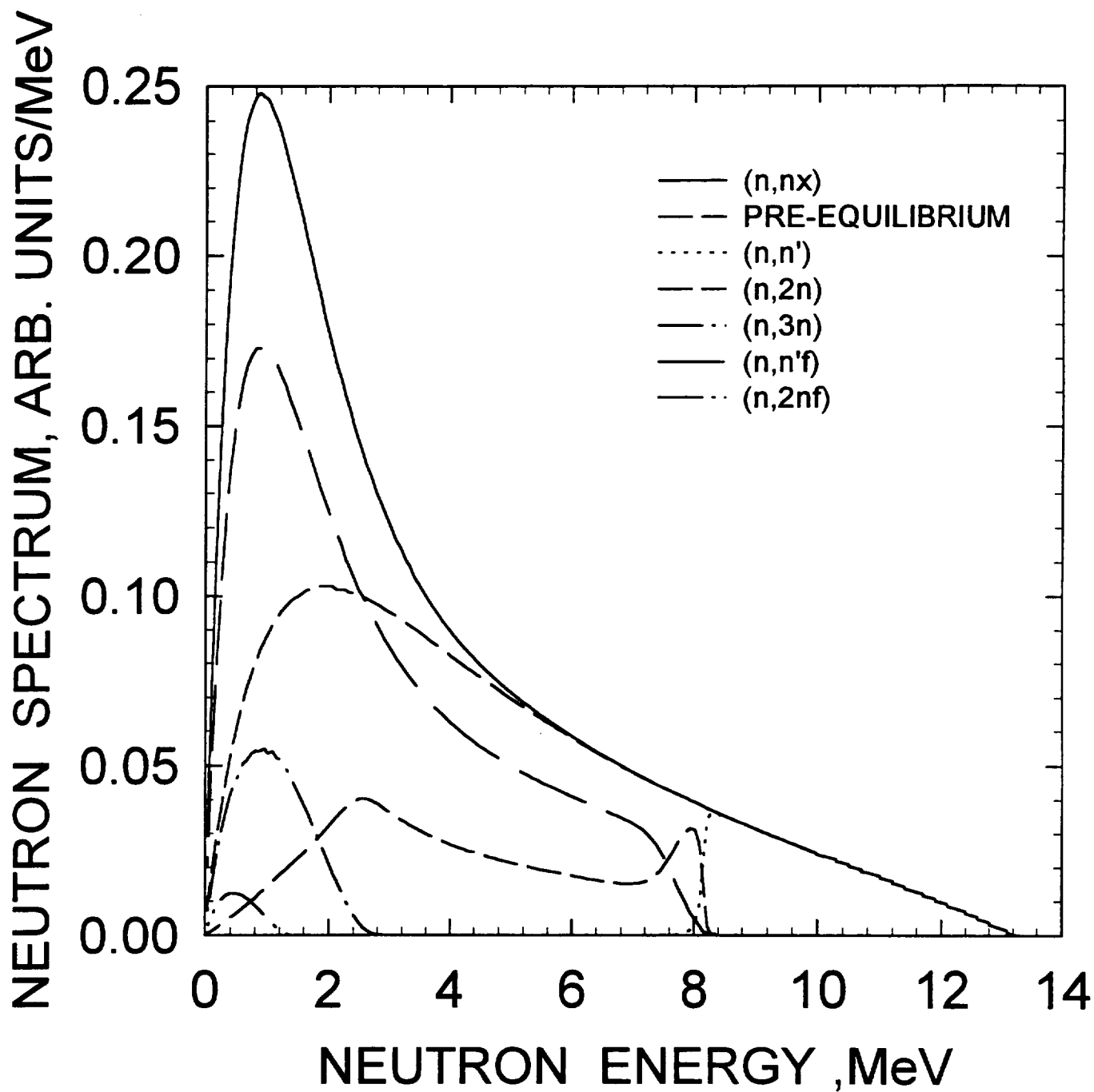


FIG.5.1

^{245}Cm $E_n=14\text{ MeV}$
COMPONENTS OF SECOND NEUTRON
SPECTRUM

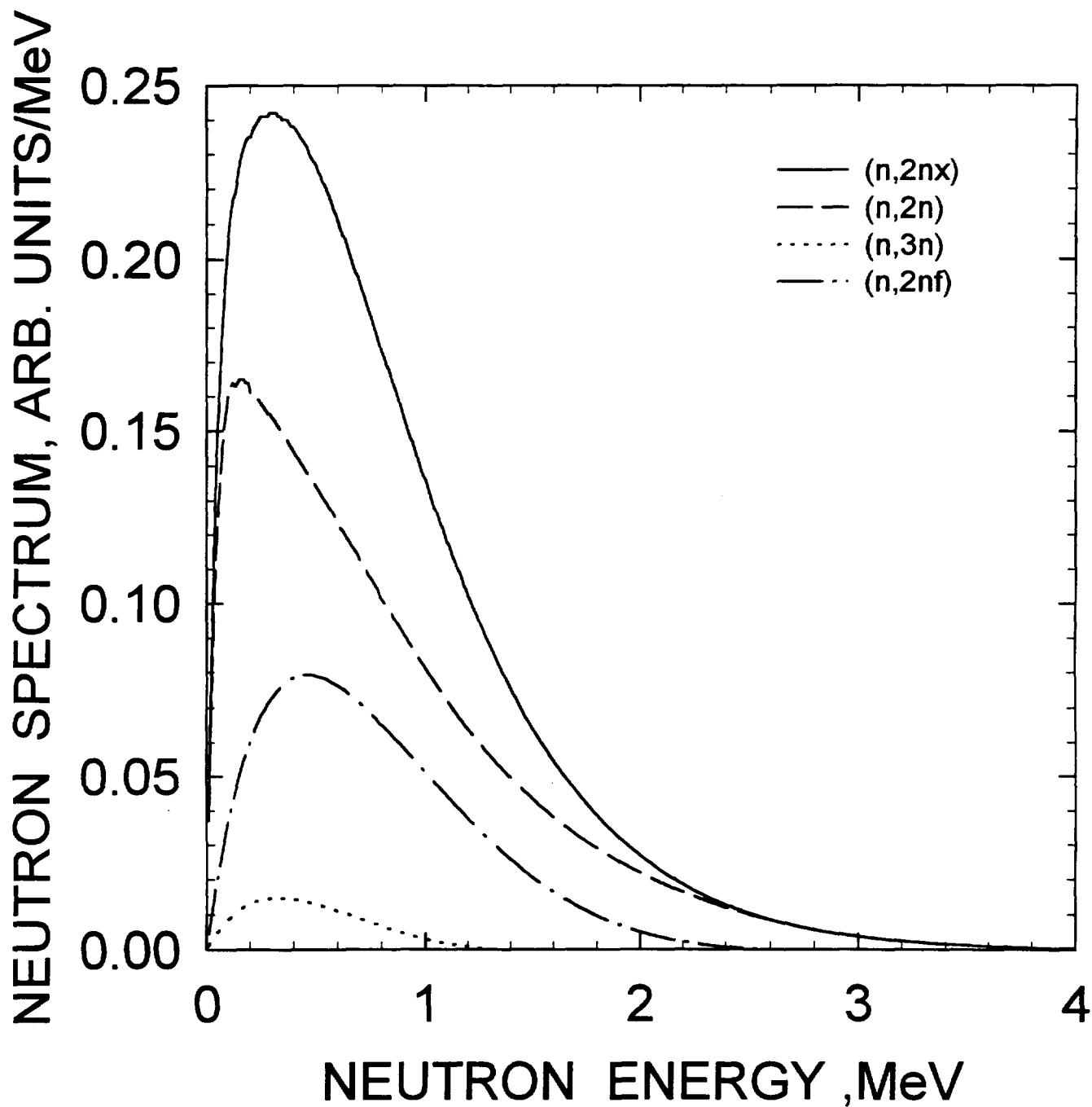


FIG.5.2

^{245}Cm $E_n=8\text{ MeV}$
COMPARISON WITH JENDL-3

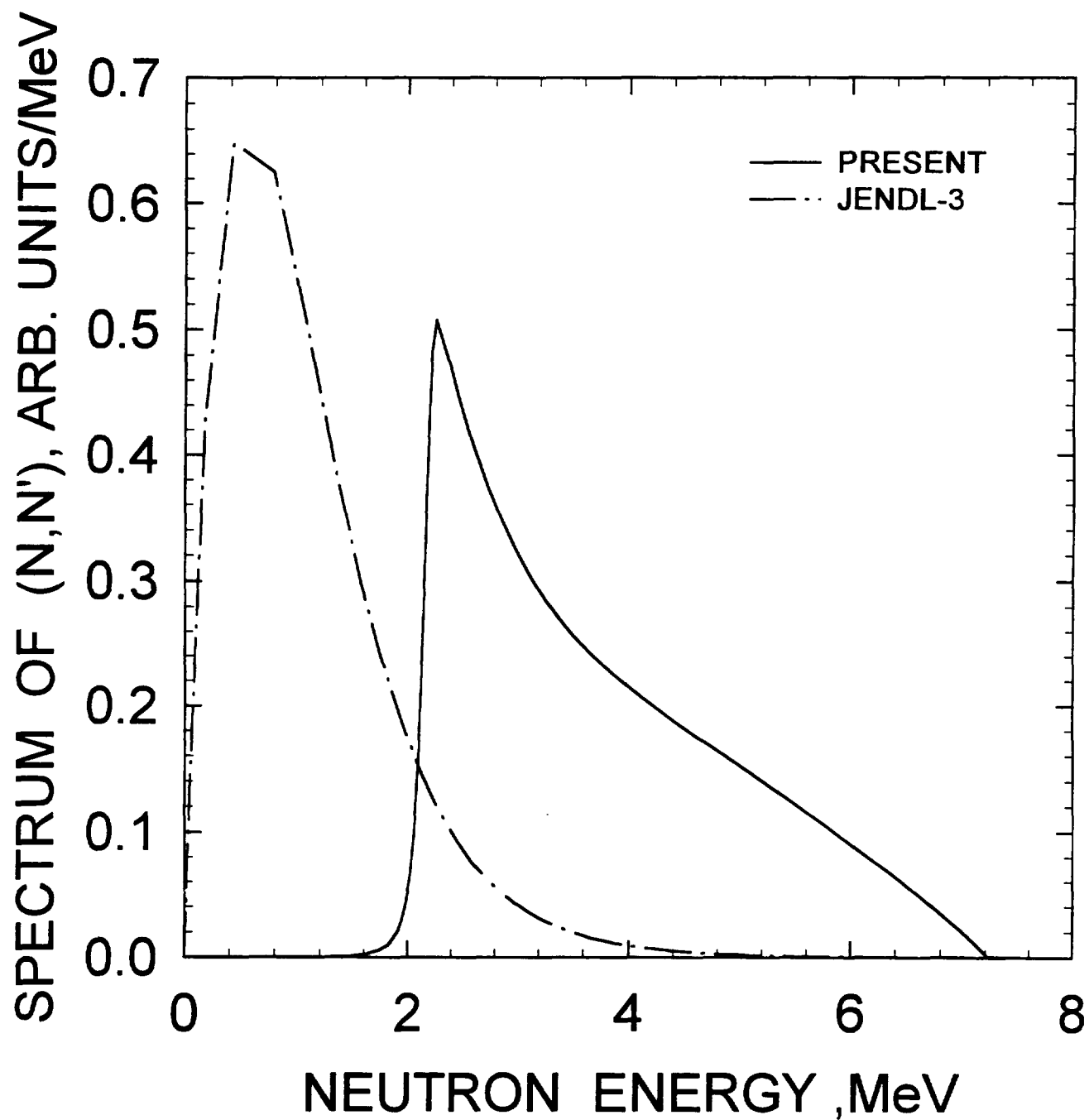


FIG.5.3

^{245}Cm $E_n=8$ MeV
COMPARISON WITH JENDL-3

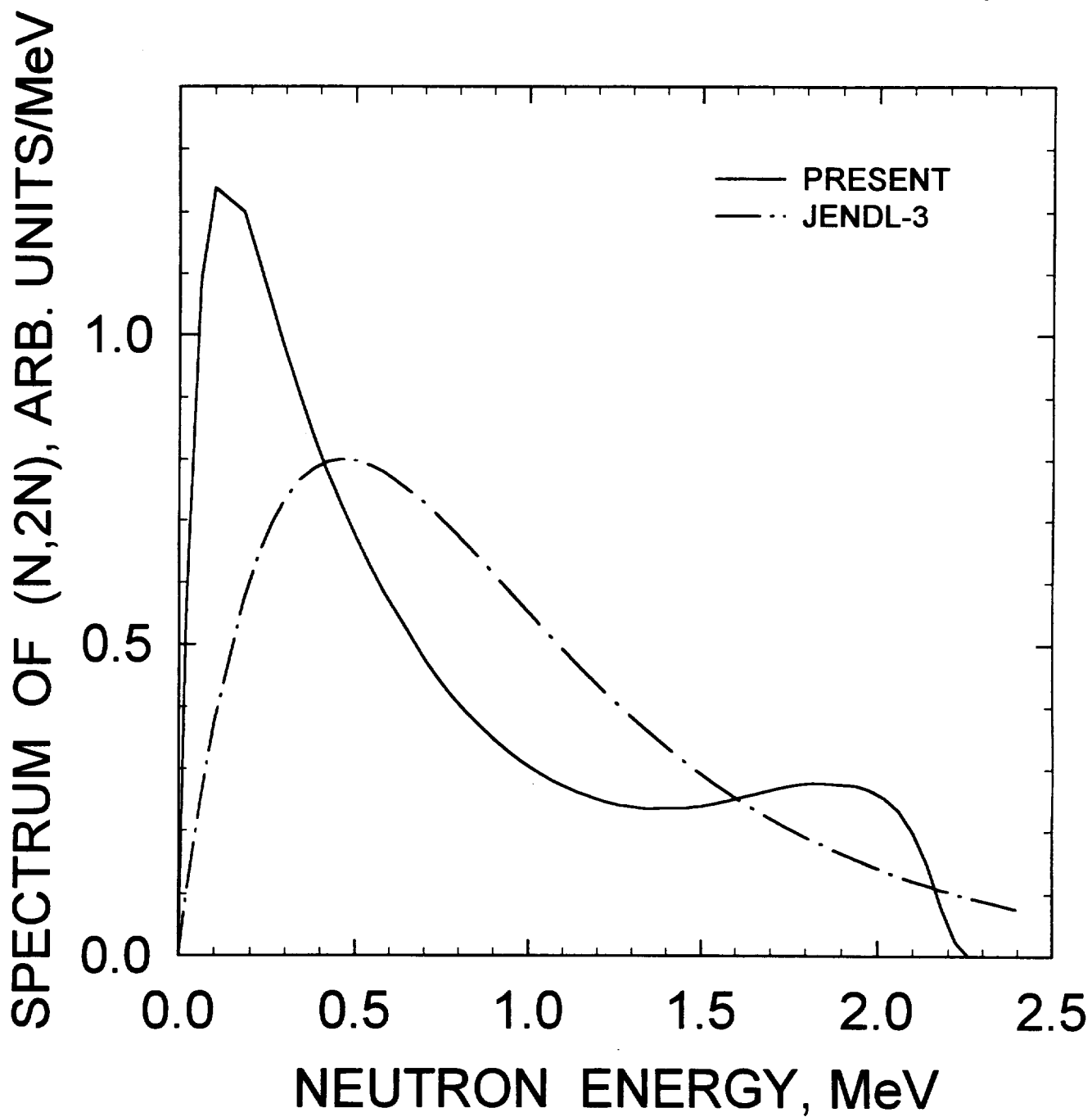


FIG.5.4

^{245}Cm $E_n=14$ MeV
COMPARISON WITH JENDL-3

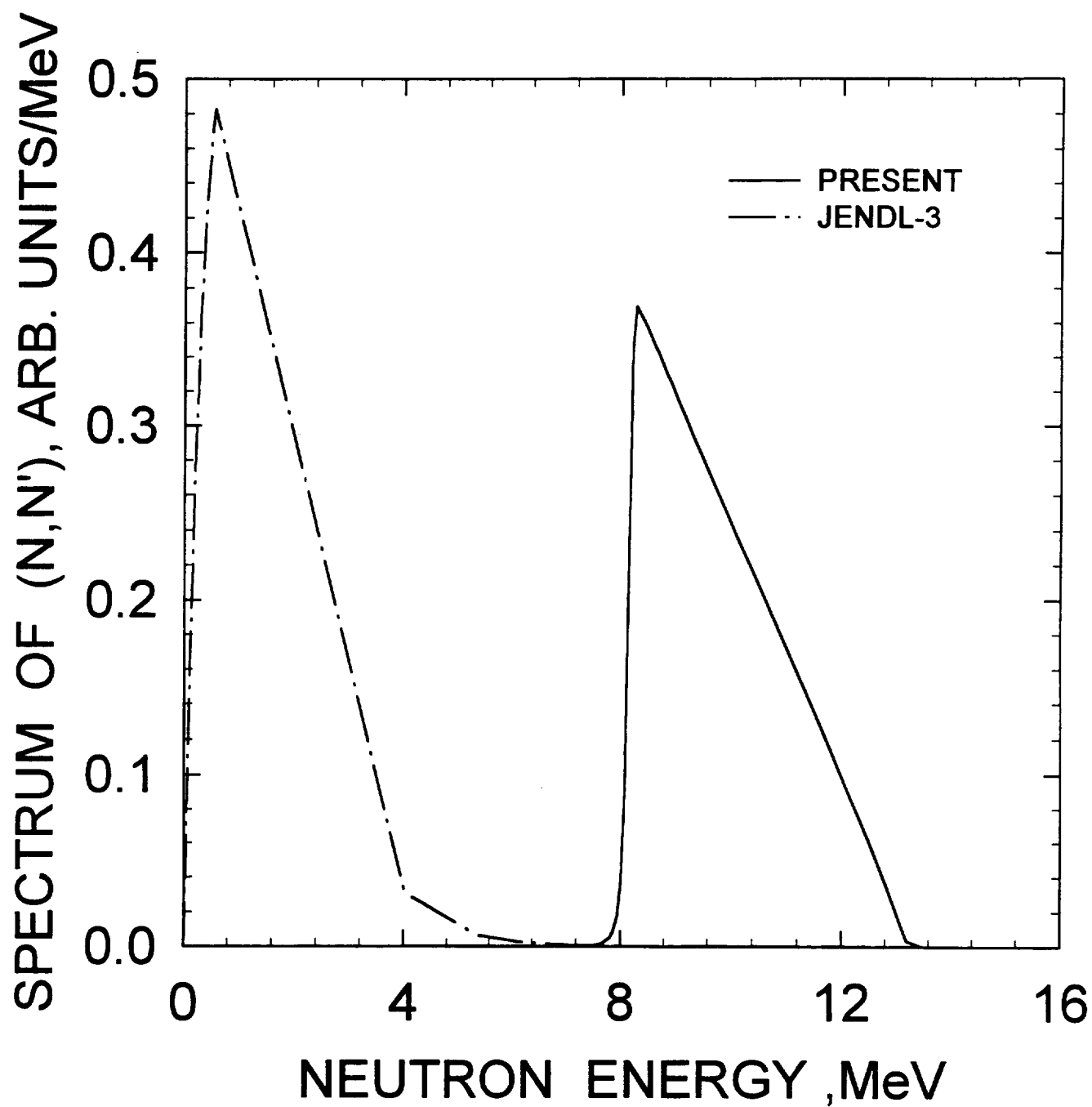


FIG.5.5

^{245}Cm $E_n = 14 \text{ MeV}$
COMPARISON WITH JENDL-3

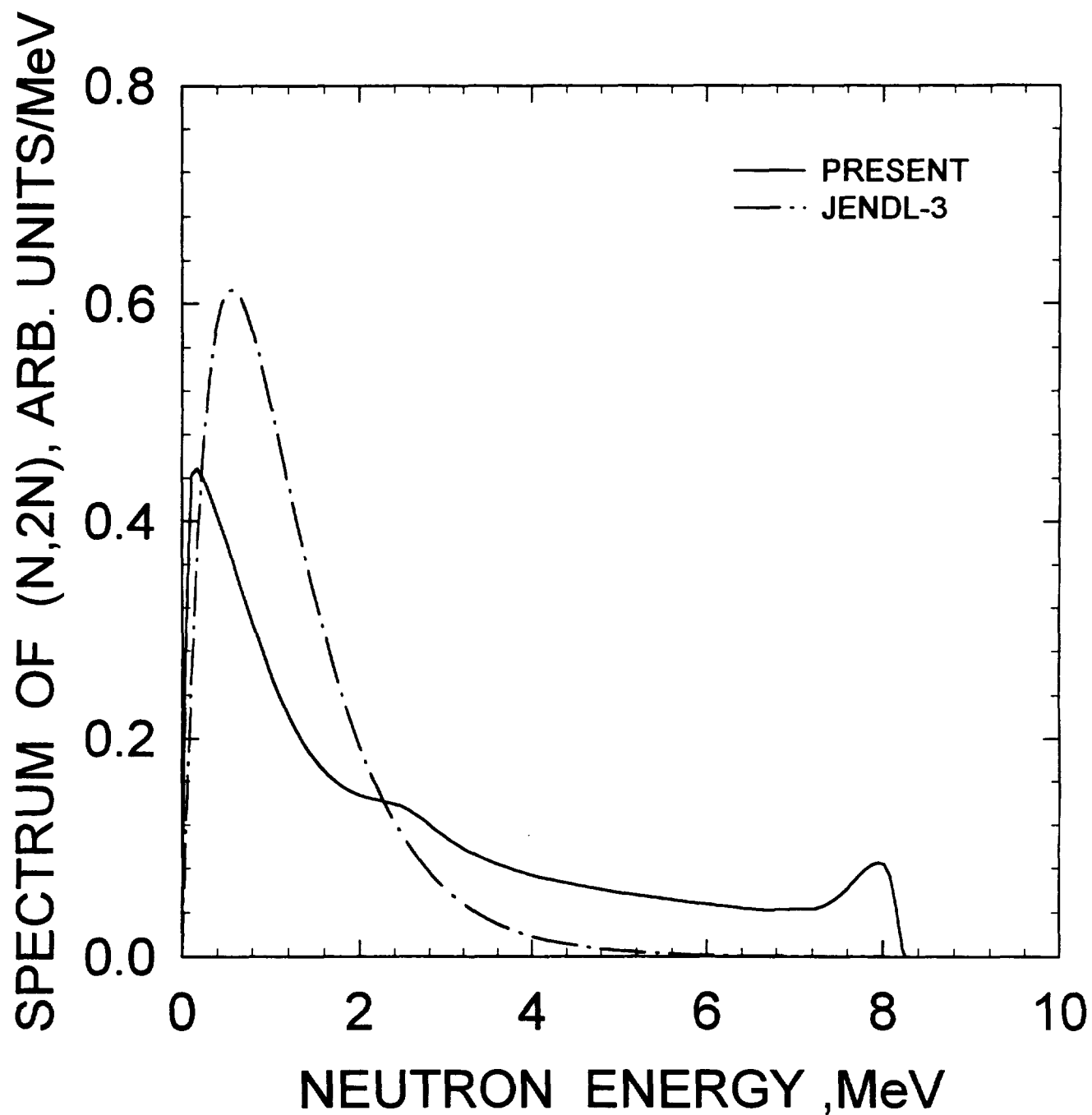


FIG.5.6

^{245}Cm $E_n=14$ MeV
COMPARISON WITH JENDL-3

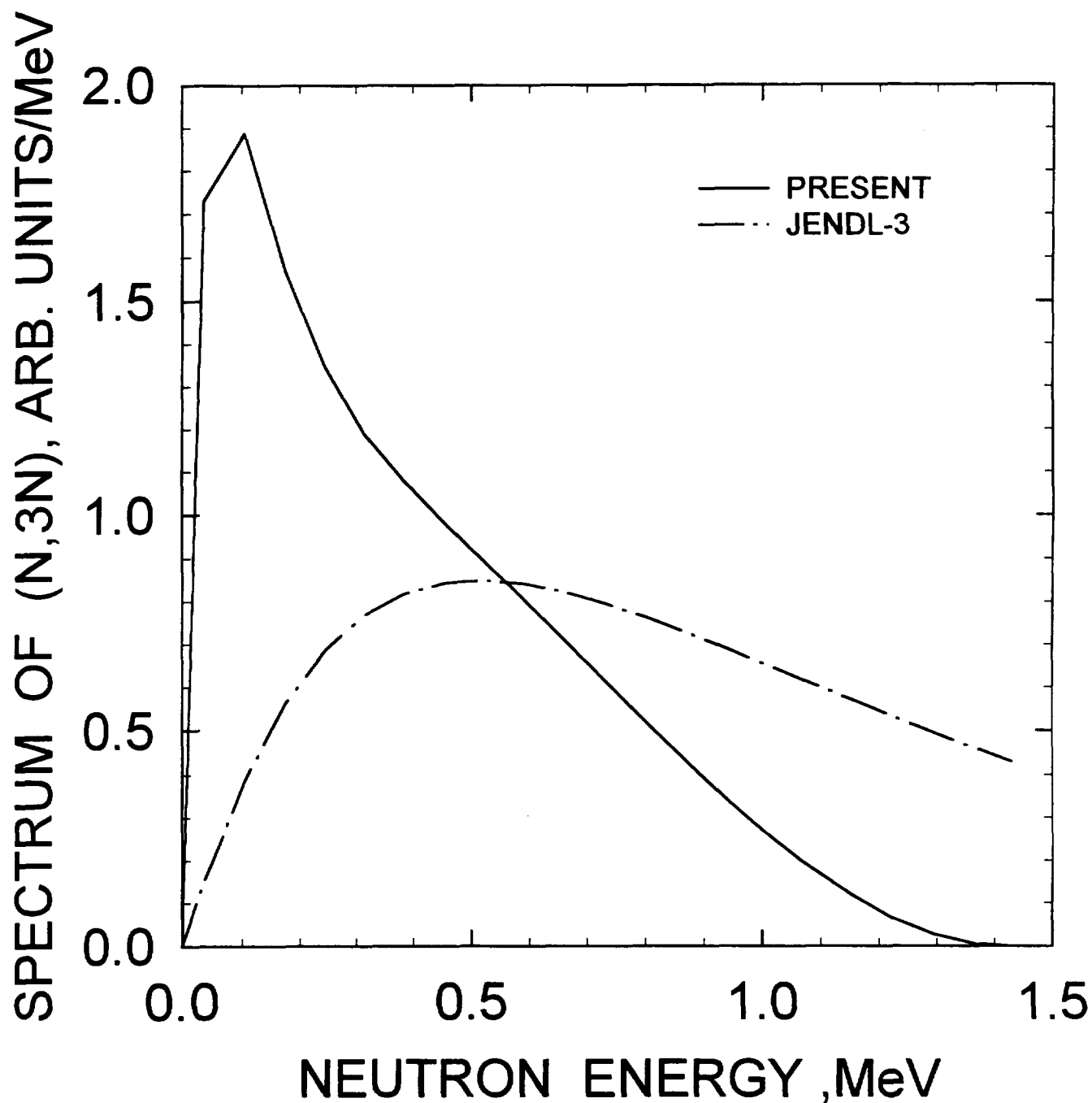


FIG.5.7

^{245}Cm THERMAL PROMPT FISSION
NEUTRON SPECTRUM

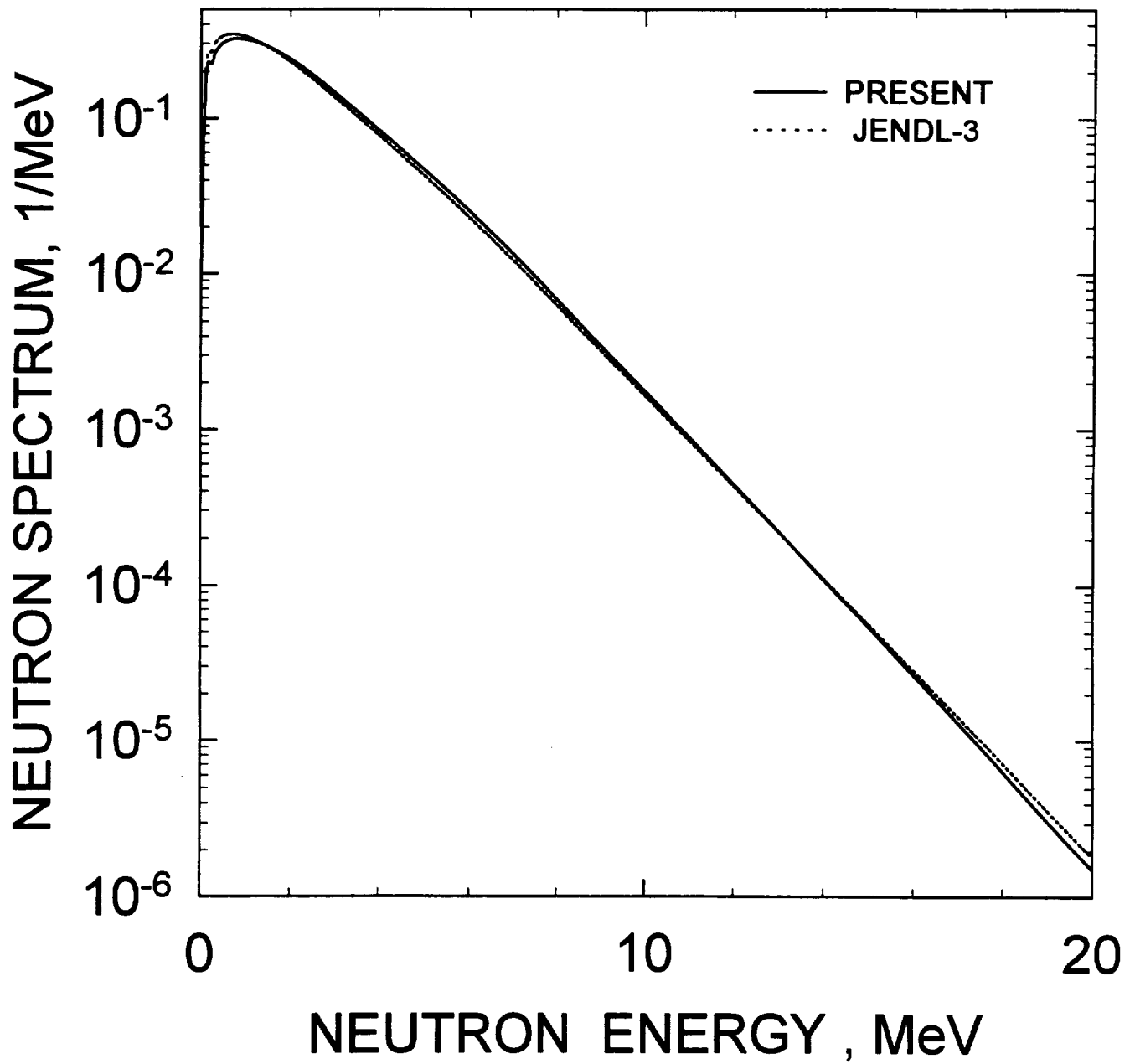


FIG.5.8

^{245}Cm PROMPT FISSION
NEUTRON SPECTRA
RATIO TO JENDL-3 ($T_{\text{MAXW.}} = 1.395$)

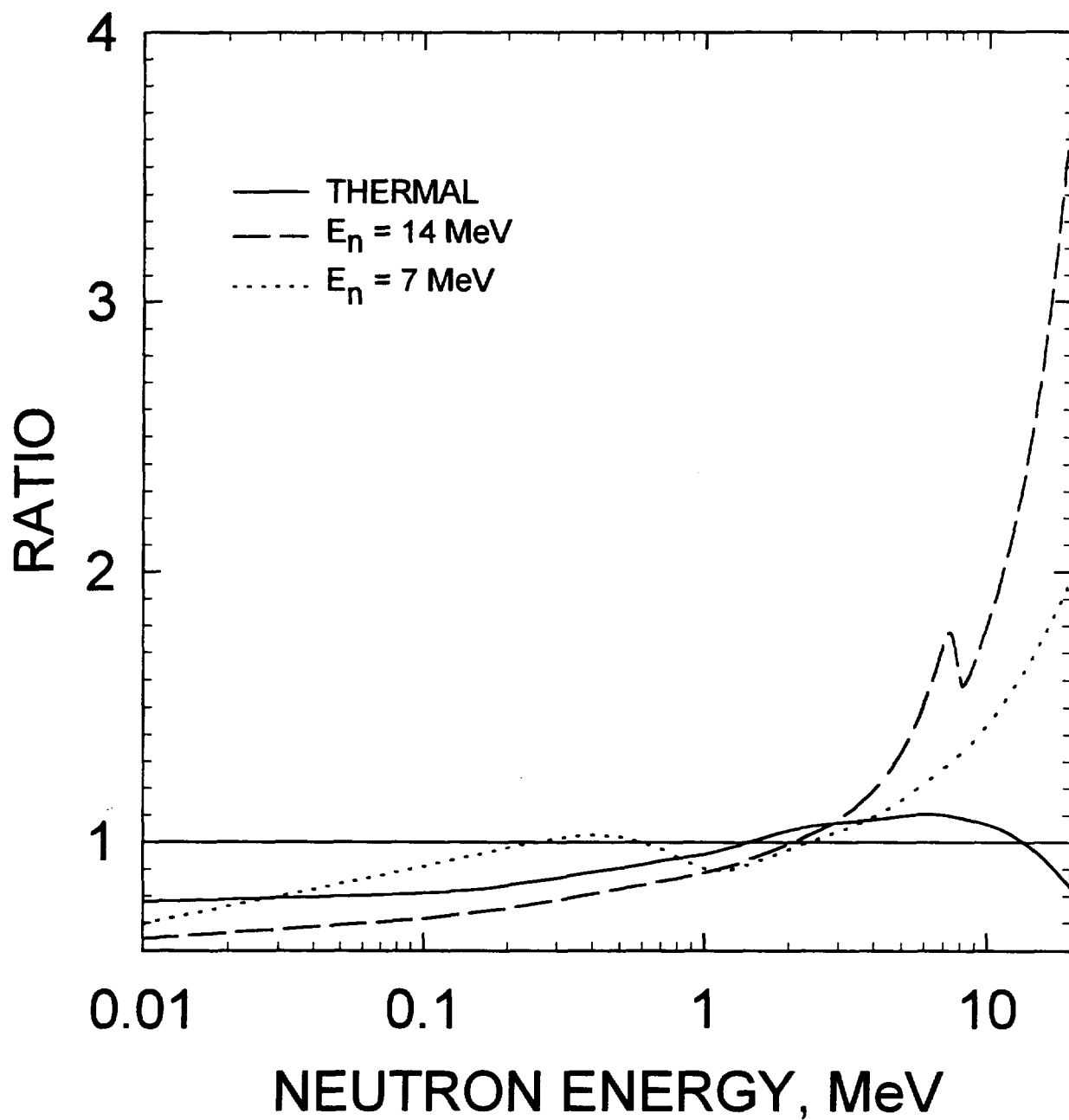


FIG.5.9

^{245}Cm FISSION NEUTRON SPECTRA
RATIO TO MADLAND-NIX MODEL
CALCULATION

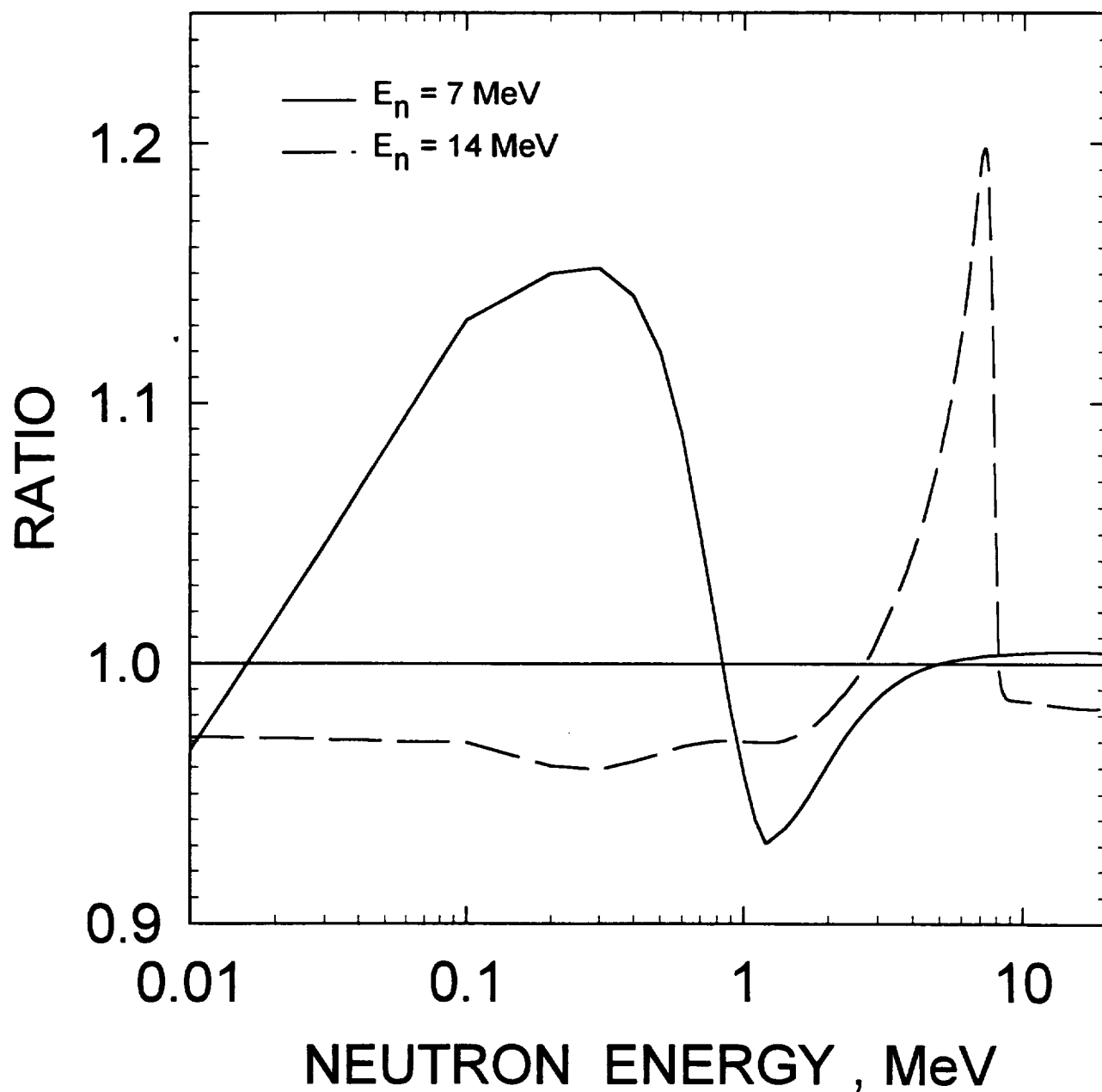


FIG.5.10

^{245}Cm FISSION NEUTRON SPECTRA
FOR $E_n = 14 \text{ MeV}$

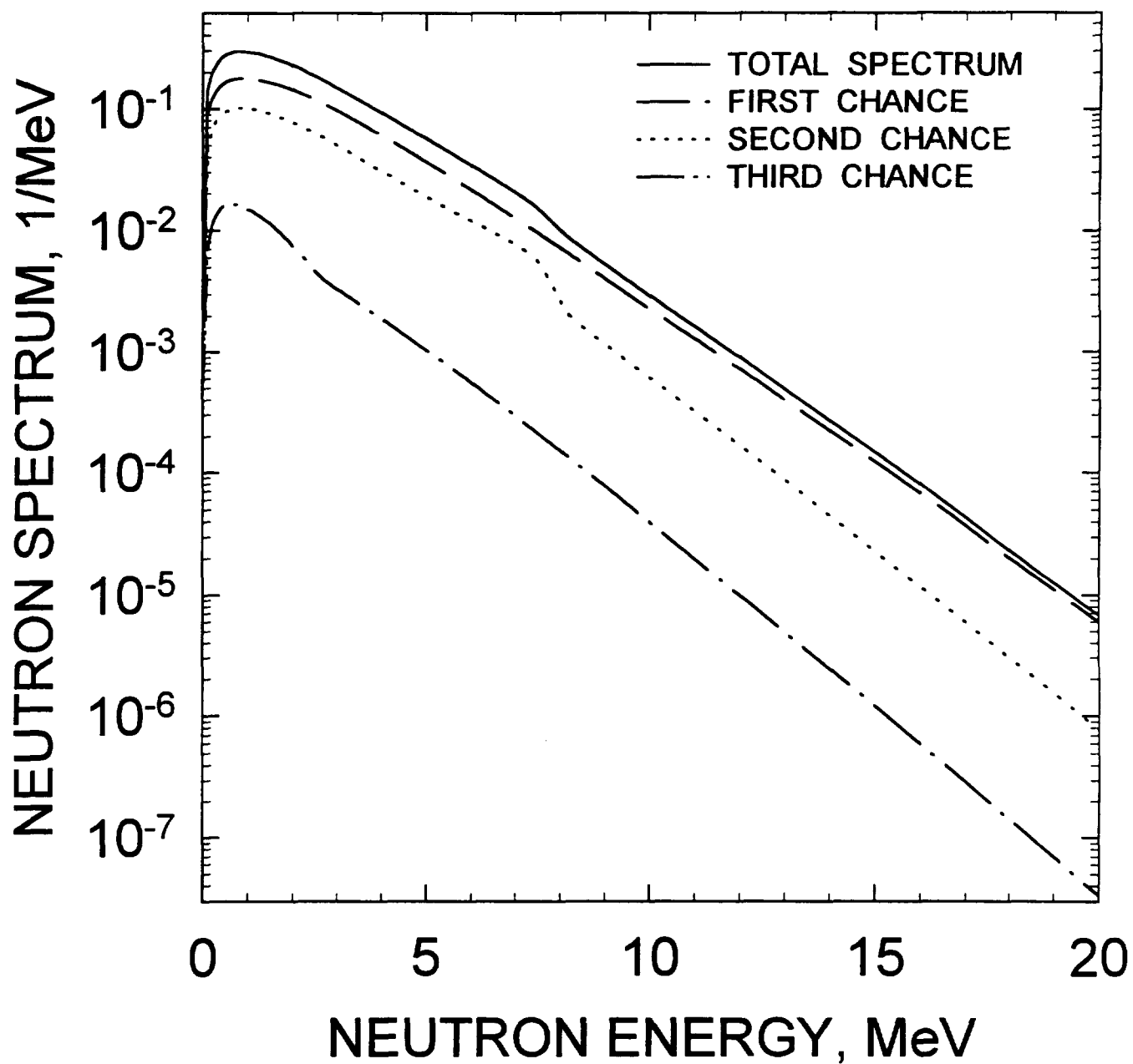


FIG.5.11

^{245}Cm PROMPT FISSION NEUTRON MULTIPLICITY

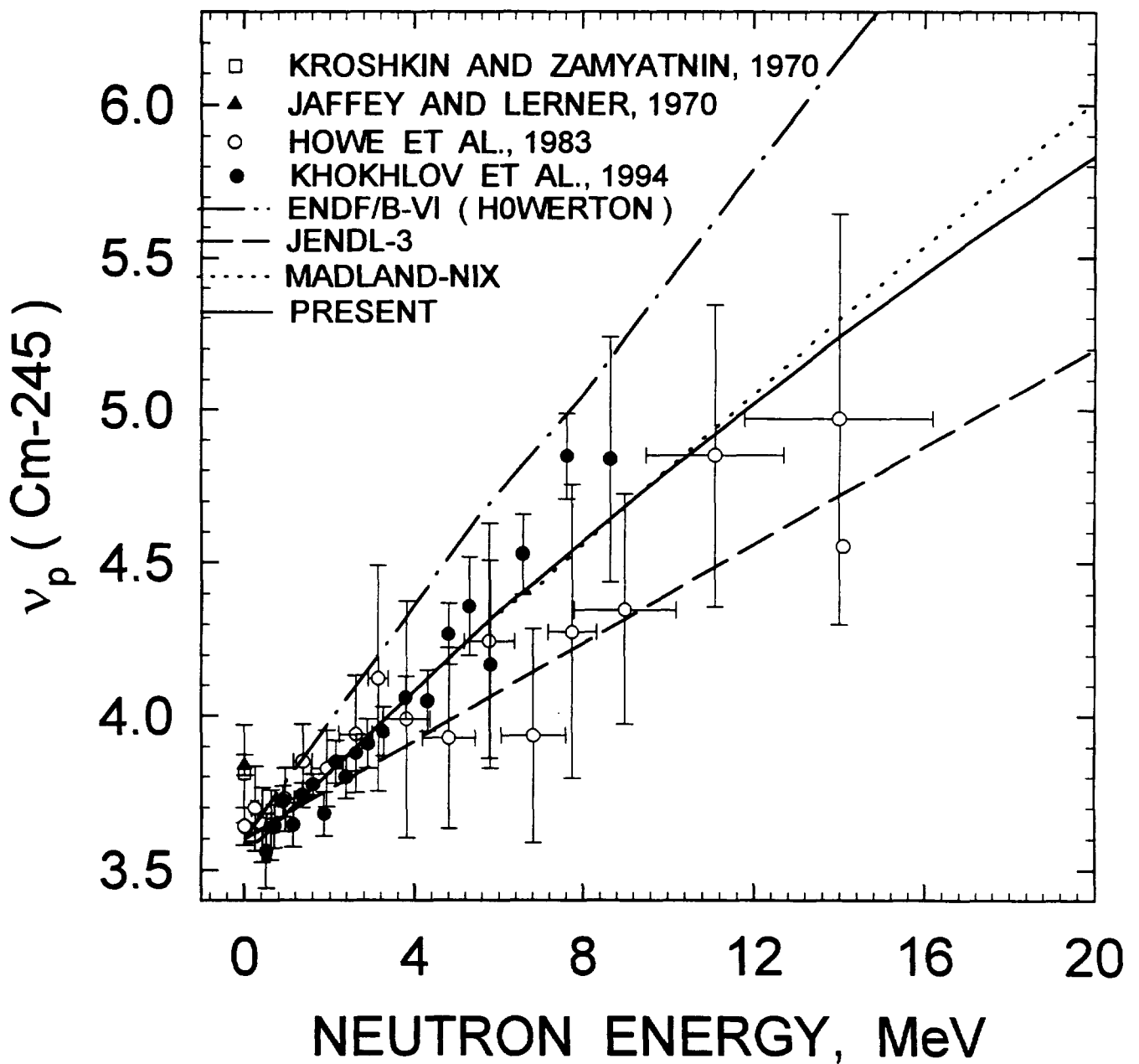


FIG.6.1

Nuclear Data Section
International Atomic Energy Agency
P.O. Box 100
A-1400 Vienna
Austria

e-mail, INTERNET: SERVICES@IAEAND.IAEA.OR.AT
e-mail, BITNET: RNDS@IAEA1
fax: (43-1) 20607
cable: INATOM VIENNA
telex: 1-12645 atom a
telephone: (43-1) 2060-21710

online: TELNET or FTP: IAEAND.IAEA.OR.AT
username: IAEANDS for interactive Nuclear Data Information System
username: NDSOPEN for FTP file transfer
